SLAC-109
UC-34
(EXP)

BACKWARD PHOTOPRODUCTION OF π^0 MESONS AT 6 TO 18 GEV

DONALD H. TOMPKINS

STANFORD LINEAR ACCELERATOR CENTER

STANFORD UNIVERSITY

Stanford, California 94305

PREPARED FOR THE U.S. ATOMIC ENERGY

COMMISSION UNDER CONTRACT NO. AT(04-3)-515

July 1970

ABSTRACT

Differential cross sections for π^0 photoproduction at backward angles have been measured in the momentum transfer range $u = 0$ to -1 $(GeV/c)^2$, for incident photon energies of 6, 8, 12 and 18 GeV. A collimated bremsstrahlung beam from the Stanford linear accelerator was passed through a 40-in. -long liquid-hydrogen target, and the momentum spectrum of the forward moving protons was measured in the SLAC 20 GeV/c magnetic spectrometer. Single pion production is separated from other processes on the basis of kinematics and the spectrum shape.

ACKNOWLEDGEMENTS

It is a pleasure to acknowledge and express my thanks to the many persons with whom I have had the opportunity to work during this experiment.

Professor Walter Selove, graduate advisor, through his interest in research in baryon exchange processes, supported my participation in the research. Association with him has been a most enjoyable and fulfilling experience. His friendly and patient manner of address, his enthusiasm for discussing a point in question, and his support both as advisor and friend are most gratefully and warmly acknowledged.

Professor Bernard Gittelman, initially proposed the experiment and provided direct supervision of its progress. His willingness to give assistance with any detail, his cheerful and friendly manner, and his many kindnesses as both counselor and friend are most appreciated and gratefully acknowledged.

It is also a pleasure to acknowledge the many contributions, too numerous to detail, made by Drs. Robert Anderson, John Litt, Adolph Minten, Bjorn Wiik, and David Yount through their direct participation in the experiment, and their many kindnesses on my behalf. Dr. G. Buschhorn is thanked for his assistance with a portion of the data taking.

I am also grateful for the contributions made by other members of the laboratory, and express my appreciation to each.

Orientation to the on-line computer complex and direct support in the form of system programs was generously given by Drs. Adam Boyarski and Stanley Ecklund.

Dr. Gerhard Fischer assisted with the beam monitors and kindly made available his very complete compilations of their operating characteristics.

Professor David Ritson and Dr. David Gustavson made available at an early stage, their data on backward photoproduction and discussions thereof.

Norb Heiman, Warren Groves, and Keith Doty dealt with the many problems associated with the functioning of the on-line computer complex.

Larry Karvonen, John Grant and Mike Lateur provided much assistance during setup of the experimental apparatus.

Arthur Leino greatly facilitated the data fitting problem through his kindness in providing a scope graphic subroutine allowing direct operator intervention with the fitting program. Hills Lee and William Dickey also were generous with their counsel regarding computer programming problems.

Drs. James Beaupre and Emmanuel Paschos kindly provided graphs of their fits to the backward photoproduction data and many discussions concerning theoretical interpretations of that data.

Appreciation is also expressed to Professor Vernon Barger and Mr. Peter Weiler at the University of Wisconsin for providing graphs of their fits to the backward photoproduction data and discussions of theoretical points.

I wish to express my appreciation to Professor W. K. H. Panofsky for his hospitality while at the laboratory. Professor Richard Taylor kindly made available facilities of Experimental Group A.

The assistance received from the Accelerator Operations Staff, Axel Golde and the RAD Group for beam line setup in End Station A and from Mel Ray and the SLAC Computer Operations staff is greatly appreciated.

Mr. Tony Bell is acknowledged for his kind assistance with drafting problems.

And it is a pleasure to thank the SLAC Reports Office for their wonderful assistance for typing and drafting of figures and for reproducing this document.

The support of the Atomic Energy Commission under Contracts AT(30-10)-2171 and AT(04-3)-515 is gratefully acknowledged.

PREFACE

Backward reactions at high incident energy in which baryons are exchanged in the crossed channel, provide insight into the nature of the exchange mechanism and thus insight into one aspect of particle physics. They also presumably provide information on the strength of baryon-baryon-meson couplings involving one real and one virtual baryon and a real meson.

Boson-baryon processes at high energies show "backward" peaks. Baryon exchange is believed to provide the dominant mechanism for these peaks.

Prior to this experiment, no high energy backward π^0 photoproduction data existed delineating the characteristics of the backward peak in that process. (Lower energy data are presumably dominated by "direct channel" effects rather than by exchange processes.) High energy backward peaks involving baryon exchange had been studied for the first time, recently, in backward elastic pi-proton scattering. The Regge-pole model provided an economical explanation of backward elastic pi-meson scattering. Backward photoproduction of mesons is also believed to be mediated by baryon exchange in the crossed channel and in addition the exchanges should be similar in character to those in the backward elastic pi-meson scattering.

Therefore, if the Regge model is a valid description of such high energy phenomena at a sufficiently fundamental level, it should contain an explanation of backward photo-induced reactions also in terms of an economy of parameters, some of which would be expected to have identical values in both the backward pion-induced and photon-induced reactions.

The experiment reported herein was designed to give experimental data in a new range of energies for several such processes of interest, particularly for

baryon exchange in the backward photoproduction of π^0 mesons, and to provide data for a backward photo-induced reaction against which to test the validity of the Regge-pole model.

Chapter I sets forth the framework in which the questions regarding backward photoproduction are viewed. Chapter II gives a discussion of the relevance of Regge-pole theory to the description of high energy backward processes mediated by baryon exchange. The experimental details concerning this experiment are given in Chapter III with discussion of the data reduction procedure given in Chapter IV. The results and discussion thereof are presented in Chapter V.

TABLE OF CONTENTS

CONTENTS (continued)

LIST OF FIGURES

FIGURES (continued)

LIST OF TABLES

SYMBOL TABLE

α	Regge trajectory function
Bin	Measure of spacial coordinate granularity in a hodoscope. Formed by overlapping rows of scintillation finger counters with the requirement that an ionizing particle produce a pulse in each of the overlapping scintillator elements in the combination of those elements which define the "bin." (usually two or three such elements)
δ	$= \left(\frac{P - P_{spectr}}{P_{spectr}} \right) 100$ = momentum deviation in percent
DCD	Discriminator - Coincidence - Discriminator: one such electronics unit for each hodoscope photo tube. Pulses from the photo tube which passed through the input Discriminator were passed to one side of a Coincidence circuit. The "large fan" gate pulse (see Fig. 3.5) was passed to the second input of the coincidence circuit and a resulting coincidence pulse passed through the final Discriminator and then to a buffer storage unit (see Ref. 5, Chapter III), for later multiplexing into the on-line computer.
E_D	Energy of detected particle (GeV)
EFF	Efficiency factor of detection system for hadrons
EFTL	Effective target length
F	Scale factor for adjusting boundaries of spectrometer acceptances
ΔH(MM)	Number of events recorded in MMth bin of missing mass histogram
JM	Calibration constant for beam monitor
K	Photon energy (GeV)
K_0	Maximum photon energy = electron beam energy
$\partial K/\partial P$	Jacobian transformation between incident photon energy and momentum of detected particles

L	Physical length of hydrogen target (40 inches)
λ	Relates to shape of bremsstrahlung spectrum -(see Eq. (A.3))
M	Proton mass
M_D	Mass of detected particle (GeV)
MM	Bin index in missing mass histogram
MM^2	Squared value of missing mass (GeV^2)
M_T	Mass of target particle
Momentum Hodoscope	Generic name to designate fourth of four hodoscopes (see Fig. 3.4)
N_A	Effective number of target atoms per cm^2
NEQQ	Number of equivalent quanta
ΔN_γ	Number of incident photons
dN(K)	Number of photons in energy band of width dK at photon energy K
N_0	Avagadros number
$\Delta\Omega$	Increment of solid angle (steradians)
$\Delta\Omega\Delta P\|_{bin}$	Increment of solid angle times momentum acceptance per missing mass bin
P	Three-momentum (GeV/c)
ΔP	Three-momentum increment
P_D	Momentum of detected particle (GeV/c)
PHA	Pulse height analyzer
ϕ_0	Projected scattering angle in vertical plane of target space (mrads)
$\phi(K, K_0)$	= K dN(K)/dK; a function which represents normalized shape of bremsstrahlung spectrum
"Phi" - Hodoscope	Generic name to designate first of four hodoscopes (see Fig. 3.4)
ψ_H	Angle in horizontal plane of detection system space made by particle's trajectory with respect to central trajectory (mrads)

ψ_V	Angle in vertical plane of detection system space made by particle's trajectory with respect to central trajectory (mrads)
$\psi(x', \theta_{spectr})$	Source density function for target atoms as seen by spectrometer
ΔQ	Accumulated charge from beam monitor
	Density of hydrogen (gms/cc)
rl	Radiation length
$R(x-x')$	Resolution function for "X-Theta" hodoscope system
s	Center-of-mass energy squared (GeV^2)
$d\sigma/d\Omega$	Laboratory cross section
$d\sigma/dt$	Forward differential cross section
$d\sigma/du$	Backward differential cross section
t	Four-momentum transfer squared $(GeV/c)^2$
T	Isotopic spin quantum number
"Theta"-Hodoscope	Generic name to designate third of four hodoscopes (see Fig. 3.4)
θ_0	Projected scattering angle in horizontal plane of target space (mrads)
θ_{sc}	Scattering angle of detected particle in target space ($\cos \theta_{sc} = \cos \theta_0 \cos \phi_0$)
θ_{spectr}	Rotation angle of spectrometer
u	Four-momentum transfer squared $(GeV/c)^2$
x'	Source integration variable at target
x_d	Horizontal displacement in detection system space of particle's trajectory with respect to the central ray at the focal plane (cm)
x_0	Horizontal displacement of particles's trajectory at the target relative to the spectrometer axis (cm) - measured where trajectory crosses the object space reference plane at target mid-length

"X"-Hodoscope — Generic name to designate second of four hodoscopes (see Fig. 3.4)

y_d — Vertical displacement in detection system space of particle's trajectory with respect to the central ray at the focal plane (cm)

y_0 — Vertical displacement at target of particle's trajectory relative to spectrometer's central ray

CHAPTER I

Introduction

The behavior characteristics of the nucleon, as it takes part in various kinds of high energy interactions, have been the objective of many investigations both theoretical and experimental.

The structure of the nucleon has been looked at in various ways, one of the most important of which involves the study of its electromagnetic structure. In analysis of this kind of data, the work of Hofstadter[1] and others, it is assumed that the interaction can be understood through a factorization model in which the purely electromagnetic effects are exactly understood and therefore the scattering, for example electron-proton scattering, gives information on the electromagnetic structure of the proton. Confidence in such a model, a model in which the "purely electromagnetic" effects are understood exactly, rests on the success that quantum electrodynamics theory has had in treating the experiments on wide angle pair production,[2] wide angle bremsstrahlung[3] and perhaps above all, those of electron-electron[4] scattering.

Excitation states for the nucleon have been revealed in electro-production processes (the excitation initiated by a virtual photon) in the experimental work from DESY[5] and more recently the electron scattering experiments of the SLAC-MIT[6] collaboration. The data on electron-proton scattering should in principle be able to disclose whether there is any central point-like component in the structure of the proton. Elastic data give no such indication. At the present time, the inelastic data are under intensive analysis and no clear conclusions can be drawn regarding the question of proton structure.

Nucleon resonance states produced through strong interactions with values of strangeness quantum number from -3 to 0 have been numerously investigated.[7]

But distinct from those types of studies are "backward" reactions, in which the nucleon participates as the exchanged object. A typical reaction of this kind is indicated in Fig. 1.1 where particles "a" and "b" are not baryons and "b" is emitted in the backward direction in the center-of-mass system. For example, in backward photoproduction of mesons, "a" would be a photon and "b" the photo-produced meson. Furthermore, at high energies and based on a field-theoretic or a Regge-type model, backward reactions would be expected to show backward peaks, arising from the exchange of objects with appropriate quantum numbers. It remains a question, though, as to whether such baryon exchange effects can be seen or whether they are too small in comparison with the contribution to the backward direction from the tail of the forward peak.

It has been found, however, that forward peaks fall off in $d\sigma/dt$ as exp (Bt), (for example see Ref. 8) with B roughly independent of t, or step-wise varying with t. t is the square of the four-momentum transfer for "forward" scattering. Recalling that the sum of the Mandelstam variables s + t + u equals the sum of the squared masses of the particles participating in the reaction, then for the backward direction, where u is small, the magnitude of t increases with s, the square of the center-of-mass energy. Thus the contribution to the backward direction from the tail of the forward peak would be expected to fall exponentially with s. The exchange peak, on the other hand, would be expected to fall not exponentially with s but as s^{α} where for an "elementary particle" model α would be a constant (the spin of the exchanged particle) and for a Regge model α would be a function of u. The important point is, therefore, that as s is increased, the tail from the forward peak will fall as Const(exp(-Bs)) whereas the backward peak will fall less rapidly, as s to a power, and thus it might be expected that at sufficiently high energies the characteristics of the backward peak could be seen.

By the early 1960's there existed some evidence for such a backward peak in pion scattering from the proton. However, at that time no experiment had been designed that had sufficient sensitivity to see the peak in any detail. In 1965-66, two experiments were carried out which together showed these peaks in detail. One, by Frisken et al.,[9] showed the region very close to 180^{o}. The other, by Brody et al.,[10] covered a "u" range approximately equal to M^2 (the proton mass squared) near 180 degrees. u is defined as the square of the four-momentum transfer from incident boson to outgoing nucleon; we use a metric in which u is positive when time-like. The combined results showed the existence of and measured the magnitude for the backward peak; and Brody et al., found in the case of the π^+ proton elastic scattering that a pronounced dip effect occurred in the neighborhood of $u = -0.2\ (GeV/c)^2$, while no such effect appeared for the negative pion scattering.

Several important conclusions were drawn from that experiment. First, the existence of a backward peak with a shape roughly independent of "s" was consistent with baryon exchange as the dominant mechanism mediating such backward processes. Second, the π^-p interaction can only occur through a T = 3/2 exchange. In the π^+p interaction, isospin Clebsch-Gordon coefficients show that T = 3/2 exchange contributes less than it does in the π^- interaction; yet the π^+ proton cross section was found to be much larger than that of π^- proton. This suggested the conclusion that T = 1/2 exchange dominated the π^+ proton reaction, and was also responsible for the dip.

But perhaps the most important conclusion drawn from that experiment regarded the Regge nature of the exchanged nucleon. Chiu and Stack[11] showed that the dip effect in the backward π^+p scattering, together with the absence of any such dip in the π^-p scattering, could be understood on the basis of a Regge

pole model with the exchanged nucleon (T = 1/2) and Δ (T = 3/2) having Regge behavior. Chiu showed that for Reggeized nucleon exchange a dip would be expected in the differential cross section, $d\sigma/du$ where the nucleon trajectory $\alpha(u)$ passed through the value Re $\alpha(u) = -1/2$. The remarkable result was found that if the experimentally observed dip was interpreted in terms of the trajectory passing through $\alpha(u) = -1/2$ at that value of u, namely $u \sim -0.2$ $(GeV/c)^2$, then the nucleon trajectory thus defined would join smoothly with the nucleon trajectory determined in the time-like region from the observed baryon states.

In view of the above results, the question arose as to whether Regge effects would be seen in backward scattering if the exchanged fermion were an electron instead of a baryon. The work of Gell-Mann et al.,[12] had shown that fermions interacting with nonzero rest-mass vector bosons seemed theoretically to be Reggeized, by radiative-correction effects. Might it also be expected that fermions which interact with massless vector bosons, namely the photon, also are Reggeized and in particular would the electron itself exhibit Regge behavior? Present theory does not give a clear answer to this question.

With regard to these points, electron Compton scattering cross sections were measured[13] at 180 degrees for incident beam energies of 0.5 and 1.0 GeV. In this process the electron is the exchanged fermion. It was found that for u values covering the range 0 to -0.003 $(GeV/c)^2$ the measured backward peak was in agreement with the predictions of the Klein Nishina formula and to the 15% level no Regge effects were seen. Due to the smallness of the u values attained, the experiment was not very sensitive and thus further experimental results are awaited regarding the possible Regge nature of the electron.

With the above in mind, the present experiment, reported here, was planned with the following objectives:

(a) New, unknown cross sections would be measured for the photoproduction of π^o mesons near 180 degrees in the process $\gamma + p \longrightarrow p + \pi^o$ at energies heretofore unattainable. The cross section was to be traced out as a function of u for four primary beam energies.

(b) Initial crude values of the photoproduction cross sections would be obtained for the reactions $\gamma + p \longrightarrow p + \left\{ \begin{matrix} \eta \\ \rho^o \end{matrix} \right\}$ at two u values for each primary beam energy.

(c) The simple Regge-pole model appears to provide a satisfactory explanation for the behavior of the cross sections measured in backward $\pi^{\pm} p$ elastic scattering. It would therefore be interesting to see if such a model could satisfactorily explain, at the same time, the behavior of the cross sections in all five of the reactions listed below. The measurements reported here contribute the information on reaction #4.

(1)	$\pi^+ + p \longrightarrow p + \pi^+$	Ref. (18)
(2)	$\pi^- + p \longrightarrow p + \pi^-$	Ref. (18)
(3)	$\pi^- + p \longrightarrow n + \pi^o$	Ref. (16)
(4)	$\gamma + p \longrightarrow p + \pi^o$	this exp.
(5)	$\gamma + p \longrightarrow n + \pi^+$	Ref. (17)

These five reactions proceed through baryon exchange in the crossed channel with allowed isospin T exchange of 3/2 or of 1/2 and 3/2. It is noted that in a Regge model the residue functions, $\gamma(u)$, for photoproduction will not be the same as those for pion-proton scattering but presumably will be three new functions, two for the γNN and one for the $\gamma N\Delta$ vertex. (The γNN vertex requires two such functions because the photon coupling has both isoscalar and isovector components.)

Nevertheless the trajectories, $\alpha(u)$ should not be new. In that way it is desired to see if the baryon exchange peak in the photoproduction experiments can be understood in terms of the same Regge trajectories that were used to analyse the backward πp scattering experiment.

The relationship of the data obtained from the measurements reported here to those previously obtained for the same reaction by Croissiaux et al.,[14] at Orsay and Buschhorn et al.,[15] at DESY is shown in Fig. 1.2.

REFERENCES FOR CHAPTER I

1. R. Hofstadter, Rev. Mod. Phys. 28, 214 (1956).
2. J. G. Asbury, William K. Bertram, U. Becker, P. Joos, M. Rohde, A. J. S. Smith, S. Friedlander, C. L. Jordan, Samuel C. Ting, Phys. Rev. 161, 1344 (1967).
3. R. H. Sieman, W. W. Ash, K. Berkelman, D. L. Hartill, C. A. Lichtenstein, R. M. Littauer, Phys. Rev. Letters 22, 421 (1969).
4. W. C. Barber, B. Gittelman, G. K. O'Neill, B. Richter, Phys. Rev. Letters 16, 1127 (1966).
5. W. Bartel, B. Dudelzak, H. Krehbiel, J. McElroy, W. Meyer-Berkhout, W. Schmidt, V. Walther, and S. G. Weber, Vienna Conference, Paper #821, (1968);

   W. Albrecht, F. W. Brasse, H. Dorner, W. Flanger, K. Frank, E. Ganssauge, J. Gayler, H. Hultschig, J. May, Vienna Conference, Paper #313 (1968).
6. W. K. H. Panofsky, XIV International Conference on High Energy Physics, Vienna (1968) or "Low q^2 electrodynamics, elastic and inelastic electron (and muon) scattering," Report No. SLAC-PUB-502, Stanford Linear Accelerator Center, Stanford University, Stanford, California (1968).
7. Arthur Rosenfeld, Naomi Barash-Schmidt, Angela Barbaro-Galtieri, Leroy R. Price, Paul Söding, Charles G. Wohl, Matts Roos, William J. Willis, Rev. Mod. Phys. 40, 77 (1968).
8. J. Orear, R. Rubinstein, D. B. Scarl, D. H. White, A. D. Krisch, W. R. Frisken, A. L. Read, and H. Ruderman, Phys. Rev. 152, 1162 (1966).
9. W. R. Frisken, A. L. Read, H. Ruderman, A. D. Krisch, J. Orear, R. Rubinstein, D. B. Scarl, and D. H. White, Phys. Rev. Letters 15, 313 (1965).

10. H. Brody, R. Lanza, R. Marshall, J. Niederer, W. Selove, M. Shochet, R. Van Berg, Phys. Rev. Letters 16, 828 (1966).

11. Charles B. Chiu and John D. Stack, Phys. Rev. 153, 1575 (1967).

12. M. Gell-Mann, M. L. Goldberger, F. E. Low, E. Marx and F. Zachariasen, Phys. Rev. 133, B145 (1964).

13. B. Gittelman, W. C. Barber, W. Selove, D. Tompkins, F. Forman, Phys. Rev. 171, 1388 (1968).

14. M. Croissiaux, E. B. Dally, R. Morand, J. P. Pahin, W. Schmidt, Phys. Rev. 164, 1623 (1967).

15. G. Buschhorn, P. Heide, U. Kötz, R. A. Lewis, P. Schmüser, H. J. Skronn, Phys. Rev. Letters 20, 230 (1968).

16. V. Kistiakowsky, R. K. Yamamoto, R. D. Klem, P. Marcato, I. A. Pless, I. Spirn, E. F. Anelli, C. N. DeMarzo, A. Romano, D. G. Crabb, A. C. Meyers, III, and J. R. O'Fallon, Phys. Rev. Letters 22, 618 (1969); R. C. Chase, E. Coleman, H. W. J. Courant, E. Marquit, E. W. Petraske, H. Romer, and K. Ruddick, Phys. Rev. Letters 22, 1137 (1969).

17. R. Anderson, D. Gustavson, J. Johnson, D. Ritson, R. Weinstein, W. G. Jones, D. Kreinick, Phys. Rev. Letters 21, 479 (1968); R. Anderson, D. Gustavson, J. Johnson, I. Overman, D. Ritson, and B. Wiik, "High-energy photoproduction of charged pions at backward angles," Report No. SLAC-PUB-631, Stanford Linear Accelerator Center, Stanford University, Stanford, California (1969).

18. J. Orear, D. P. Owen, F. C. Peterson, A. L. Read, D. G. Ryan, D. H. White, A. Ashmore, C. J. S. Damerell, W. R. Frisken, R. Rubinstein, Phys. Rev. Letters 21, 389 (1968).

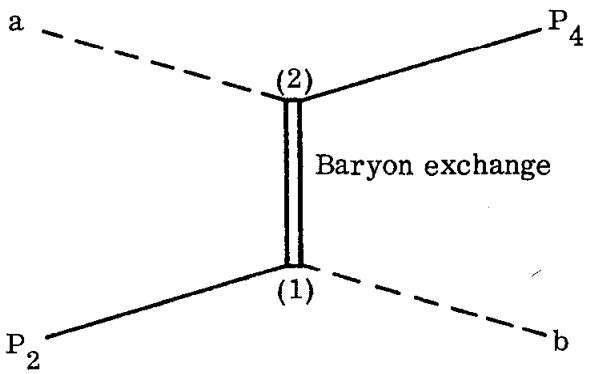

Fig. 1.1--Figure indicates a "backward" reaction mediated by baryon exchange. Particles P_2 and P_4 are baryons while particles "a" and "b" are not. Particle "b" is taken to be emitted in the backward direction in the center-of-mass system.

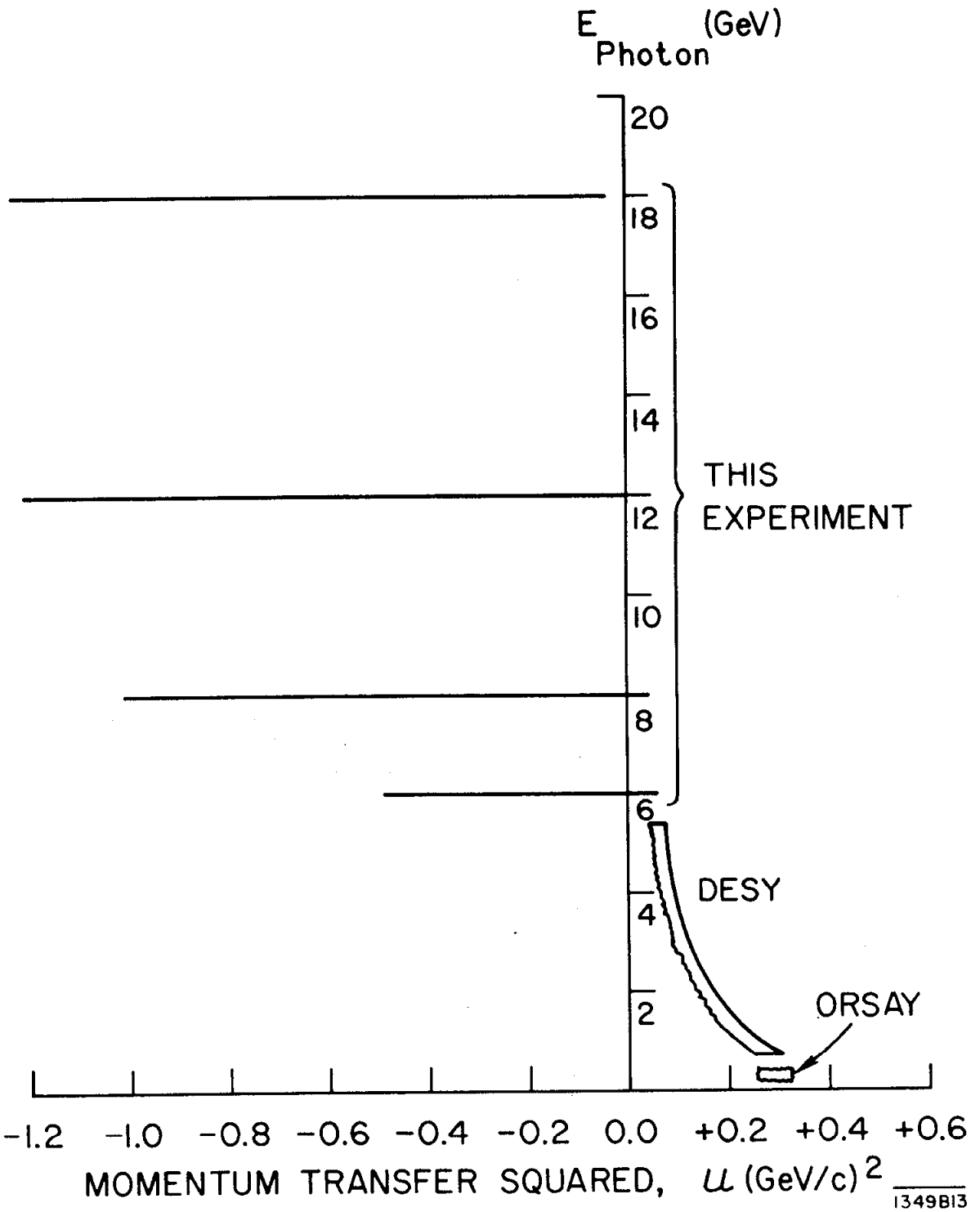

Fig. 1.2--Figure depicts the ranges of energy and momentum transfer squared of the measured cross sections for the reaction $\gamma + P \longrightarrow P + \pi^0$.

CHAPTER II

THEORETICAL BACKGROUND

A major effort in the many attempts to create a description which explains the observed properties of the strong interactions, has been that of the "S-Matrix Theory." The S-matrix elements, which describe processes of scattering and decay, are taken to be functions of complex variables; for example, energy and momentum transfer. The procedure then has been to explore and exploit the analytic properties of those elements (the transition amplitudes) with the intent of adding further predictive power into the theory and also providing an understanding of the presently available data.

Considerable difficulty with the initial or early theories describing "elementary" particles, was experienced due to predictions from Feynman graph calculations for exchange processes, that asymptotically at high energy the Lorentz invariant amplitude had an energy dependence of the form s^{J^1} (s the center-of-mass energy squared) where J, the spin of the exchanged particle, has a constant (fixed) magnitude. One can show that σ_{total} diverges if $J > 1$. Consequently, this s^J form gives the result that exchanges of high J-particles, with $J > 1$, leads to divergent cross sections, which grow without limit as $s \longrightarrow \infty$. Experimentally, however, cross sections were observed to either decrease with increasing s or to trend toward what appeared to be constant values.[2]

By the late 1950's, T. Regge[3] had introduced a theory for potential scattering which theorists recognized contained important implications for the theoretical high energy dependence of the cross section and which indicated how the previous divergence problems embodied in the "elementary particle" approach might be eliminated. Although Regge theory has not proved to be an all encompassing exposition of high energy phenomena, it has enjoyed some significant successes. Some

of these successful aspects of Regge theory were identified in 1965-66, as indicated below, and it was these successful applications which were in good part responsible for the planning of the present experiment. Accordingly, this section sets forth an elementary discussion of Regge theory and the structure of the Reggeized amplitude, and gives an indication of its pertinence to the present experiment. Detailed accounts of Regge theory can be found in numerous writings, a few of which are given in Ref. (4).

It has long been known that the amplitude for scattering may contain poles with respect to the energy, poles which describe either bound states or resonances. For our discussion we take the case of spinless particles. Regge's contribution was to show that in potential scattering, if the scattering amplitude $f(s, t)$ is expanded in a partial wave series, i.e., $f(s, t) = \sum_J (2J + 1)\, f_J(s)\, P_J(z)$, where $z = \cos\theta$, then the partial wave amplitude $f_J(s)$ can be continued, in the complex angular momentum plane (J-plane) into a respectable function, $f(J, s)$ of J. The energy-domain poles of $f(s, t)$ appear as J-domain poles in $f(J, s)$. Furthermore, and most importantly, the J-plane poles may move as a function of energy. Therefore, it is possible to write down an amplitude $f(J, s)$ which acts as a unique interpolating function between integer or half-integer values of J, and which takes on the characteristics of the partial wave scattering amplitude, $f_J(s)$, at the physically allowed J values. These concepts from potential theory were then taken over by elementary particle theorists, as the basic working hypotheses for a Reggeized theory to describe high energy (relativistic) phenomena.

The attractiveness of the moving pole concept is twofold; (1) the amplitude A $\left(\text{where A is related to the cross section by } \frac{d\sigma}{d\Omega} = \frac{1}{s}\left|A\right|^2\right)$ now has an energy dependence (for spinless particles) of the form $s^{\alpha(t)}$ where $\alpha(t)$ is the "effective spin" of the exchanged object and depends on the four momentum transfer squared,

t. Now for a reaction in which s is the total energy squared, the physical region for t is < 0 (we consider the rest masses to be equal, or else negligible). Thus if the moving poles have the property that for all such poles $\alpha(t)$, for $t < 0$, is no larger than 1, then the divergence in σ_{total} described above will be eliminated. This was the basic proposal of Chew and Frautschi,[5] for the Regge behavior of exchanged particles in elementary particle reactions. Thus the important point is that the exchanged particle has an "effective spin" whose magnitude is connected with the particle's four momentum transfer. (2) Seemingly unrelated resonances and/or bound states at say energies s_1, s_2, ... and spins J_1, J_2, ... may indeed be manifestations of a single moving pole which journeys across the J-plane. Thus a connection is provided amongst particles with different masses and spins but with identical values for their internal quantum numbers (strangeness, baryon number, isospin, and parity). Such particles (poles) are said to be on a Regge trajectory. When the trajectory function, α, passes directly through an integer value, a bound state appears (i.e., through a pure real integer or, for baryons, half integer) for the physical system, whereas when $\mathrm{Re}\alpha$ passes near to an integer value, but in addition α has a small imaginary part, then a resonance state appears in that system. A set of real states, associated with each other in this way, is also associated with the properties of the transition amplitude when the corresponding particle or "family" acts as the exchange particle in a reaction. Thus the description of an interaction, in terms of the Regge model, is given in terms of the exchange of a Regge trajectory (s), a set of quantum numbers, rather than the exchange of an "elementary particle."

For example, the proton N(j = 1/2, M = 938 MeV) and N*(J = 5/2, M = 1688 MeV) are two of several particles taken to lie on the Regge trajectory with the set of quantum numbers (strangeness = 0, baryon number = 1, isospin = 1/2,

and parity = +1) and usually designated, N_α. (This was the first pair of real states to be associated with each other in the Chew-Frautschi proposal; from this single pair Chew and Frautschi guessed at a more or less universal slope for Regge trajectories.) Consequently, if an experiment could allow the exchanged object to have these quantum numbers and an energy of 938 MeV then it would appear as the nucleon with spin $\alpha = 1/2$, whereas for the same quantum numbers, but with an energy of 1688 MeV the same exchanged object would have a spin $\mathrm{Re}\alpha = 5/2$, etc.

Regge theory was introduced to particle physics in this way in 1962. In the course of the next few years it fell somewhat out of favor, however, when experimental results began to appear which contradicted predictions extracted from the early form of that theory. Specifically, Regge theory predicted a shrinkage effect in $d\sigma/dt$ for increasing s. Although such a shrinkage effect does appear to exist for pp scattering,[6] other hadron scatterings do not show a consistent shrinkage effect, in fact, $\bar{p}p$[7] scattering soon showed an anti-shrinkage effect. The shrinkage effect was predicted on the basis of a dominance of the highest trajectory expected to apply in the high energy limit. In the face of nonshrinkage, explanations were still possible in the framework of Regge theory, but required appeal to the idea that the asymptotic region had not been reached and that therefore, many different exchanges were contributing. Thus many parameters were introduced into the theory, and the result did not have the attraction of simplicity or economy of description. Consequently, Regge theory fell into some disrepute, for particle physics.

The subsequent measurement of the forward $\pi^- p$ charge exchange reaction ($\pi^- p \longrightarrow \pi^0 n$),[8] and its interpretation,[9] in late 1965, infused the Regge concept with a new vitality of life. Noting that the possibilities for quantum numbers[1]

of the exchange quantity were restricted to strangeness = 0, baryon number = 0, isospin = 1, parity = -1 and the spin J, to 1, 3, ... one finds that only the ρ-meson, of the then known particles, qualified for the exchange. In terms of the Regge model, the restriction on quantum numbers implied that exchange of a single trajectory mediated the reaction. The Regge-expected shrinkage effect was found in these data, and the functional form of the trajectory, $\alpha(t)$ with t in its space-like domain, i.e., < 0 — was determined from the shrinkage.

Two significant effects were noted from the trajectory function. First, it was found to be approximately linear, $\alpha(t) = \alpha_0 + \alpha_1 t$ with $\alpha_0 \approx -0.5$ and $\alpha_1 \approx 1$ $(\text{GeV/c})^2$; and this linear form when extrapolated into the time-like range of $t(t > 0)$, passed very closely through the point $t = M_\rho^2$ when $\alpha(t) = J = 1$. Thus the concept of the moving pole, the pole whose "effective spin" was tied to the t-value associated with the exchanged quantity, but which "effective spin" took on the spin value for the physical particle when the value of t reaches the pole (energy) of the real particle, did indeed seem to be a correct and useful concept. Moreover, the Chew-Frautschi conjecture of a slope value of $\approx 1/(\text{GeV})^2$ for Regge trajectories received striking support.

Second, it was noted that $\alpha(t)$ had a zero magnitude at that value of $t(-0.6$ $(\text{GeV/c})^2)$ at which a dip structure was noted in the cross section, $d\sigma/dt$. It was at this juncture of events that theorists noted that the then known form for the Regge amplitude did indeed contain the necessary mechanism for producing such a dip effect; an observation which, until that time, had not been made. Regge theory, once again, became the focus of many intensive efforts!

Experimentally, it then became important to investigate reactions which were thought to have a simple description in terms of a Regge model. The forward $\pi^- p$ charge exchange scattering, which is mediated via the exchange of a single

trajectory — the rho trajectory — is one such process. A second group of reactions are the so-called backward processes, reactions in which meson plus baryon gives a meson at backward angles and for which the exchanged quantity(s) carries baryon number = 1. Backward $\pi^{\pm}p$ elastic scattering (reaction #1 and #2 of Chapter I) has been measured and analysis of the data[10] in terms of two exchanged trajectories, yielded a good description of the experimental results in terms of relatively few parameters. In this $\pi^{\pm}p$ backward scattering, once again it was noted that the moving pole concept appeared to have validity. The equations for the trajectories exchanged in the $\pi^{\pm}p$ backward scattering were determined by fits to the data with the momentum transfer variable (now called u for backward processes) in its space-like range. Recalling that each trajectory represents a set of internal quantum numbers, then a plot can be made a Chew-Frautschi plot in which the spins of known particles having the internal quantum numbers associated with the Regge trajectory are plotted against the squared rest mass of those particles. The trajectory in the time-like region of u ($u > 0$) is found by drawing a simple curve through those plotted points. Now according to the moving pole concept, as the effective-spin of the exchanged quantity moves with momentum transfer, it must take on the spin-value for the real particle when the momentum transfer (now in its time-like range) takes on the value of the rest mass squared for the real particle. Significantly each of the two trajectories determined from the $\pi^{\pm}p$ data, the $T = 1/2$ and $T = 3/2$ trajectories, when extrapolated into the time-like regions of u did indeed join smoothly onto the trajectories ($T = 1/2$ "N_{α}" and $T = 3/2$ "Δ_{δ}") determined from the Chew-Frautschi plot.

So $\pi^{\pm}p$ backward scattering again, like forward $\pi^{-}p$ charge exchange scattering, gave an impressive connection between the Regge trajectory as determined for virtual nucleons at space-like u, and the trajectory as determined for real nucleon

states at time-like u. But there was more. A striking dip effect was found in $\pi^+ p$ backward scattering, and no dip in $\pi^- p$ scattering; and these two facts, and the position of the dip, again received an extremely simple interpretation on the basis of Regge theory. (And to date no other equally simple interpretation has been advanced.)

Thus, the moving pole danced to the tune the orchestra played!

We have said that a very important success of Regge theory was the fact that it gave a simple interpretation of the dip effects that were found in 1965-66. We now discuss the dip effect, and further aspects of Regge amplitudes, in more detail.

The Reggeized amplitude, for the case of baryon exchange (particle states for this case have half integral spin), has the structure given in the following expression[11]

$$f(\sqrt{u}, s) = \gamma(\sqrt{u}) \frac{1}{\Gamma(\alpha+1/2)} \frac{1+\tau\, e^{-i\pi(\alpha-1/2)}}{\cos \pi\alpha} s^{\alpha-1/2}$$

The residue function γ, gives a measure of the strength with which a particular trajectory is present in a specified amplitude. The total amplitude for a reaction usually consists of a sum of terms of the form above — one such term for each exchanged trajectory. The signature factor $= \frac{1+\tau\, e^{-i\pi(\alpha-1/2)}}{\cos \pi\alpha}$, with $\tau = \pm 1$, allows for the possibility that the dynamics for states of even and odd J may not be the same. Therefore every other pole — poles occurring due to the $\cos \pi\alpha$ term in the denominator when α takes a half integral value — is "killed" by the zero produced in the numerator at those half integral values of α. The half integral values of α for which the numerator of the signature factor is 0 are termed 'wrong signature' points whereas the points with the numerator equal to 2 are termed 'right signature' points. Thus the amplitude in the time-like region

of four-momentum has the sequential behavior pole — finite value — pole — finite value, at succeeding half integral values of α.

The gamma function in the denominator of the amplitude expansion plays a key role for explaining the dip structures observed in the data in the space-like four-momentum region. Considering the case of the backward $\pi^+ p$ elastic scattering, the dip appeared when α for the nucleon (N_α) trajectory was $\simeq -0.5$ $(GeV/c)^2$ ($u \simeq -0.2$) or one unit of spin below the lowest lying pole on that trajectory. Following the structure sequence of pole — finite value — etc. it would be expected that at this 'wrong signature' point where $\alpha = -1/2$, the amplitude would have a finite value. However, the skillfully arranged gamma function, $\Gamma(\alpha + 1/2)$ becomes infinite when its argument is zero or negative and thus forces the amplitude to a zero value at that point. Thus in the space-like region of momentum transfer, the amplitude for exchange of the N_α trajectory changes to the sequence zero — finite value — zero etc. at each successively smaller half integral value of α, beginning at $\alpha = -1/2$. Mathematically the origin of that convenient and crucial gamma function lies in the asymptotic expansion ($s \longrightarrow \infty$) that is ultimately made of the Legendre function appearing in the partial wave expansion of the scattering amplitude — an expansion that occurs in developing the Reggeized form for the amplitude. Physically, the zero in the amplitude at $\alpha = -1/2$, or its reflection as the dip structure seen in the cross section, rests on the principle that angular momentum is a conserved quantity. Violation of that principle would occur when the spin of the exchanged object is less than the helicity change of the two external particles (one initial — one final) connected to the exchanged quantity at either vertex of an exchange diagram, see for example Fig. 1.1. Such a pole position has come to be called a "nonsense" point in Regge theory;[12] it is clear that on physical grounds no pole effect can occur at such a point. Thus the point

$\alpha = -1/2$ for the nucleon, N_α, trajectory, and similar points for other trajectories, is termed a 'wrong signature-nonsense' point. At a 'wrong-signature nonsense' point it is clear that one expects a zero in the amplitude. With the total amplitude describing $\pi^+ p$ backward elastic scattering the sum of two amplitudes, one for N_α exchange and one for exchange of the "Δ" trajectory, the dip structure would occur at the zero of the N_α amplitude — the 'wrong signature-nonsense' point.

It is thus evident that the prediction of dips in cross sections should be a firm prediction of Regge theory. Unfortunately, the theory does not give a prescription for calculating the magnitude for the residue functions in a specified reaction. The consequence of this is that the importance of a given amplitude representing the exchange of a particular trajectory — which amplitude may contain a nonsense zero — is <u>not</u> predictable before the fact and thus the possibility of predicting dips is voided. (See the discussion concerning the photoproduced reactions in Chapter V).

Backward meson photo production, the domain of this experiment, is also mediated by baryon exchanges, with at least some of the exchanged trajectories the same as those found in the backward pion scattering. A Regge analysis of these kinds of reactions can be found in the paper of Refs. 11 and 13.

REFERENCES FOR CHAPTER II

1. L. Van Hove, Comments on Nuclear and Particle Physics 1, 191 (1967).
2. S. J. Lindenbaum, Oxford International Conf. on Elem. Particles (1965); p. 93.
3. T. Regge, Nuovo Cimento 14, 951 (1959).
4. R. Omnes and M. Froissart, Mandelstam Theory and Regge Poles, (W. A. Benjamin, Inc., New York, 1963);
   G. Chew, S-Matrix Theory of Strong Interactions, (W. A. Benjamin, Inc., New York, 1961);
   R. C. Arnold, Argonne National Lab. Report No. 7173, Argonne, Illinois, (1966);
   W. R. Frazer, Proc. Internat'l. School of Phys., Course XLI (1966) p. 82.
5. Geoffrey F. Chew and Steven C. Frautschi, Phys. Rev. Letters 8, 41 (1962).
6. G. Cocconi, Internat'l. Conf. on High Energy Physics, CERN 1962, p. 883.
7. B. Barish, D. Fong, R. Gomez, D. Hartill, J. Pine, A. V. Tollestrup, A. Maschke, T. F. Zipf, Phys. Rev. Letters 17, 720, (1966).
8. P. Sonderegger, J. Kirz, O. Guisan, P. Falk-Vairant, C. Bruneton, P. Borgeaud, A. V. Stirling, C. Caverzasio, J. P. Guillaud, M. Yvert, and B. Amblard, Phys. Letters 20, 75 (1966).
9. G. Höhler, J. Baacke, H. Schlaile, P. Sonderegger, Phys. Letters 20, 79 (1966).
10. Charles B. Chiu and John D. Stack, Phys. Rev. 153, 1575 (1967).
11. V. Barger and P. Weiler, Wisconsin Preprint, July 1969, to be published in Phys. Letters.
12. G. Chew, Comments on Nuclear and Particle Physics 1, 58 (1967).
13. J. Beaupre and E. Paschos, "Regge analysis of π^o and π^+ photoproduction at backward angles," Report No. SLAC-PUB-655, Stanford Linear Accelerator Center, Stanford University, Stanford, California (1969);
    E. Paschos, Phys. Rev. Letters 21, 1855 (1968).

CHAPTER III

EXPERIMENTAL CONSIDERATIONS

The Measurement

The experiment was designed to measure backward π^0 photoproduction as a function of center-of-mass energy and four momentum transfer squared, u, using the so called "missing mass"* technique. At each of the primary beam energies of 6, 8, 12, and 18 GeV: (a) the π^0 cross section was measured at six to eight u values covering the range from 0 to -1 $(GeV/c)^2$ and (b) at two angles, photoproduction cross sections were measured out to missing mass squared values around 1.5 GeV^2. The latter provided preliminary information on cross sections for η and ρ production, and a search for any other mass peaks that might be present, as well as giving data over a wide range in missing mass against which to make a fit that would account for the nonresonant background arising from multiple pion production. (See Chapter IV.)

Additionally, at each of the primary energies, forward π^+ photoproduction was measured at the tip of the bremsstrahlung spectrum at a few angles. This measurement could be made very quickly, and provided (a) a check on overall normalization, (b) an internal consistency check on the apparatus — the measurement was made at each energy both before and after taking the π^0 data, (c) a measure of any mismatch in momentum setting between spectrometer and switchyard, and (d) the width of the resolution function for the instrumentation.

In addition to determining the u dependence of the π^0 cross section, the above plan allowed that the data be cross plotted yielding the s (center-of-mass energy squared) dependence of the data; i.e., curves of $d\sigma/du$ vs s for constant values of u. The results obtained are presented in Chapter V.

---

*See Appendix A.

Experimental Approach

The final state for backward photoproduction of π^o mesons at high energy consists of the meson moving backward, i.e., opposite to the direction of the incident photon in the center-of-mass system, and a proton traveling forward. For center-of-mass π^o angles near 180^o, the proton has a laboratory angle near zero degrees and a momentum some 400 MeV/c above that for the photon which initiated the reaction. For this situation u is approximately 0. With increasing proton laboratory angle, out to u of -1 $(GeV/c)^2$ and more, it remains true that the momentum of the final state proton associated with the π^o is greater than that for protons associated with any other known photoproduction process. A sole known exception is that of backward Compton scattering which, however, is expected to be negligible in this experiment. (See Fig. 3.1 and associated note.) Figure 3.2 (a-d) gives the relevant kinematics plots. Those protons therefore, reside in what might be termed a "kinematic free region." It is this point which makes a measurement of the π^o cross section feasible when the reaction is studied using photons from the tip of the bremsstrahlung spectrum.

In view of the above, the experimental technique was to measure the momentum and scattering angle of the forward moving proton with a magnetic spectrometer. Then taking the energy of the photon to be that of the primary electron beam, the missing mass of the particle or particles associated with that proton was calculated and histogrammed. As described in Appendix A, π^o, η^o and other meson states will appear as steps in this histogram. (See Fig. A.1) π^o meson production appears as the initial step in such a histogram with the steps from η and ρ production superimposed upon a nonresonant background arising from multiple meson production.

Apparatus

The experiment was carried out at the Stanford Linear Accelerator Center (SLAC) using the magnetic spectrometer facilities[1] of that laboratory. The accelerator's[2] electron beam, momentum analysed and focused by the switchyard beam transport system, was passed through an 0.03 rl thick aluminum radiator and then swept vertically downward into a below-ground level beam dump. Figure 3.3 depicts schematically the setup. The photon beam, produced at the radiator, then passed through a series of two collimators, each followed by sweeping magnets, a helium filled Cerenkov cell which served as primary beam monitor, a Secondary Emission Monitor (SEM), a 40-inch long liquid hydrogen target centered on the pivot for the spectrometer and nonrotatable, and finally was dumped in a Secondary Emission Quantometer (SEQ). The SEQ consists of a series of parallel gold-surfaced-plates in an evacuated cavity with alternate plates held at minus a few hundred volts. For details concerning the beam monitors, see Ref. 3. Two calorimeters, each constructed in the form of a large cylindrically shaped metal core surrounded by the necessary insulation, served as total beam energy absorption devices against which the beam monitors were calibrated.

The hydrogen target cell was a rectangularly shaped container 40 inches long by 7 inches wide by 2.5 inches high with end windows of 0.005-inch stainless. A dummy cell of identical construction was mounted below the main hydrogen cell. A remotely controlled mechanism allowed either the liquid or the dummy target to be positioned in the beam thus making it easy to perform empty target measurements. Yields from the dummy target were taken for most of the angles at each energy and were found to be completely negligible.

Beam parameters varied according to the energy of the accelerator but those used at 8 GeV illustrate a set of operating conditions. The normal beam pulse repetition rate was 180 per second which resulted in an average intensity for the primary electron beam of 10 μamps before the momentum analyzing slits in the switchyard and 7.3 μamps following them (thus incident on the radiator) for 73% transmission through those slits. Such a beam intensity produced 1650 watts of photons from a 3% rl radiator which resulted in 800 watts of photons at the target after collimation for 48% transmission. At 18 GeV, transmission through the momentum analyzing slits was comparable, 40-50%.

While measuring the backward π^0 cross sections, nearly the full beam intensity (up to the beam breakup point) was used. Forward π^+ cross sections necessitated a reduction in beam intensity to the point where the fast electronics was receiving one event per two to three beam spills, a comfortable rate reasonably within the processing speed of the on-line computer system.

The SLAC 20 GeV/c spectrometer[1,4] detected protons with a gas filled differential Cerenkov counter and determined their kinematics using a series of four finger-hodoscopes. Scattering angles in the vertical and horizontal planes are measured with resolution $\delta\phi_0 = \pm 1.2$ mrad and $\delta\theta_0 = \pm 0.14$ mrad, momentum with resolution $\delta P = \pm 5 \times 10^{-4} P$ and horizontal displacement relative to the spectrometer axis with resolution $\delta x_0 = \pm 2$ cm. See Fig. 3.4 for a schematic of the detection system, and appendix B for a more complete description of its functioning. We note that momentum analysis is carried out with magnetic deflection in the vertical plane.

Optical parameters for the spectrometer are as follows:

Solid angle acceptance	$\Delta\Omega$	$\sim 10^{-4}$ ster
Vertical acceptance angle	ϕ_0	$\pm$ 10 mrad

Horizontal acceptance angle	θ_0	± 3 mrad
Momentum acceptance	$\delta P/P\|_{spectr}$	± 1.5%
Momentum dispersion		3.25 cm/%
Angular dispersion		1.62 cm/mr

The detection system was interfaced into an on-line SDS 9300 computer (32 K core, 1.75 μsec cycle time) which treated the data on an event by event basis, accepting at most one event per beam pulse and logging that on magnetic tape before performing analysis upon it.

A diagram of the electronic logic is shown in Fig. 3.5. In its most basic form it functioned as follows. A coincidence between the three trigger counters Tr1, Tr2, Tr3, termed a "true" event, triggered a monostable gate whose output was fanned out to provide gating pulses for signals from each phototube in the detection system. This gate limited the event rate to one per accelerator pulse, the maximum which the computer could process. It was possible to create a hardware veto of the "true" event pulse using the output of a gas filled threshold Cerenkov counter; this was a useful procedure during the backward π^o measurements when the number of π^+'s was a sizable fraction of the detected particles. A description of the buffer complex into which the pulses from the phototubes of the detection system were fed, the interfacing of signals into the on-line computer and the details of the on-line data acquisition system including the computer can be found in Ref. (5).

Rates

The number of events, ΔH, into bin "MM" of the missing mass histogram is given by Eq. (III. 1) as

$$\Delta H(MM) = \Delta N_\gamma N_A \left.\frac{d\sigma}{d\Omega}\right|_{lab} \Delta\Omega|_{bin} \, EFF \qquad \text{(III. 1)}$$

EFF = efficiency factor for the detection system

$\Delta\Omega\big|_{bin}$ = solid angle acceptance of the missing mass bin (ster)

$d\sigma/d\Omega\big|_{LAB}$ = laboratory cross section to be measured (ub/ster)

N_A = effective number of atoms per cm^2 in the target

ΔN_γ = number of incident photons

Re-expressing ΔN_γ as detailed in Appendix A (Eq. (A.3) and (A.4)) with the notation defined there, namely

$$\Delta N_\gamma = NEQQ \frac{\lambda}{K} \frac{\partial K}{\partial P} \Delta P \qquad \text{(III.2)}$$

and inserting this result into Eq. (III.1) above after multiplying and dividing that equation by P, the spectrometer momentum, re-expresses the number of events into the missing mass bin in terms of the momentum bite, $\Delta P/P$, for that bin as

$$\Delta H(MM) = NEQQ\ \lambda\ N_A \frac{P}{K} \frac{\partial K}{\partial P} \frac{d\sigma}{d\Omega}\bigg|_{LAB} \left(\Delta\Omega \frac{\Delta P}{P}\right)\bigg|_{bin} EFF \qquad \text{(III.3)}$$

Using this equation, the measured ΔH gives $d\sigma/d\Omega$, the desired cross section; the manner in which all the other quantities in Eq. (III.3) are related to directly measured quantities is discussed in Chapter IV and Appendix A.

Resolution

Momentum resolution $\Delta P/P$ (full-width — half maximum) attainable during the experiment was dependent upon four major contributions:

(a) $\Delta P/P\big|_{\Delta E}$ of the incident beam

(b) $\Delta P/P\big|_{\Delta}$ height of the photon beam at the target, Δh

(c) $\Delta P/P\big|_{rise}$ width of the tip of the bremsstrahlung spectrum

(d) $\Delta P/P\big|_{\Delta}$ height due to depth of field effect for a 40-inch long target, $\Delta h\phi$

These four contributions are individually detailed as follows:

(a) $\Delta P/P$ due to energy spread of the photon beam is equal to $\Delta E/E$

(b) Vertical height of the photon beam at the target, Δh

$$\left.\frac{\Delta P}{P}\right|_{\Delta h} = \frac{1}{P}\left(\frac{\partial P}{\partial y_d}\right)\left(\frac{\partial y_d}{\partial y_0}\right)\Delta h = 0.284 \times 10^{-2}\,\Delta h$$

where $\partial P/\partial y_d$, is the reciprocal of the momentum dispersion at the focal plane of the detection system and $\partial y_d/\partial y_0$ (the magnification) is a measured matrix element for the spectrometer optics which couples the vertical displacement of the ray at the target (y_0) to its vertical displacement at the focal plane for the system (y_d).

(c) Rise width 10% - 90% of the "flat top" value at the tip of the bremsstrahlung spectrum for the 0.03 rl radiator was 60 MeV. Therefore, $\left.\Delta P/P\right|_{brem} = 0.060/P$. See Fig. A.1.

(d) The depth of field effect arises due to particles produced in the target at points other than on its vertical plane at mid-length and with vertical angles, ϕ_0, not equal to zero degrees. The trajectories of such particles intersect the target's mid-length vertical plane (the object plane for the spectrometer optics) at vertical heights $\Delta h\phi$, not equal to the true vertical height at which they were produced in the target. The contribution of this effect to the effective momentum resolution was estimated as

$$\left.\frac{\Delta P}{P}\right|_{\Delta h\phi} = 0.284 \times 10^{-2}\,\Delta h\phi = 0.284 \times 10^{-2}\,\frac{1}{2}(100\text{ cm})\,\frac{1}{2}(20\text{ mrad})$$

The factor $\frac{1}{2}(100$ cm) equals the maximum distance from the target's vertical mid-plane at which a particle can be produced. The term $\frac{1}{2}(20$ mrad) is an average effective full width vertical angle spread which these particles can have. Consequently,

$$\left.\frac{\Delta P}{P}\right|_{\Delta h\phi} = 0.284 \times 10^{-2}(0.5\text{ cm})$$

Finally, combining these four contributions in quadrature, gives the effective momentum resolution $\Delta P/P_{eff}$

$$\left.\frac{\Delta P}{P}\right|_{eff} = \left[\left(\frac{\Delta E}{E}\right)^2 + \left(\left.\frac{\Delta P}{P}\right|_{\Delta h}\right)^2 + \left(\left.\frac{\Delta P}{P}\right|_{brem}\right)^2 + \left(\left.\frac{\Delta P}{P}\right|_{\Delta h\phi}\right)^2\right]^{1/2}$$

The following table lists, as a function of primary beam energy, items (a) and (b) above in the second and third columns and the calculated effective momentum resolution in column four.

Beam energy (GeV)	$\frac{\Delta E}{E}$(%)	Photon beam height, Δh (cm)	$\left.\frac{\Delta P}{P}\right\|_{eff}$(%)
6	0.76	1.68	1.23
8	0.56	1.26	0.92
12	0.36	0.84	0.62
18	0.21	0.56	0.41

The missing mass resolution, ΔMM^2, is related to the effective momentum resolution by

$$\frac{\Delta MM^2}{P} = 2M \left.\frac{\Delta P}{P}\right|_{eff} \qquad \text{(III.4)}$$

which expression, results from differentiating Eq. (A.1) with respect to P and making the approximation of high energy $\left(\frac{P}{E} \sim 1\right)$ and small θ ($\cos\theta \sim 1$).

The width of the step rise for the 10% - 90% points in the missing mass histogram, as determined from the best fits to the high statistics forward π^+ photoproduction data (see next chapter) provided an experimental measure of the missing mass resolution. Comparing the values for the missing mass resolution as calculated from Eq. (III.4) with those values determined for it from the fits to the forward data indicated agreement on the 10 to 15% level. Therefore it is concluded that the major contributions to the missing mass resolution were understood.

REFERENCES FOR CHAPTER III

1. SLAC User's Handbook, Stanford Linear Accelerator Center, Stanford University, Stanford, California.

2. R. B. Neal, Ed., The Stanford Two Mile Accelerator, (W. A. Benjamin, Inc. New York, 1968).

3. G. E. Fischer and Y. Murata, "A beam monitor system for high-intensity photon beams in the multi-BeV range," Report No. SLAC-PUB-605, Stanford Linear Accelerator Center, Stanford University, Stanford, California (1969).

4. W. H. K. Panofsky, Proc. of Internat'l. Symposium on Electron and Photon Interactions at High Energies, Hamburg, Germany (1965).

5. A. Boyarski, "The on-line control, analysis and display for the SLAC multi-GeV/c spectrometer," Report No. SLAC-PUB-559, Stanford Linear Accelerator Center, Stanford University, Stanford, California (1969).

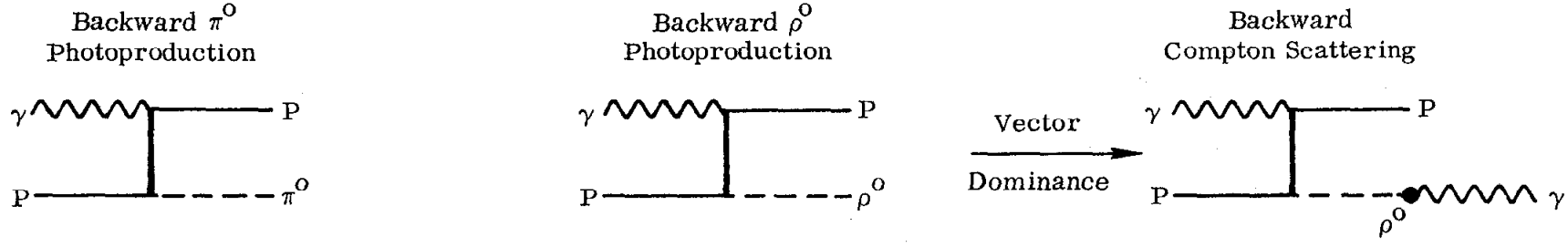

1349A11

$$\left.\frac{d\sigma}{du}\right|_{\gamma p \to p\gamma} = \frac{\alpha}{4}\left(\frac{4\pi}{\gamma_\rho^2}\right)\left.\frac{d\sigma}{du}\right|_{\gamma p \to p\rho^o}$$

transverse

Presently

$$0.42 < \frac{\gamma_\rho^2}{4\pi} < 1.1$$

Fig. 3.1--Backward Compton scattering from the proton produces protons with momentum about 10 MeV/c higher than that for the protons associated with backward photoproduction of pi-zero mesons. The kinematics for the latter process are shown in Figs. 3.2(a-d). The magnitude of the cross section for backward Compton scattering, however, would be some 250 to 500 times smaller than that for the backward photoproduction of neutral rho mesons according to the value assumed for $\gamma_\rho^2/4\pi$ in the Vector Dominance Model. (See diagram above.) As indicated in Chapter V, the rho and pi-zero cross sections are comparable in magnitude and consequently the contribution from the Compton scattering is a negligible effect.

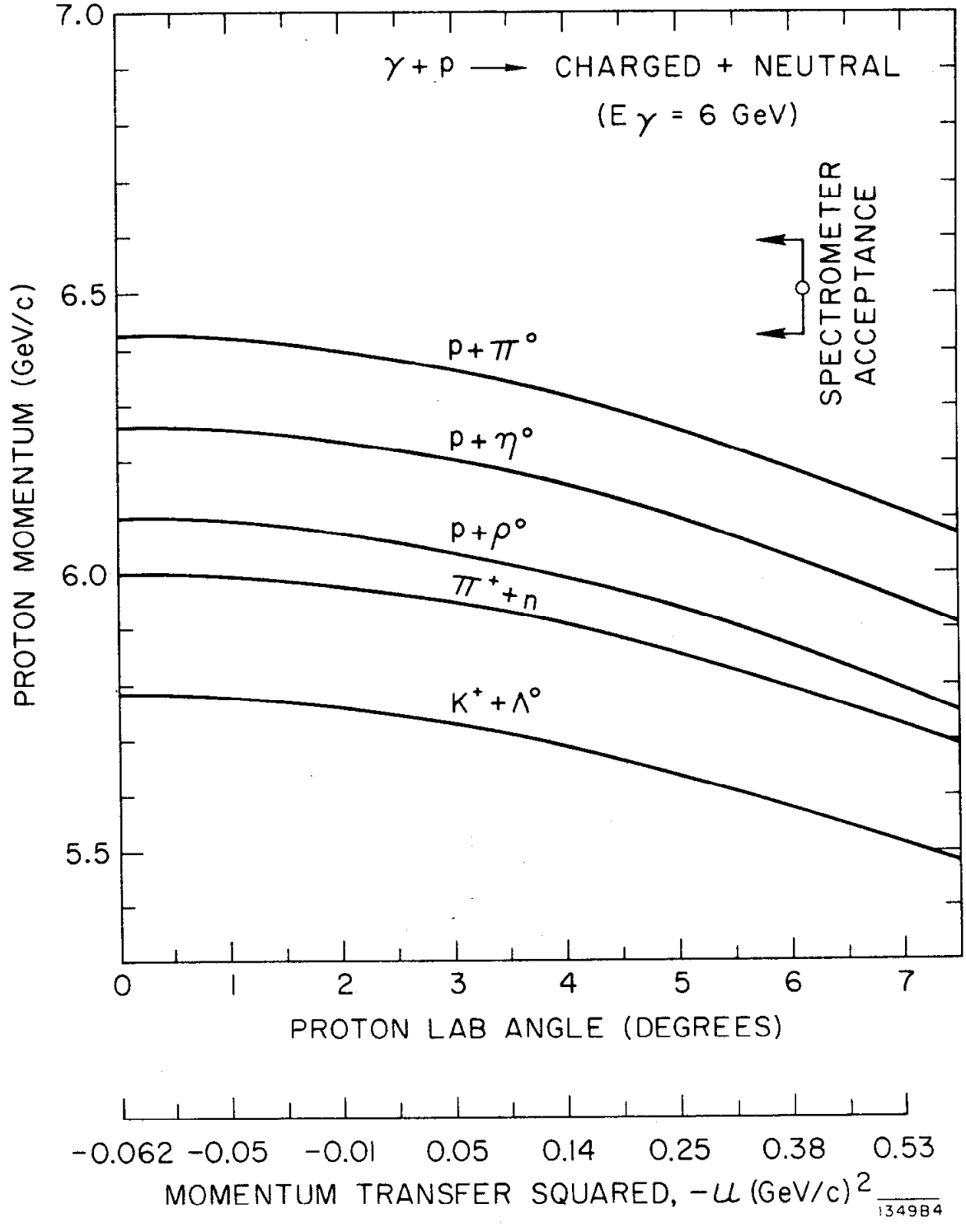

Fig. 3.2a--Laboratory momentum vs laboratory angle for the forward moving charged particle in the reaction $\gamma + p \longrightarrow$ charged + neutral with $E_\gamma = 6$ GeV.

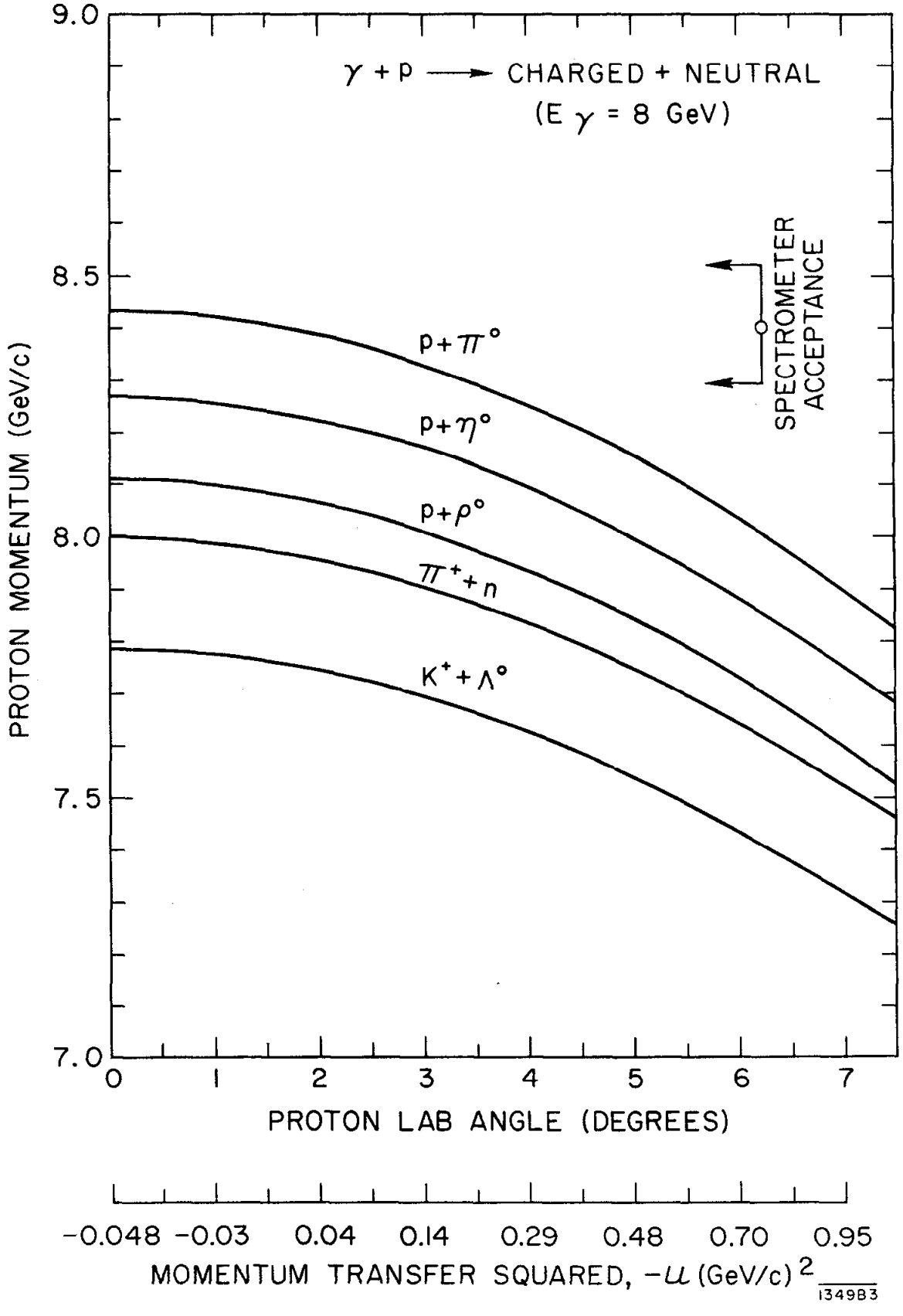

Fig. 3.2b--Laboratory momentum vs laboratory angle for the forward moving charged particle in the reaction $\gamma + p \longrightarrow$ charged + neutral with $E_\gamma = 8$ GeV.

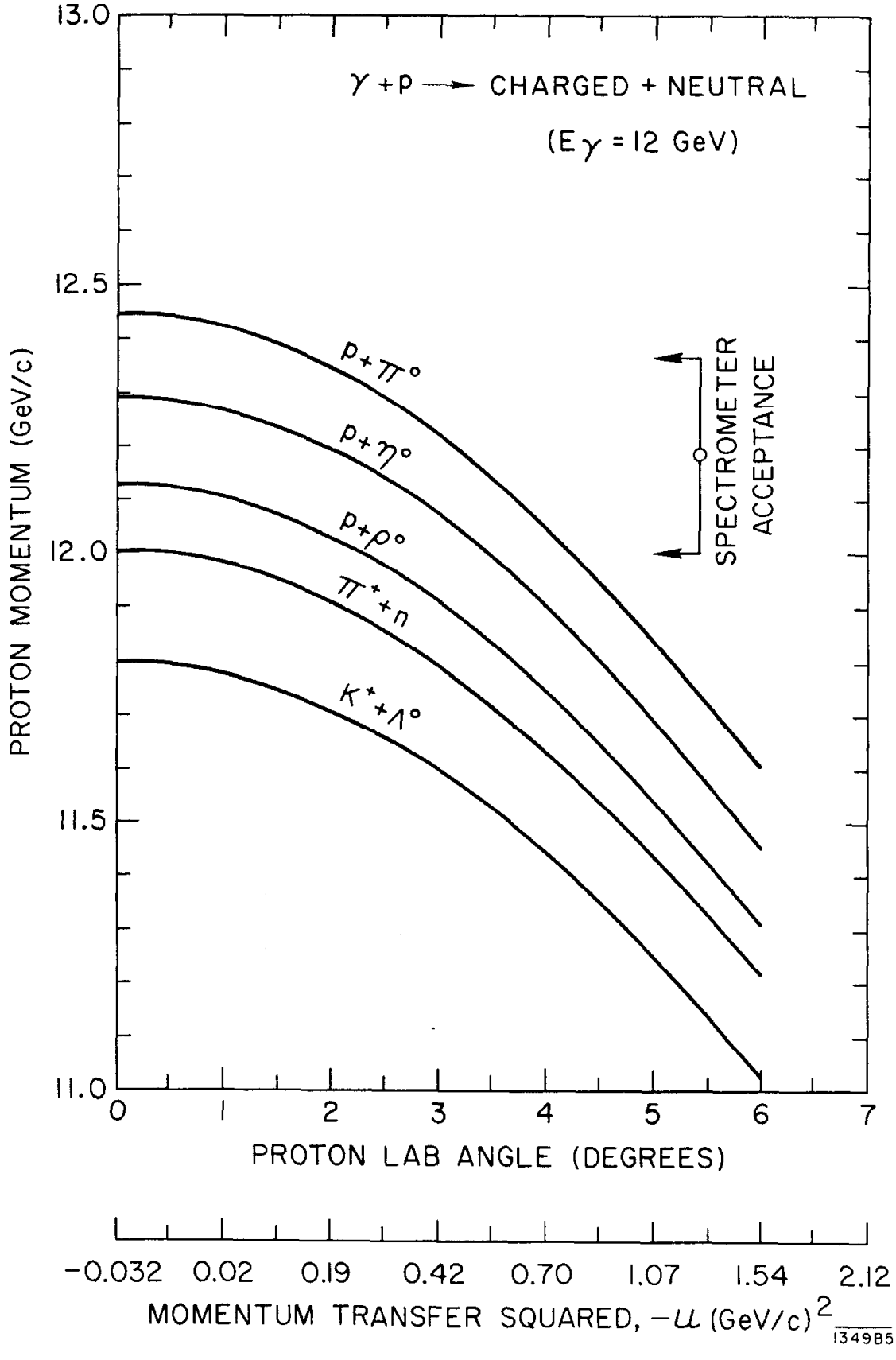

Fig. 3.2c--Laboratory momentum vs laboratory angle for the forward moving charged particle in the reaction γ + p—→charged + neutral with E_γ = 12 GeV.

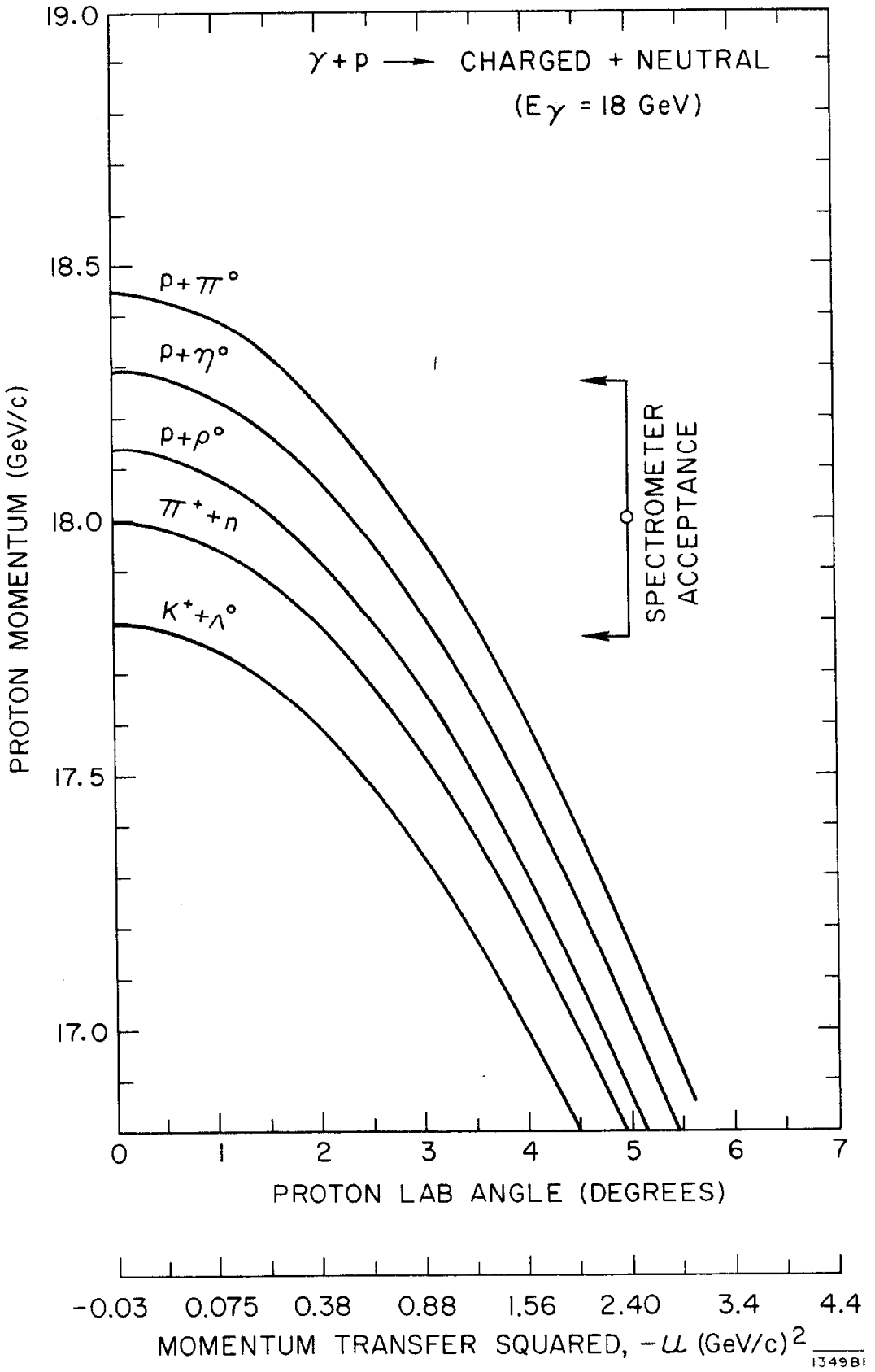

Fig. 3.2d--Laboratory momentum vs laboratory angle for the forward moving charged particle in the reaction $\gamma + p \longrightarrow$ charged + neutral with $E_\gamma = 18$ GeV.

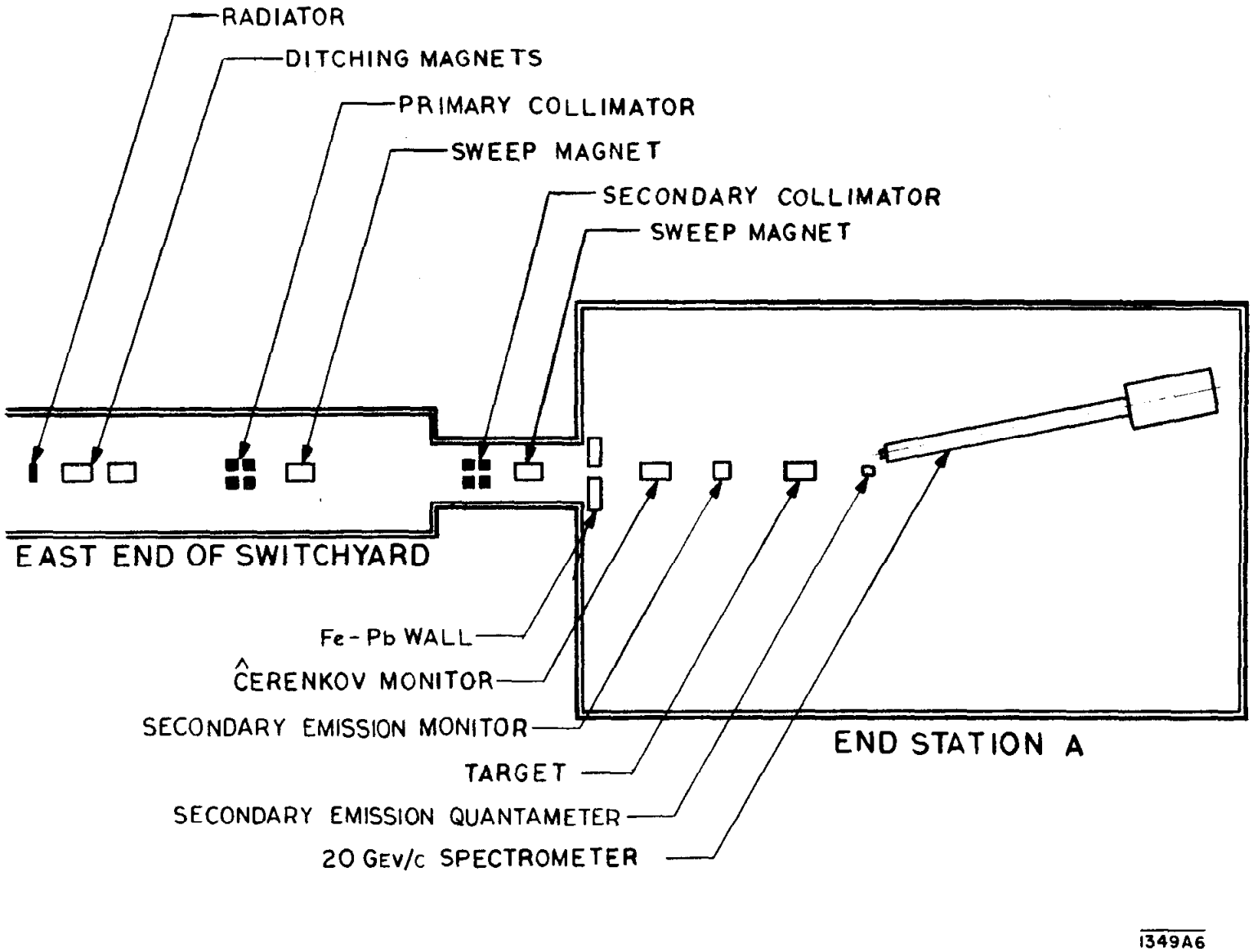

Fig. 3.3--Schematic representation of the experimental apparatus.

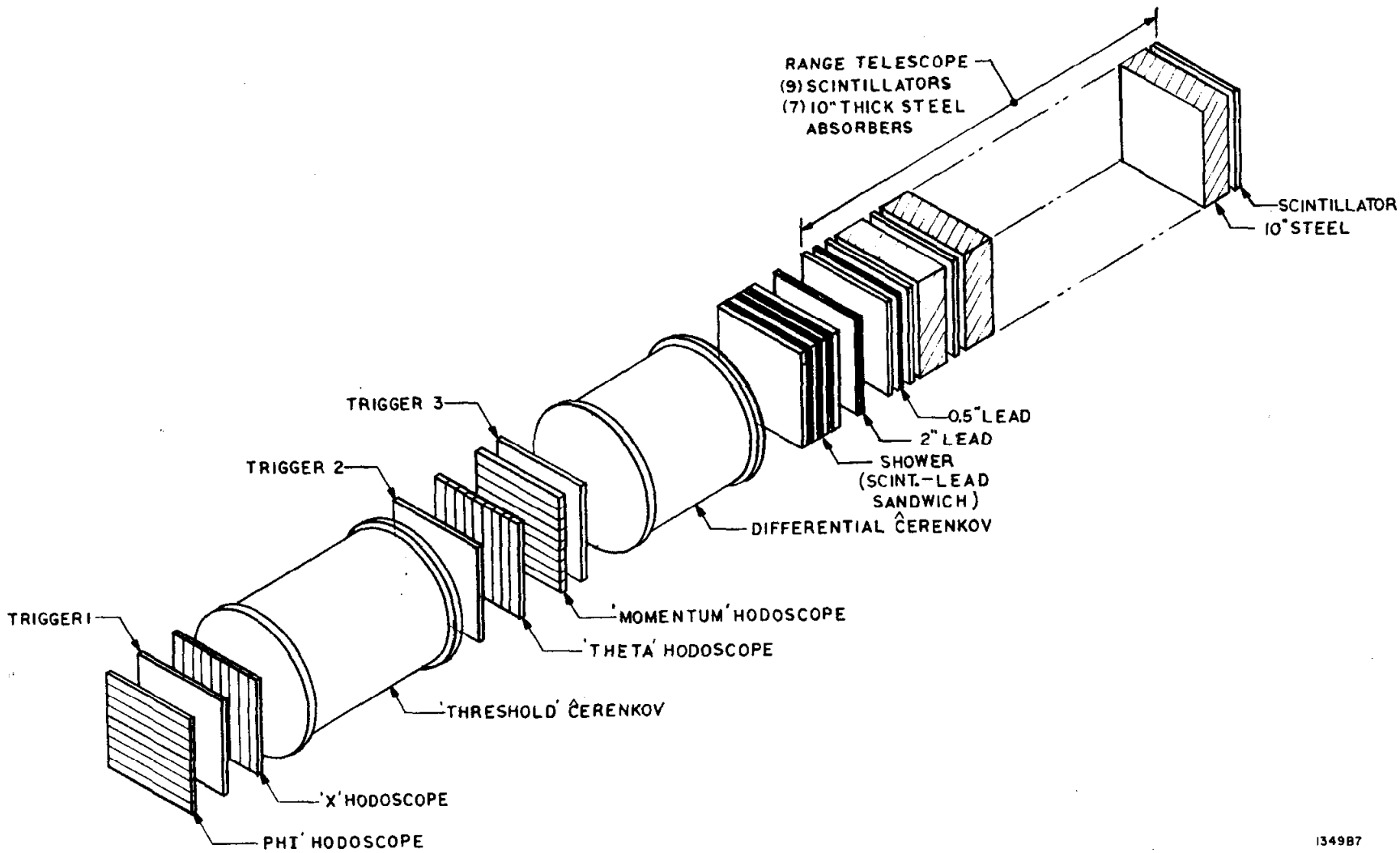

Fig. 3.4--Schematic representation of the particle detection system contained in the cement — shield "hut" of the 20 GeV/c spectrometer.

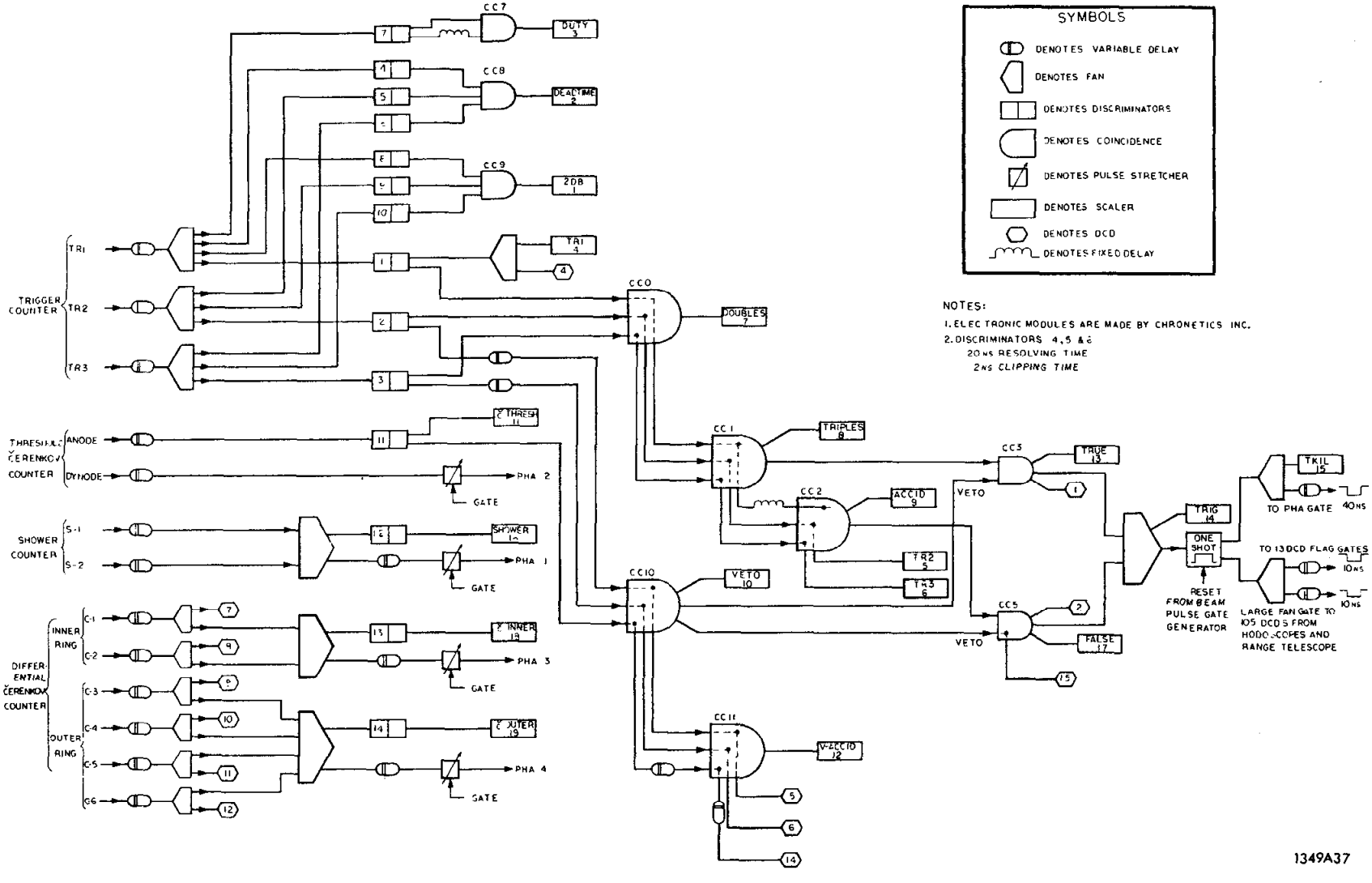

Fig. 3.5--Logic diagram for the Fast Electronics.

CHAPTER IV

REDUCTION OF THE DATA

Analysis of the raw data, recorded event by event on magnetic tape, proceeded according to the logic diagram in Fig. 4.1. (Consult Appendix B for details of the detection system.) The analysis programs first decoded the hodoscope and range telescope information into bin numbers. The event was tagged "good" if it passed the following checks; otherwise it was rejected.

Event Acceptance Criteria

(a) Single tracks in each hodoscope. (If a hodoscope did not contain a track (~ 5% of events) or had multiple tracks (~6% of events) the event failed. The number of such events and the reason for the failure was tabulated.)

(b) Horizontal angle ψ_H* in the detection system, within preset bounds (97%).

(c) Vertical angle ψ_V in the detection system, within preset bounds (99%).

(d) Event's trajectory did not come from a wall in the spectrometer (92%).

Histogramming

The characteristics of the "good" events were then tabulated in the following histograms.

"Phi"-hodoscope	Number of events vs bin number
"X"-hodoscope	Number of events vs bin number
"Momentum-theta"-hodoscope	P bin (x-axis) vs θ bin (y-axis) with number of events plotted along the z-axis
Shower-range	Shower counter Pulse Height Analyzer (PHA) channel number (x-axis) vs bin number (y-axis) to which the particle penetrated in the range telescope with number of events plotted along the z-axis

*See symbol table for definition of symbols.

Differential-Cerenkov counter	Channel number for Inner region PHA (x-axis) vs channel number for Outer region PHA (y-axis) with number of events plotted along the z-axis
Threshold-Cerenkov counter	Number of events vs PHA channel number.

These histograms appeared as part of the printed output from the computer analysis of each data run.

Classifying of Events

With the histogramming completed, the event was checked for "type." For this purpose, the range telescope is used to identify muons and the shower counter to identify electrons. All other events are classified as hadrons. Figure 4.2a, b shows two computer outputs of the shower-range histogram for the spectrometer set at 1.5^{o} and 5^{o}. Superimposed upon the outputs are drawn the boundaries chosen for distinguishing particle "types." If the event fell within the region marked, electron, pedestal, or muon, it was counted as such and its analysis ended. Therefore, the subsequent discussion deals exclusively with the hadrons which fell within the region marked hadrons in Fig. 4.2. The hodoscope coordinates for each hadron event were transformed into target space coordinates (see Appendix B) and the event was checked to determine whether it came from within a fiducial volume defined in the target space.

Spectrometer Acceptances

Two spectrometer acceptances (fiducial volumes) were defined by the computer programs in terms of target space coordinates, the boundaries for the first being totally contained within the boundaries for the second. Both acceptances were smaller in extent than the total acceptance of the spectrometer but for each it was believed that the optics is fully understood.

The boundaries for the larger spectrometer acceptance (referred to as the "Full" acceptance) are expressed, with F = 1.0, as

$$\left\{\begin{array}{ll} -3.0\ F \le x_0 \le +3.0\ F & x_0 \text{ in centimeters} \\ \theta_{min}(x_0) \le \theta_0 \le \theta_{max}(x_0) & \theta_0 \text{ in milliradians} \\ -1.35\ F \le \delta \le +1.53\ F & \delta \text{ in percent} \\ \phi_{min}(\delta) \le \phi_0 \le \phi_{max}(\delta) & \phi_0 \text{ in milliradians} \end{array}\right\} \qquad \text{(IV.1)}$$

$$\theta_{min}(x_0) = \max(-3.6\ F;\ 0.089\ x_0^2 - 0.6 x_0 - 4.2\ F)$$

$$\theta_{max}(x_0) = \min(3.2\ F;\ -0.11\ x_0^2 - 0.67\ x_0 + 3.4\ F)$$

$$\phi_{max}(\delta) = -0.25\ \delta^2 + 7.5\ F$$

$$\phi_{min}(\delta) = 0.625\ \delta^2 - 1.25\ \delta - 5.5\ F$$

where θ_0 and ϕ_0 are the projected scattering angle in the horizontal and vertical planes respectively, $\delta = \dfrac{(P-P_{spectr})(100)}{P_{spectr}}$ is the percent momentum displacement, and x_0 is the horizontal displacement at the target relative to the spectrometer axis.

Synthesis of the data from the optics measurements on the spectrometer indicated that the fiducial volume defined by the above relations with $F \le 1$, actually was completely contained within the physical boundaries defined by the walls of the spectrometer vacuum chamber.

The second spectrometer acceptance (referred to as the "Reduced" acceptance) was defined through the above relationships by setting F = 0.9 and thereby was totally contained within the Full acceptance. By comparing cross sections calculated with the events from each of the acceptances, a check on the understanding of these fiducial volumes was provided.

Thus using the acceptance boundaries defined above, each hadron event was labeled according to whether it entered the spectrometer outside the boundaries

of the Full acceptance, in which case its analysis ended, inside the boundaries of the Full or inside the boundaries of the Reduced acceptance.

Hadrons passing the acceptance test were identified (for example — pion, kaon, or proton) using the information from the Cerenkov counters. If the hadron was determined to be the "type of interest," for example a proton when the particular run was aimed at measuring the protons associated with π^o production, the event was then passed to the missing mass routine which calculated and histogrammed a value for the missing mass associated with it. Analysis of the event ended at this point.

With the analysis of the last event in a given run completed, a cross section $d\sigma/d\Omega\big|_{bin}$, was calculated for each of the missing mass bins.

Calculation of the Cross Section

Solving Eq. (III.3) for $d\sigma/d\Omega\big|_{bin}$ provides the equation used by the computer to evaluate the cross section per missing mass bin; namely

$$\left.\frac{d\sigma}{d\Omega}\right|_{bin} = \frac{\Delta H(MM)}{\left[\Delta\Omega\Delta P\right]_{bin} N_A \, EFF \, NEQQ \, \frac{\lambda}{K_0} \, \frac{\partial K}{\partial P}} \qquad (IV.2)$$

where $\Delta H(MM)$ is the number of events in the "MM" bin of the missing mass histogram, $\Delta\Omega\Delta P\big|_{bin}$ is the solid angle times momentum acceptance for that bin, N_A, the number of target atoms per cm^2, EFF, the efficiency factor for the detection system. NEQQ is the number of "equivalent quanta" detected by the beam monitor, $\lambda \simeq 0.87$ is a quantity related to the shape of the bremsstrahlung spectrum, K_0 is the maximum photon energy, and $\partial K/\partial P$ is the Jacobian relating outgoing particle momentum and incident photon energy. We have replaced the factor K in Eq.(III.3) by K_0; the reason for this is explained in Appendix A. The symbols in the denominator of Eq.(IV.2) and their relation to physically measurable quantities are discussed subsequently.

Spectrometer Acceptance per Missing Mass Bin

The spectrometer acceptance per missing mass bin is defined by the integration limits in the following equation.

$$\Delta\Omega\Delta P\Big|_{bin} \equiv \frac{1}{2x_0}\left[\int_{-x_{0_{max}}}^{+x_{0_{max}}} dx_0 \int_{\theta_{min}(x)}^{\theta_{max}(x)} d\theta_0\right]\left[\int_{P_{min}}^{P_{max}} dP \int_{\phi_{min}(P)}^{\phi_{max}(P)} d\phi_0\right] \qquad \text{(IV.3)}$$

P_{min}, P_{max}, $\left(P_{\substack{max\\min}} = P_{spectr}(1 \pm .01\,\delta)\right)$ and x_0 are given by Eq. (IV.1). θ_{min}, θ_{max}, ϕ_{min}, ϕ_{max} are restricted to be the smaller (in absolute value) of (a) the limits imposed on those coordinates by the spectrometer acceptance boundaries as defined by Eq. (IV.1) or (b) the limits as imposed on those coordinates by the boundaries of the particular missing mass bin. Division by $2x_0$ averages the acceptance over the target length seen by the spectrometer. The true effective target length is inserted into the cross section calculation through the factor N_A.

The acceptances $\Delta\Omega\Delta P\Big|_{bin}$ for each missing mass bin in each of the two spectrometer acceptances, were numerically evaluated by the computer for the particular angle and momentum setting of the spectrometer, before commencing analysis of the event data in a data run.

Jacobian $\partial K/\partial P$

The expression for the Jacobian, $\partial K/\partial P$, is obtainable from Eq. (A.1) treating "MM^2" and θ as constants and differentiating. The result is

$$\frac{\partial K}{\partial P} = \left.\frac{(M_T + K_0)\frac{P}{E} - K_0 \cos\theta}{(P\cos\theta + M_T - E)}\right|_{\substack{P = P_{sp}\\ \theta = \theta_{sp}\\ E = \left[P_{sp}^2 + M_D^2\right]^{1/2}}} \qquad \text{(IV.4)}$$

Number of Equivalent Quanta

The number of equivalent quanta, NEQQ, is determined by multiplying the charge increment, ΔQ (coulombs) for the current integrator associated with the primary beam monitor in a given run, by the calibration constant, JM (joules/coulomb) for that beam monitor and dividing by the beam energy, K_0. Thus

$$NEQQ = \frac{\Delta QJM}{K_0} = \frac{E_{tot}}{K_0} \qquad (IV.5)$$

The quantity ΔP NEQQ $\frac{\lambda}{K_0} \frac{\partial K}{\partial P}$ is the number of photons in the bremsstrahlung beam which have the correct energy for producing protons in a missing mass bin. NEQQ and the quantity λ are further discussed in Appendix A.

Number of Effective Target Atoms, N_A

Two problems arise in trying to determine the number of effective target atoms;

(a) With the 40-inch long target the number of atoms seen by the spectrometer acceptance is not constant as the spectrometer is rotated in angle; i.e., the effective target length changes.

(b) Due to attenuation of the photon beam as it passes along the target, the relative yield per atom for the upstream portion of the target is different from that for the downstream portion.

In order to determine the effective number of target atoms, calculations and measurements were made using two additional test targets which were included in the target assembly. The first of these, the "distributed" target, was constructed from 40 aluminum sheets, 0.01 inches thick, spaced at one-inch intervals, thus representing the physical length and thickness (rl) of the hydrogen target. The second target had its 40 foils, identical to those in the "distributed" target, bunched together forming a "point" target. This target with thickness 0.4 inches in the

beam direction and transverse dimension of approximately a centimeter square, the beam spot size, was effectively a "point" target in view of the coarse spacial resolution provided by the "X-Theta" hodoscope system.

With the point target, acceptance characteristics could be measured directly. As seen by the spectrometer, this target which actually had a negligible size in its transverse dimension (along the x_0 direction) appeared to be a target with a transverse size about 5 centimeters. Specifically, the target appeared to have a transverse distribution described by the normalized resolution function $R(x_0) = 0.171 \exp\left(-(x_0 - 0.2)^2/2(2.34)^2\right)$. The 0.2 displacement effect appearing in the function corresponds to the fact that the detector hodoscope assembly was not positioned precisely on the spectrometer axis.

For the actual experiment with the long nonpoint target or correspondingly for the calibration measurements with the "distributed" target, the true source points did not all lie on the spectrometer axis. Accordingly, we used a generalized resolution function $R(x_0, x')$ where x' is the true transverse location of a source point (transverse relative to the spectrometer axis) and x_0 the apparent source location as seen by the spectrometer. (x_0 and x' are measured at the point where the particle crosses the effective source plane at the target mid-length.) This function was for practical purposes dependent only on $x_0 - x'$ and thus is well described by the expression $R(x_0 - x') = 0.171 \exp\left((x_0 - x' - 0.2)^2/2(2.34)^2\right)$. We note that even for x_0 values at the edge of the acceptance region defined by Eq. (IV.1) there are in-scattering effects from true source points outside that x_0 value which compensate closely the out-scattering effects from true source points inside that x_0 value.

The calculation of the effects listed as (a) and (b) above is facilitated by introducing a source strength function $\psi(x', \theta_{spectr})$ where x', as defined above,

is the actual transverse location of a source point relative to the spectrometer axis. See Fig. 4.3. ψ was calculated for each value of θ_{spectr} used in the experiment; ψ was normalized to give

$$\int_{-\infty}^{\infty} \psi(x', \theta_{spectr})\, dx' = 1.$$

The true yield from the "distributed" and "point" targets can then be calculated by including the resolution function, $R(x_0 - x')$, and the source strength function, $\psi(x', \theta_{spectr})$, into the expression describing the spectrometer acceptance. Defining

$$I_{P\phi_0} \equiv \int_{P_{min}}^{P_{max}} dP \int_{\phi_{min}(P)}^{\phi_{max}(P)} d\phi_0 \qquad \text{(IV.6)}$$

and

$$I_{x_0\theta_0} \equiv \int_{-3F}^{+3F} dx_0 \int_{\theta_{min}(x_0)}^{\theta_{max}(x_0)} d\theta_0 \int_{-\infty}^{\infty} dx'\ R(x_0 - x')\, \psi(x', \theta_{spectr}) \qquad \text{(IV.7)}$$

with the limits on the integrals as given by Eq. (IV.1) with F = 1.0,

$$\text{YIELD} \propto I_{P\phi_0} I_{x_0\theta_0}. \qquad \text{(IV.8)}$$

Therefore, evaluating the right side of the proportionality IV.8 with $\psi(x', \theta_{spectr})$ describing the "distributed" target, and then dividing that result by evaluating the same expression but with ψ now taken to be a delta function — the representation of the source strength for a "point" target, provided a calculated ratio of yields for "point" and "distributed" target.

Experimentally this same ratio was determined by measuring the forward π^+ yield to high statistics, first from the "distributed" and then from the "point" target for several angular settings of the spectrometer. The spectrometer was set to a low momentum ($\sim 1/3$ the maximum momentum of the photon beam). The

π^+ distribution varied less than 2% across the spectrometer acceptance. Figure 4.4 shows the ratios for both the measured and calculated yields. From the general agreement between the two curves, it is concluded that the major contributions to the "effective acceptance" have been understood. Thus it remains to determine the number of target atoms, N_A.

In principle, when calculating a cross section, the number of events recorded, $\Delta H(MM)$, must be divided by, amongst other quantities, a factor which is the integral — over the acceptance limits of the spectrometer — of the response resolution function for the detection system R, folded with the spacial distribution of the target atoms, ψ, which can contribute events into the apparatus.

However, in the data analysis it was more convenient, for reasons of practicality, not to actually evaluate such an integral directly, but rather to split the calculation into two pieces; the first being the $\Delta\Omega\Delta P\big|_{bin}$ evaluation described above and the second to insert the number of target atoms through an EFfective Target Length, EFTL, multiplied by the number of atoms per square centimeter. To do so, EFTL must be defined such that its product with $\Delta\Omega\Delta P\big|_{bin}$ times the density of hydrogen, ρ, yield the same value as that given by (see Eq. (IV.9)) multiplying the total number of available atoms per cm^2 in the target, L(physical length) $\times \rho$ (hydrogen density) by an integral over the acceptance limits of the missing mass bin, which includes the resolution function for the instrumentation, R, and the target source density function, ψ. Therefore

$$\text{EFTL } \Delta\Omega\Delta P\big|_{bin}\rho = L\rho\left[I_{P\phi_0} I_{x_0\theta_0}(\theta_{spectr})\right]\Big|_{bin} \qquad \text{(IV.9)}$$

where the notation $\big|_{bin}$ indicates the integrals are evaluated for the range of variables applicable to a missing mass bin. Inserting Eq. (IV. 6) into Eq. (IV.3)

gives

$$\Delta\Omega\Delta P\Big|_{bin} = \frac{1}{2x_0} I_{P\phi_0} \int_{-3F}^{+3F} dx_0 \int_{\theta_{min}(x_0)}^{\theta_{max}(x_0)} d\theta_0 \Bigg|_{bin} \qquad \text{(IV.10)}$$

Now inserting (IV.10) into (IV.9) and solving Eq. (IV.9) for EFTL after canceling out the factor $I_{P\phi_0}$ from both sides, leaves the expression for effective target length as

$$EFTL = \frac{L\left[I_{x_0\theta_0}(\theta_{spectr})\right]_{bin}}{\frac{1}{2x_0}\left[\int_{-3F}^{3F} dx_0 \int_{\theta_{min}(x_0)}^{\theta_{max}(x_0)} d\theta_0\right]_{bin}} \qquad \text{(IV.11)}$$

The quantity N_A is then given by

$$N_A = \rho N_0 EFTL \qquad \text{(IV.12)}$$

where N_0 is Avagadros number.

The usefulness of introducing EFTL as a means of specifying N_A can be seen by noting that the ratio exhibited on the right side of Eq. (IV.11) retains its value whether evaluated for each missing mass bin or evaluated over the total spectrometer acceptance as defined by Eq. (IV.1). Therefore, with the boundaries for the spectrometer acceptance remaining fixed as the instrument was rotated in angle, the quantity EFTL could be calculated as a function of the spectrometer angle for each of the two spectrometer acceptances (Eq. (IV.1) with F = 1.0 and the F = 0.9) a simple time and the results tabulated. The data analysis programs could then use a single table interpolation scheme for determining the value of EFTL for a particular spectrometer angle and therefore, the value of N_A.

Detection Efficiency, EFF

The efficiency for the detection system, as written in Eq. (IV.1) consisted of two parts. The first, was the measured efficiency of the detection system for hadrons, EFH. The second consisted of a correction to allow for the fact that the

computer could read in at most one event per beam pulse, yet it was possible for more than one trigger to occur per beam pulse. The scaler called "Trig" in Fig. 3.5, counted the number of such triggers during a run. The ratio, R = (Number of Triggers)/(Number of events read by the computer) was then calculated and used as the correction. Combining both of the above, EFF was given by; EFF = EFH/R. R was typically 1.01 to 1.06.

The error in the cross section for a given missing mass bin was calculated by replacing ΔH(MM) in Eq. (IV.2) by its square root or "1," whichever was the larger. This completes the discussion of the quantities in Eq. (IV.2).

Corrections to the Data and Systematic Errors

Analysis of the data tapes ("off-line analysis") was performed subsequent to the data taking period in the manner discussed above and with the following items included.

(a) The acceptances per missing mass bin, $\Delta\Omega\Delta P\big|_{bin}$ were corrected for geometrical irregularities in the hodoscope construction and individual counter inefficiencies (typically 2-4%).

(b) Best values for the monitor calibration constants (joules/coulomb) were deduced from the monitor calibration runs and the run-by-run data reflecting monitor ratio stability (± 2%) as a function of time.

(c) Best values for various constraints, for example, the boundaries for the regions of the shower-range counter histogram, were determined from the histogram outputs obtained at the end of each run during the "on-line" analysis.

The raw cross sections σ_{raw} for each missing mass bin, which resulted from this "off-line" analysis, were then corrected for the effects listed below. The corrected cross section, σ_{corr}, was determined from

$$\sigma_{corr} = \sigma_{raw}(C_1 x C_2 \ldots x C_6);$$

the correction factors, C_1 through C_6 are detailed below.

(1) Hydrogen density: C_1 accounted for the difference between nominal values of density and target length used in the computer analysis and those furnished by the Hydrogen Target Group for $\sim 20^{\circ}K$. Correction: $2\% \pm 1.7\%$. Therefore $C_1 = 1.02 \pm .02$.

(2) Effective length of target: The measured "distributed/point" aluminum target ratio differed from the results predicted for it by the theoretical expression Eq. (IV.7) at the larger spectrometer angles, 5-7 degrees. Corrections correspond to $C_2 = 1.04 \pm .02$ at 5°, $1.08 \pm .02$ at 6° and $1.16 \pm .02$ at 7°.

(3) Interaction of photons in the hydrogen: Photons were absorbed in the hydrogen through the creation of electron pairs. The approximate size of this effect is 7/9(thickness of target in rl)=4.8%. A more detailed analysis including the thick radiator bremsstrahlung spectrum yielded 3.6%. Correction factor: $C_3 = 1.04 \pm .01$.

(4) Interaction of protons with hydrogen before exciting from the target: From the total cross section, σ_{Pr}, for protons on protons,[1] a correction was calculated for the loss of protons in the target

$$\sigma_{Pr} \times \left(\frac{\text{target length}}{2}\right) \times \left(\frac{\text{atoms}}{\text{cc}}\right) = 2.11 \times 10^{24}\, \sigma_{Pr}$$

Correction factor: $C_4 = 1.08 \pm .001$.

(5) Interaction of protons in the detection system: This effect had been previously determined[2] for the detection system via the technique of inserting various thicknesses of lucite sheet fore and aft of the hodoscopes and then extrapolating the measured yields to zero detector thickness. Synthesis of that data is contained in the expression $\text{COR} = \left[0.03 \pm 0.55/(\text{proton momentum (GeV/c)})\right] \pm .03$. Therefore $C_5 = (1.0 + \text{COR}) \pm .03$.

(6) Detection efficiency:

(a)	Cerenkov X shower counter efficiency, EFH in Eq. (IV.1)	6% ± 1.5%
(b)	Pedestals in shower counter corrected to zero detector thickness	7% ± 0.5%
(c)	Blank, single bit (only one of the required two or three hodoscope elements which form a bin, fired) and double track patterns in hodoscopes	5% ± 0.5%

Therefore $C_6 = (1.06)(1.07)(1.05) = 1.19 \pm .02$.

Additional uncertainties in the overall normalization arose from:

(1) Understanding of the shape for the bremsstrahlung spectrum ± 3%

(2) Width of the step rise used in the fitting program ± 5%

(3) Shift in missing mass scale used in the fitting program ± 5%

(4) Understanding of the spectrometer acceptance ± 3%

Thus the total uncertainty in the overall normalization was determined to be ± 10%.

The cross sections determined for the forward π^+ photoproduction data measured in this experiment, including the correction factors discussed above, were compared to similar measurements for those cross sections by A. Boyarski *et al.*,[3] with both sets of data plotted in Fig. 5.1. The measurements from the two experiments agree to within 5% substantiating the two independently used normalization procedures. Direct comparison of experimental values can be made only at 8 GeV. However, as has been observed in Ref. 3, the data scales with energy as $(s - M^2)^2$, thus allowing comparison of data measured at different energies.

Fitting — Extraction of Cross Sections from the Missing Mass Spectra

The missing mass spectra, quantitatively expressed by the cross sections per missing mass bin, were considered to be the summation of one or more steps (see Appendix A) centered around the squared rest mass value of the particle

represented by the step(s), plus a nonresonant background arising from multiple pion production. Normally the missing mass spectra extended only over the range for the π^o step with statistical errors per mass bin $\simeq \pm 12\%$. At each primary energy two spectra extended deep enough in missing mass, the "long" mass sweeps, to include the steps from η and ρ production. The so-called "ρ" step is in reality the sum of ρ^o and ω^o production as the resolution would not allow separation of the two.

Therefore, to extract cross sections for π^o, η and ρ mesons, a function was fit to the data in the form of a polynomial in squared missing mass to represent the background plus a series of steps, S_J, one for each of the backward produced neutrals. A least square fit was made to the data using the program "Solve" and a chi-squared criterion used to judge the "goodness of fit."

Fitting Function

The explicit form of the expression F(x), fitted to the data is given in Eq. (IV.11)

$$F(x) = \sum_{J=6}^{8} C_J S_J(x, M_J, W_J) + C_1 N_1(y) + C_2 N_2(y) + \sum_{J=3}^{5} C_J y^J \qquad \text{(IV.11)}$$

where:

$x \equiv MM^2$ (GeV^2)

$y = x - (2m_\pi)^2 - \Delta M^2$

$J = 6 \longrightarrow \pi^o$; $J = 7 \longrightarrow \eta$, $J = 8 \longrightarrow \rho$

m_π = mass of the charged π meson

ΔM^2 = shift in missing mass scale

C_J = parameters adjusted by fitting program

$$S(x, M, W) = 0.5\left(1.0 + \text{ERF}\left(\frac{x - M^2}{W^2}\right)\right) \qquad \text{(IV.12)}$$

W = width of step rise

M = central mass value for the step

$N_1(y), N_2(y)$ = respectively the linear and quadratic terms in the expansion for the nonresonant background, folded with the resolution function for the apparatus.

$$N_I(y) = \frac{1}{\sqrt{\pi}} \int_0^{\infty} y_0^I \, e^{-\left(\frac{y - y_0}{W}\right)^2} dy_0; \; I = 1, 2 \qquad \text{(IV.13)}$$

Determination of W and ΔM^2

The momentum of the analyzed electron beam is determined and regulated by the beam transport system in the beam switchyard. On the other hand, the spectrometer momentum is set independently of the beam switchyard. To check the overall cross calibration between switchyard (electron beam momentum — thus tip energy of photon beam) and spectrometer (momentum of detected particle), the forward π^+ data from $\gamma p \longrightarrow n\pi^+$, measured at the tip of the bremsstrahlung spectrum, was fit with a step of the form given by Eq. (IV.12) with the mass M, step width, W, and coefficient, C_π, varied to obtain the best fit. Comparison of the "M" value so obtained with the known mass of the neutron yielded the mass shift, ΔM^2. Typically, $\Delta M^2 \sim \pm .01$ GeV^2 with an uncertainty of ± 5%. The value found for W was used for the step width in the π^o and η steps and was added in quadrature to the inherent width of the ρ^o (120 MeV) to give the effective width of that step. A typical fit to the forward pion data is shown in Fig. 4.5.

Fitting the π^o Cross Section

Since the background beneath the π^o step was expected to be small on physical grounds, and restricted to be so by the forms assumed for it in the fitting function (Eq. (IV.11)), the value obtained for the π^o cross section was nearly free of variations made in the background terms. For example, at 1.9 degrees and 8 GeV (See Fig. A.1) the background below 0.35 GeV^2 was 25% of the total signal. At some angles this value went as high as 35%. Therefore, the π^o cross sections

were extracted at each angle, from the data with "x" less than 0.35 GeV^2 using only linear plus quadratic terms for the background, N_1 and N_2 in Eq. (IV.13). Inclusion of the cubic term in the background produced similar values for the π^o cross section as well as did reducing the upper missing mass limit to 0.3 GeV^2. A 7% error was combined with the statistical error calculated by the fitting program to allow for variations in the value of the π^o cross section due to different assumptions made for the background. The cross sections obtained from this procedure are given and discussed in Chapter V.

Fitting the η and ρ Cross Sections

To obtain satisfactory fits to the eight "long" mass sweeps, it was found necessary to include the polynomial background, the step for the π^o and in addition steps for the η and ρ. The significance of the η step was then determined by making a succession of fits to the data of a mass sweep, with the magnitude of the η step, c_η, fixed in each fit (but varied from fit to fit) and allowing the fitting program to minimize χ^2 by readjusting the magnitude of the π^o and ρ steps and the background parameters. The order of the background polynomial was held fixed during this procedure. Then plotting χ^2 vs the value of c_η used in those fits resulted in a parabolic shaped curve, an example of which is shown in Fig. 4.6 for the 8 GeV, 1.9^o mass sweep.

Statistically,[4] a one standard deviation effect in c_η corresponds to the change in c_η between its value at χ^2 minimum and its value when χ^2 has increased by one. It might be noted that this is also the error calculated for c_η by the fitting program for the situation in which c_η is an adjustable parameter together with those for the background and the π^o and ρ steps. For the 8 GeV, 1.9^o case represented in Fig. 4.6, χ^2 changes by 30 between the points where $c_\eta = 0$ and $c_\eta = 0.136$, its value at minimum χ^2; the significance of the c_η effect expressed in standard deviations can then be shown[4] to correspond to $\sqrt{30}$ or 5.5 standard deviations.

In terms of the Likelihood function, $\mathscr{L}$, with $\chi^2 = -2 \ln\mathscr{L}$, the ratio of the Likelihood function at χ^2 minimum ($\chi^2 = 44$) to its value at $\chi^2 = 74$ ($c_\eta = 0$) is $\exp(-15.15) = 2.6 \times 10^{-7}$. That is, the chance for c_η to be zero is on the order of one in four million. Furthermore an eyeball evaluation of the plotted fit with $c_\eta = 0$ shows it to be poor. A similar procedure at each of the other mass sweeps indicated changes in χ^2 of 12 to 50 when the value of c_η was changed from its value at χ^2 minimum to the value zero. During the fitting procedure, the polynomial background retained its smooth shape and did not show any bumps or wiggles. This also remained true in the case, subsequently discussed, when attempting fits including a step for the ω.

Variation in the missing mass squared position of the η step produced a narrow minimum in chi-squared at the true mass value of the eta. The width of the minimum corresponded to an uncertainty $\delta(m_\eta)^2 \simeq 0.02\ \text{GeV}^2$ while similar variation in the ρ step resulted in $\delta(m_\rho)^2 \simeq 0.03\ \text{GeV}^2$.

The η and ρ steps were more sharply effected by the assumed form of the background than was the π^o. Consequently, the "long" mass sweeps were fit with backgrounds that could include terms through the fifth order in Eq. (IV.11). In most cases the variation in chi-squared between alternative fits using terms through third, forth, and fifth order was small, and the fits using a polynomial up to forth order were adequate.

From these fits, the ratios of c_η/c_π and c_ρ/c_π were calculated and then multiplied by the π^o cross sections at that angle. To the statistical error for the η and ρ steps given by the fitting program, was combined an error to allow for variation in their magnitudes due to variations in background assumptions. That error was taken to be respectively the percentage difference between the η and ρ step size given from a fit using through cubic terms for the background and that found in the

fits with the background containing through forth order terms. Additionally, a 25% error should be attached to each of these cross sections to allow for ignorance of the detailed shape for the subtracted background in the region of η and ρ steps, for which regions the background was 70-85% of the total measured signal.

A plot of the η and ρ cross sections, $d\sigma/du$ vs s is given in Fig. 5.12 with numerical values for the cross sections and their errors listed in Table 5.2.

The so-called ρ step was in reality a possible mixture of ω and true ρ^0 production, the two steps being nonseparable in this experiment due to an instrument resolution of some 75 MeV at the ω mass. Therefore, an attempt was made to determine the amount of possible ω by including in addition to the previously adjustable parameters, i.e., those for the background and the π^0 and η steps, an ω step centered at the ω mass and of the same width as used for the π^0 and η steps.

At 6 and 8 GeV the fits with only ω and no ρ^0 or only ρ^0 and no ω produced equivalently good χ^2 values. As a typical numerical example, we give the χ^2 values obtained for the case of 8 GeV, 1.9°. For ρ^0 included but no ω we found $\chi^2 = 43.9$, for ω included but no ρ^0 we found $\chi^2 = 43.4$, and for ρ^0 and ω both included, (giving of course one less degree of freedom) we found $\chi^2 = 41.6$. Thus in this example, we conclude that because of the experimental resolution we cannot resolve the ρ step into true ρ^0 and ω components.

At 12 and 18 GeV again we do not find it possible to make a clear choice between ρ^0 and ω components in the ρ step although the data tends to mildly favor more ρ^0 than ω.

We shall subsequently refer to this step as the "ρ" step but will understand that it is to be interpreted as the sum of ρ^0 and ω contributions.

REFERENCES FOR CHAPTER IV

1. V. Barger, CERN Report No. 68-7, I, 51 (1968).

2. B. Gittelman and Experimental Group C (private communication).

3. A. M. Boyarski, F. Bulos, W. Busza, R. Diebold, S. D. Ecklund, G. E. Fischer, J. R. Rees, and B. Richter, Phys. Rev. Letters 20, 300 (1968).

4. J. Orear, Notes on Statistics for Physicists, UCRL No. 8417, August 1958.

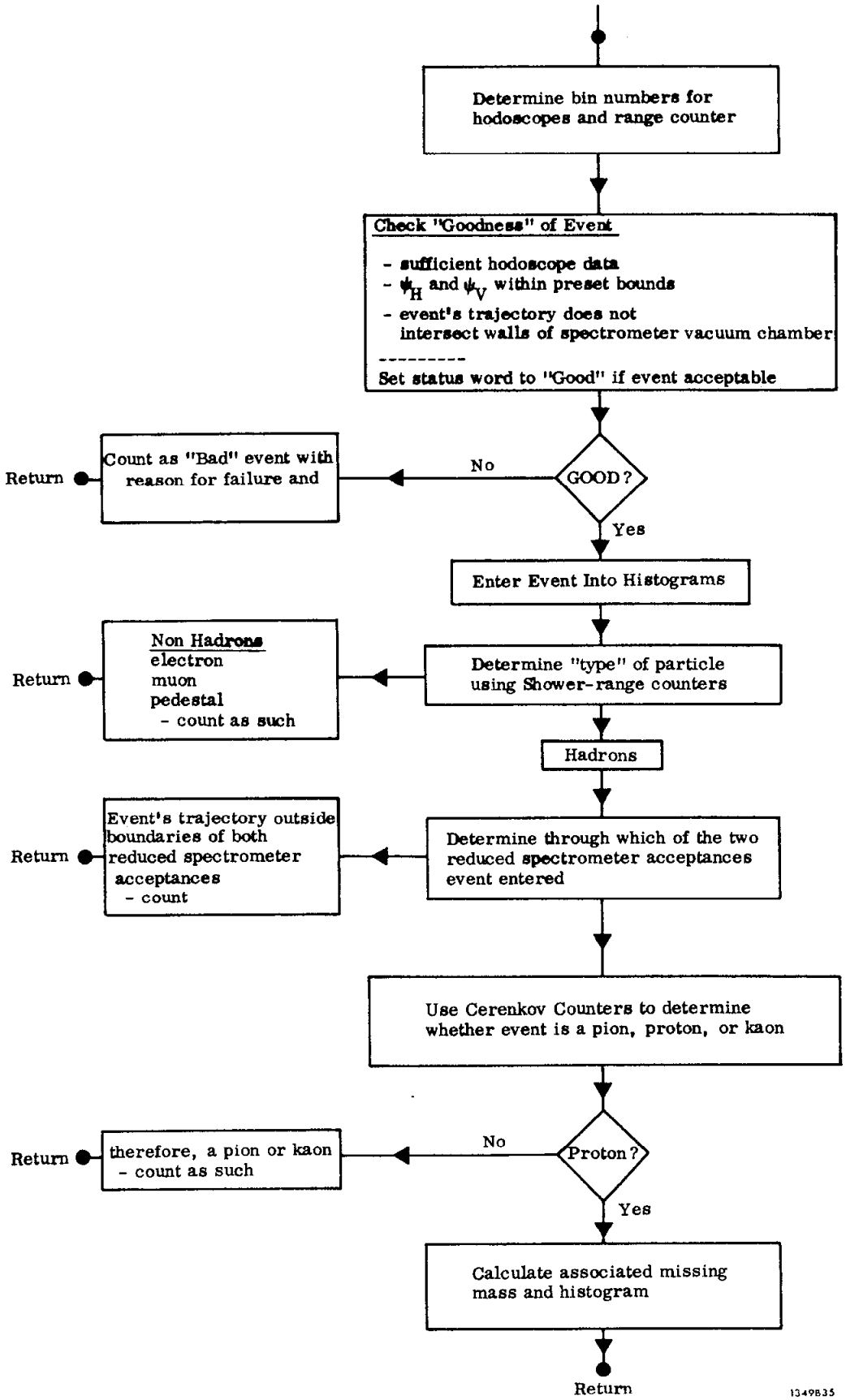

Fig. 4.1--Logic flow chart for "Off-Line" computer analysis which indicates procedure for reducing the raw data associated with each detected event and deciding on the final disposition of that event.

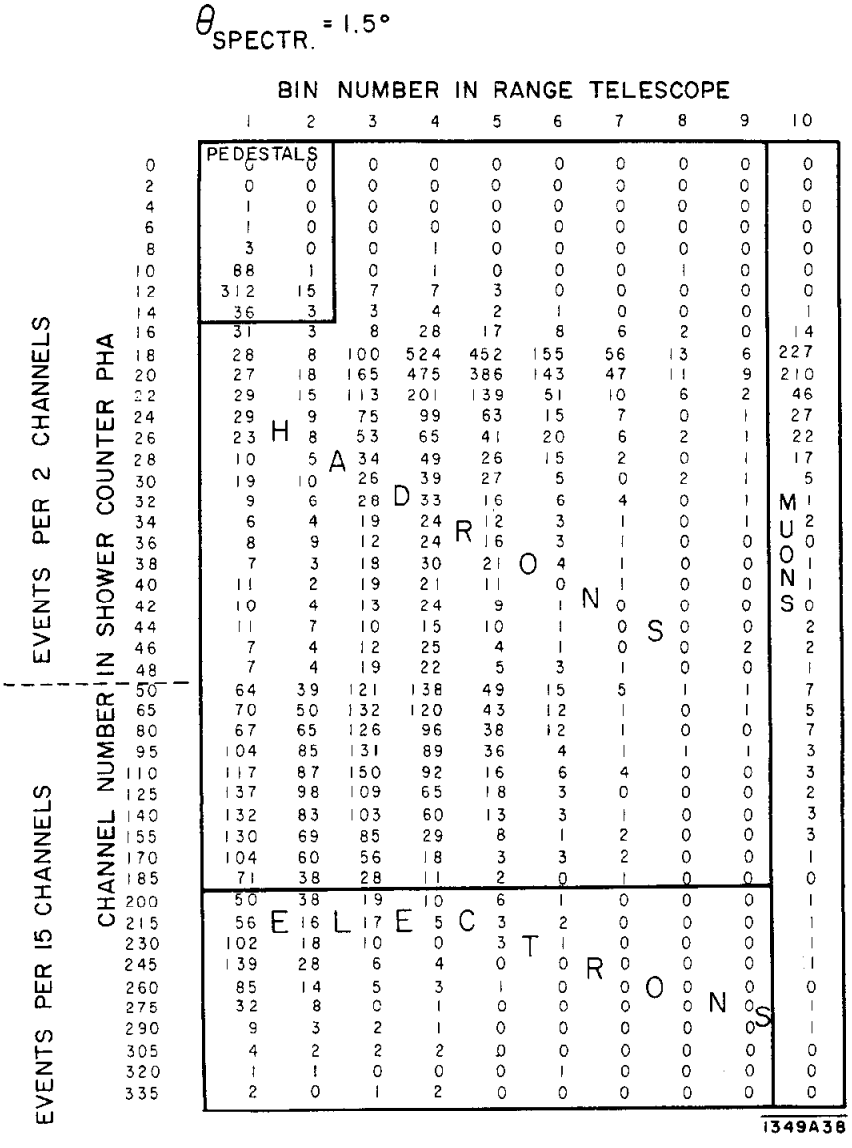

Fig. 4.2a--Shower-range histogram sectioned off with boundaries dictated by computer analysis programs. Spectrometer angle is 1.5°. At this angle there are many electrons, which give shower counter signals in the channels beyond 200 and range telescope signals in the first bin. Compare with Fig. 4.2b and Fig. B.1.

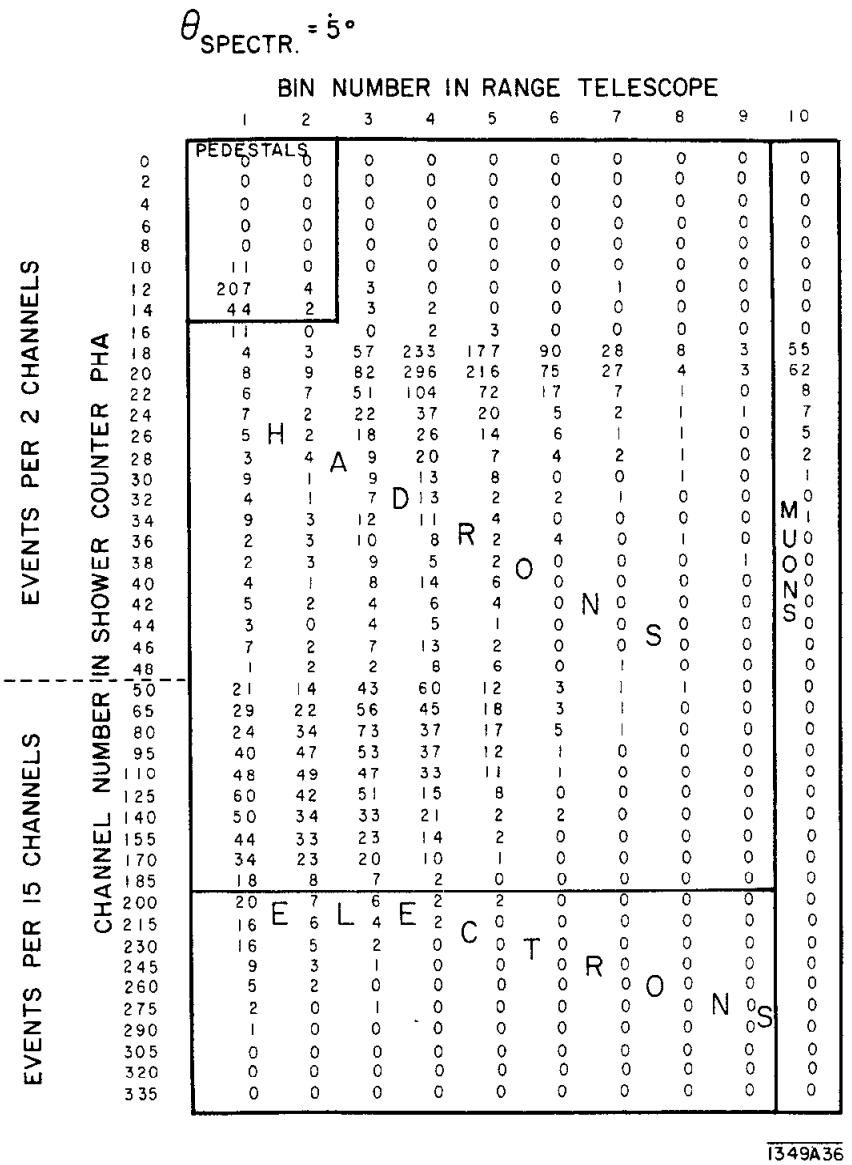

Fig. 4.2b--Shower-range histogram sectioned off with boundaries dictated by computer analysis programs. Spectrometer angle is 5.0°. At this angle there are few electrons, which give shower counter signals in the channels beyond 200 and range telescope signals in the first bin. Compare with Fig. 4.2a and Fig. B.1.

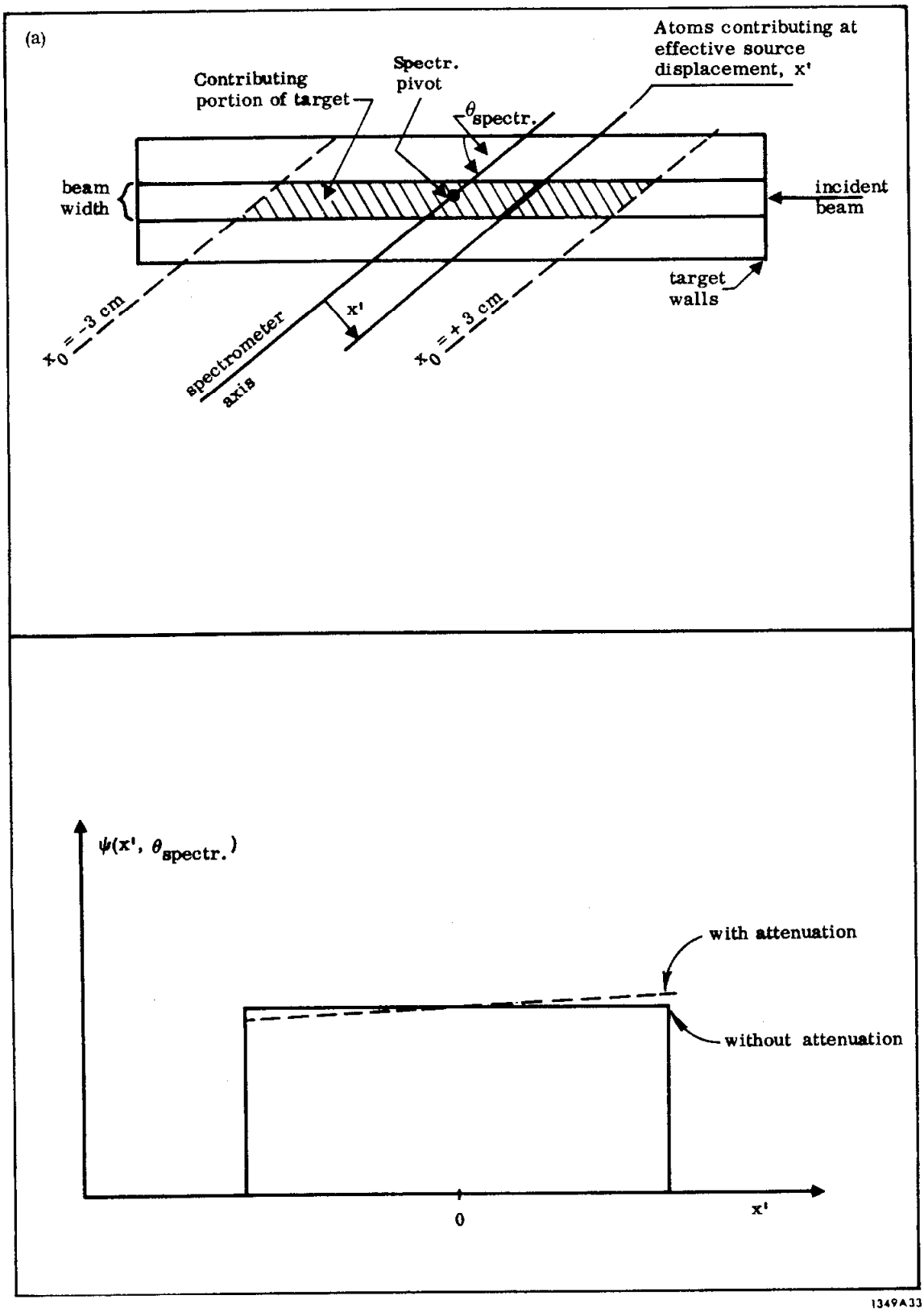

Fig. 4.3--(a) Schematic of spectrometer acceptance relative to hydrogen target for $\theta_{spectr} > 1.5^{o}$. (b) Schematic of source strength function, ψ, for geometry shown in Part (a).

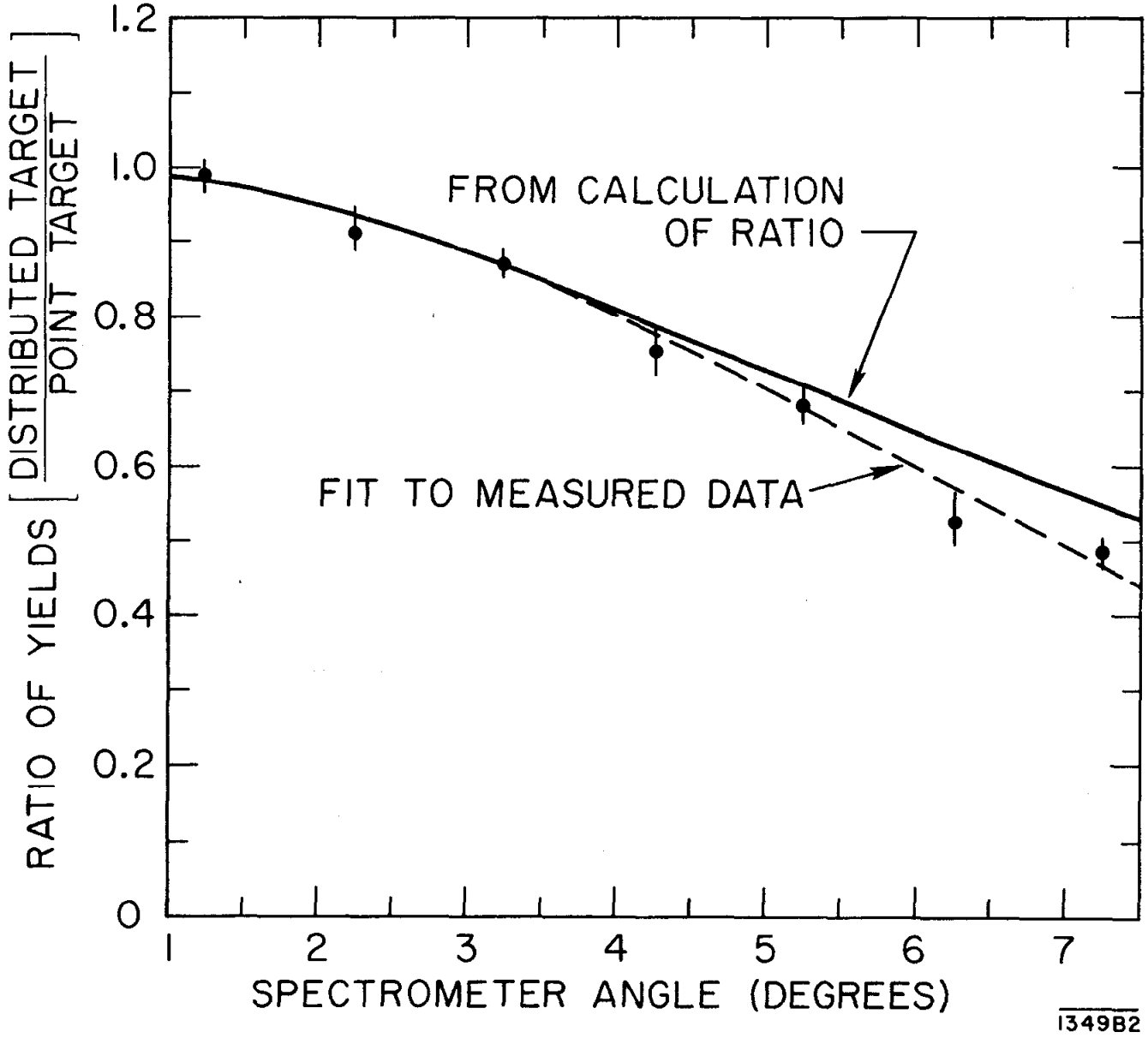

Fig. 4.4--Comparison of yield ratio for "distributed" and "point" aluminum targets. Solid curve represents calculated ratio from Eq. (IV.7). Dashed curve represents measured ratio.

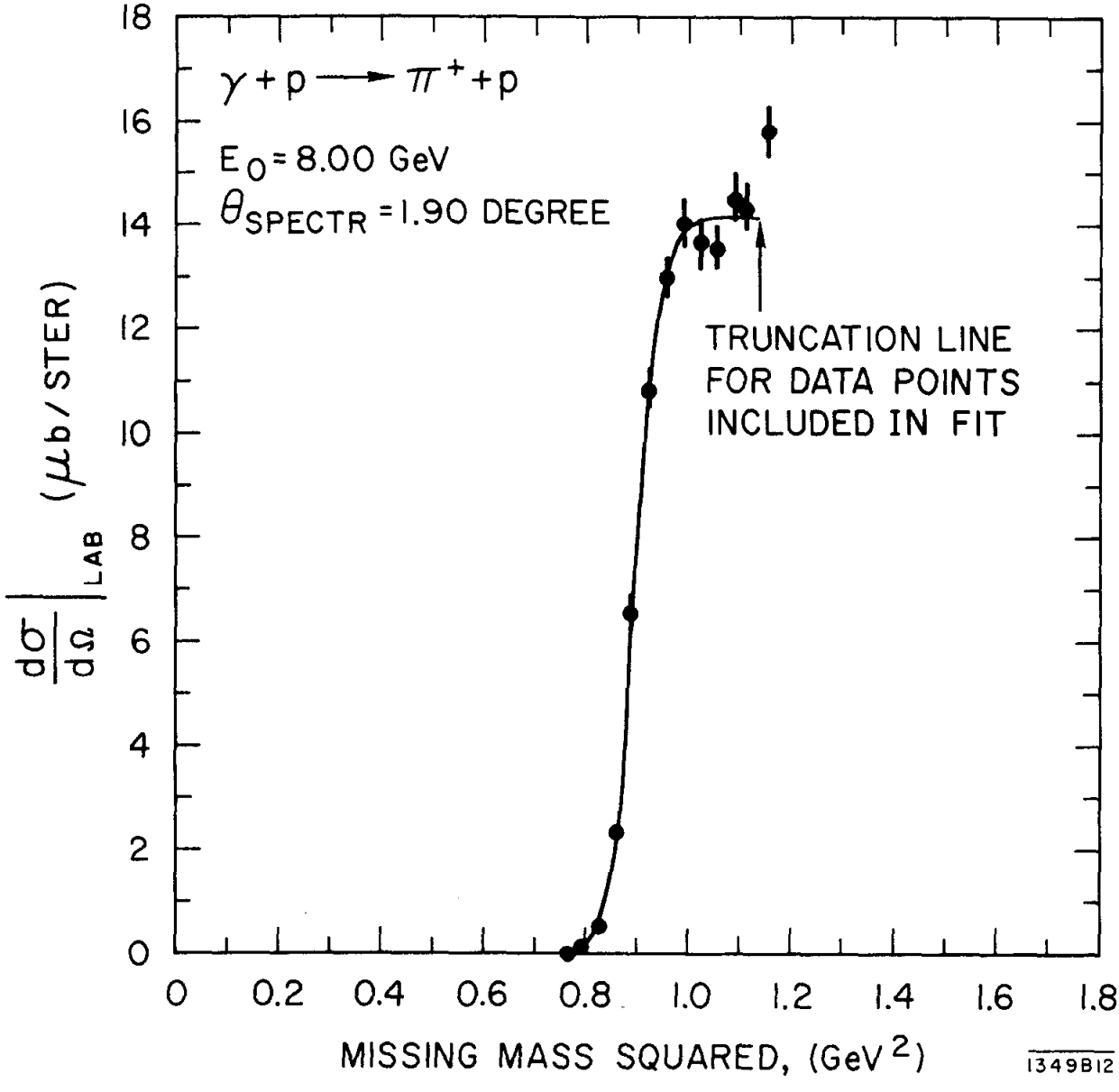

Fig. 4.5--Fit to a representative missing mass spectrum measured with one setting of spectrometer for reaction $\gamma p \longrightarrow \pi^+ n$.

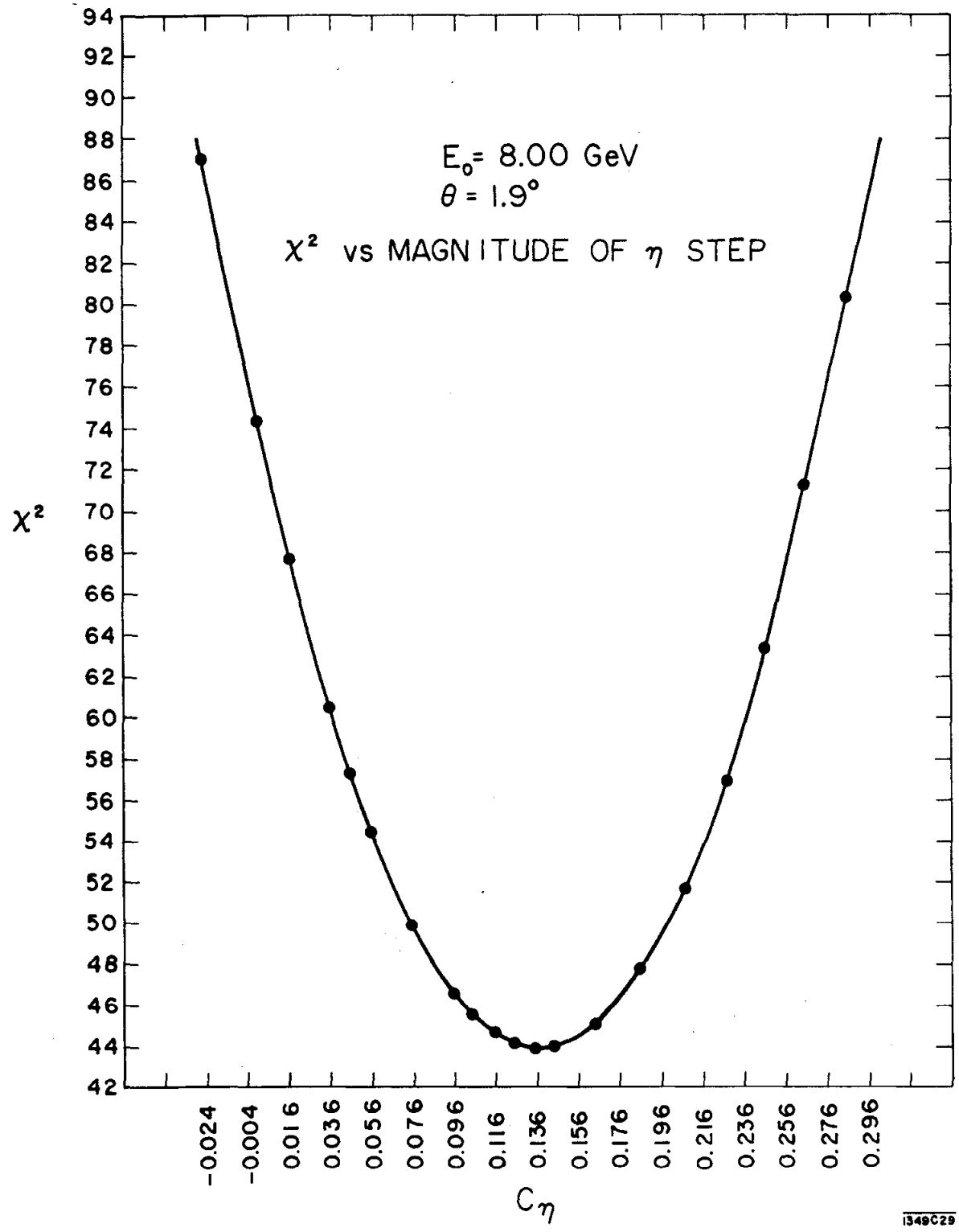

Fig. 4.6-- χ^2 vs magnitude of η step (c_η) for 8 GeV, 1.9° mass sweep. Fits adjusted parameters for fourth order polynomial background plus steps for the π^0 and ρ.

CHAPTER V

RESULTS AND DISCUSSION

Forward π^+ Data

The cross sections for the forward π^+ photoproduction measured in this experiment are shown in Fig. 5.1 together with those obtained by A. Boyarski et al.,[1] (at SLAC) in a separate but similar experiment intended to measure those cross sections.

Fits to the data from this experiment at 6, 8, 12 and 18 GeV for the range of t, $-0.07 \geq t \geq -0.7$ $(GeV/c)^2$ are depicted by the solid curves in Fig. 5.1 assuming the cross section can be represented by the expression $d\sigma/dt = A \exp(Bt)$. The table contained in that figure gives the best values for the coefficients A and B for the specified range of t, as found from the data of both experiments. The data fits reflect agreement in overall normalization between the two experiments to well within the 10% level.

Backward π^o Data

The measured differential cross section $d\sigma/du$ for backward photoproduction of π^o is plotted vs u in Fig. 5.2 and vs s for three values of u in Fig. 5.3. Table 5.1 gives numerical values for these cross sections together with their errors. Features in the data to be noted are:

(a) There is a backward peak, with a shape roughly independent of beam energy in the range 6-18 GeV. It is interesting to observe that the free hand curves passed through the data in Fig. 5.2 are identical in shape; i.e., the same curve was traced through the data point at each energy, and results in a reasonable representation of the measurements.

(b) Strikingly, the sharp dip structure seen in the backward elastic scattering of π^+ mesons from protons[2] at $u = -0.15$ $(GeV/c)^2$ does not appear in these photoproduction measurements.

(c) In the range $-0.4 \leq u \leq 0 (GeV/c)^2$, the cross section falls most rapidly, with a change of slope occurring at approximately -0.4 $(GeV/c)^2$ and thereafter falls with a more gentle decrease.

(d) For positive values of u the cross section appears to decrease from the peak value. Cross sections were not measured with the spectrometer set at exactly zero degrees which represents the maximum positive value of u. However, at 6 GeV, the cross section was measured at $u = +0.06$ $(GeV/c)^2$ as compared to $u = +0.064$ $(GeV/c)^2$ for emission of the π^0 at exactly 180 degrees.

(e) Near $u = 0$, the cross section decreases with center-of-mass energy as $s^{-3.2 \pm 0.13}$.

(f) The integral of the cross section for $u > -1.0$ $(GeV/c)^2$ can be well approximated by $10^4 s^{-3}$ nanobarns with s in GeV^2. Thus for example, at 12 GeV the total backward cross section amounts to some 0.78 nanobarns as compared to a total photoproduction cross section of some 120 ubarns at this energy.

(g) There appears to be no indication of shrinkage. Representing the differential cross section by $d\sigma/du = A(u)\, s^{-B(u)}$, then fits to the data give values for B of 3.2 ± 0.13, 2.9 ± 0.16, and 3.1 ± 0.25 for u values of 0.0, -0.2 and -0.5 $(GeV/c)^2$ respectively. (See Fig. 5.3)

Discussion of π^0 Data

A major objective of this experiment was to obtain values for cross sections for one of the two photoproduction reactions listed in Chapter I in order that a comparison could be made between photo-induced and meson-induced processes in the backward direction. It was of particular interest to see if the Regge pole

analysis which so well explained the features found in the backward elastic πp scattering data would also explain the backward photoproduction data if in the analysis of the photoproduction data the baryon Regge trajectories were taken to have the same form and relative importance as in backward πp scattering. The possibility that such an approach would prove successful was considered reasonable as both sets of reactions, i.e., the backward pion scattering and the backward photoproduction, have in common the point that they are presumably produced by exchange of baryons in the crossed channel with isotopic spin values of 1/2 and 3/2 only.

The backward π^+ photoproduction data resulting from the first measurement of reaction #5 (see Chapter I) out to u values of approximately -0.5 $(GeV/c)^2$ were measured and reduced prior to the reduction of the present data on reaction #4. The most striking feature of the π^+ data was the absence of the dip structure which had previously been seen in reaction #1. Using the pion scattering data (reactions #1 and #2) and the photoproduction data (reaction #5), E. Paschos[3] carried out a Regge analysis and determined that acceptable fits could be made simultaneously to the combined data from all three reactions on the basis of a pure Regge pole model including only the same two trajectories which gave a good fit to the πp data, namely the N_α and the Δ_δ. He found that to explain the photoproduction data either it must be assumed that there existed interference between the N_α and Δ trajectories and that both trajectories had substantial imaginary parts in α- or else that, in contrast to the πp case, the N_α trajectory was not dominant.

With completion of the measurements reported here and of additional measurements on the backward π^+ photoproduction, Fig. 5.4, it was noted once more that the marked dip effect seen in reaction #1, again did not appear in the π^o

photoproduction data, which further supported the suggestion that the nucleon trajectory, N_α, was not dominating the photoproduction reactions. An attempt by J. Beaupre and E. Paschos to fit all four of the reactions (1, 2, 4 and 5) using just the two trajectories N_α and Δ, but with complex form, now failed to produce reasonable fits. If the N_α trajectory were dominant in photoproduction, one would expect a dip near $u = -0.15$ $(GeV/c)^2$, as is seen in the backward $\pi^+ p$ data; but there is no such dip in either π^+ or π^0 backward photoproduction. And if the Δ_δ were dominant, and the N_α contribution indeed very small at the dip position, then from isospin symmetry the ratio of the cross sections at the dip,

$$r = \frac{\left.\frac{d\sigma}{du}\right|_{\gamma p \to p\pi^0}}{\left.\frac{d\sigma}{du}\right|_{\gamma p \to n\pi^+}} \qquad \text{(V.1)}$$

should be 2; but in fact it is $r = 0.8 \pm 0.2$.

The preceding remarks indicate why neither an N_α-dominant nor a Δ_δ-dominant solution, in the framework of a pure $N_\alpha + \Delta_\delta$ Regge pole exchange model, fits the photoproduction data. Beaupre and Paschos[4] have shown that no mixture of the two exchanges, even with complex trajectories, can fit the photoproduction data and still give the very deep sharp dip effect seen in reaction #1, the $\pi^+ p$ backward scattering. They conclude therefore that at least one additional trajectory must be present. Some information on the contributing trajectories should be obtainable from the s-dependence of the data, since that s-dependence should be approximately of the form

$$\frac{d\sigma}{du} \approx s^{2\alpha(u)-2} .$$

Unfortunately, this general form, together with the general nature of the dependence of α on u for known trajectories, would lead one to expect shrinkage effects, and yet the π^+ and π^0 photoproduction data seem to show no shrinkage. Nevertheless,

the fact that at the nominal dip position for the N_α, $u \approx -0.15$ $(GeV/c)^2$, the s-dependence for the photoproduction data is approximately s^{-3} suggests that the contributing trajectory or trajectories at that u value have $\alpha \approx -0.5$. This helps suggest that whatever trajectories are contributing at that point have $\alpha \approx -0.5$.

From the experimental value of the ratio, r (Eq. (5.1)) one concludes that an additional T = 1/2 exchange must be present, besides the N_α. With the suggested value of $\alpha \approx -0.5$ for this additional contribution, as just explained, one finds the best candidate is the $N_\gamma \left(\frac{3}{2}^-, 1520\right)$ trajectory (see Fig. 5.5).

A 3-pole fit, using the N_α, Δ_δ and N_γ trajectories, has been made by Beaupre and Paschos[4] (Fig. 5.6a). Independently, Barger and Weiler[5] have also made a fit, using the same trajectories (Fig. 5.7a). Both fits are reasonably satisfactory to both the π^+ and the π^0 photoproduction data. Rather different parametrizations are used, and the two groups arrive at rather different conclusions concerning the relative importance of the N_α contribution. It therefore seems that at present one can conclude that a 3-pole fit to reactions 1, 2, 4, and 5 can be found, but that there is considerable latitude in the parameter values which give a satisfactory fit.

One point remains to be discussed here. That concerns the question as to why the N_γ (or some similar trajectory) should not be required to explain reactions 1 and 2, and yet should be necessary to explain reactions 4 and 5. What is obviously involved here is the strength of the "upper vertex" in Fig. 1.1, the vertex connecting the exchanged baryon, the outgoing proton, and an incoming photon or pion respectively. The sizable contribution from N_γ, necessary to describe the photoproduction data, relative to the small (essentially negligible) contribution it is allowed to make in the pion scattering data (reactions #1 and #2) is not necessarily surprising. The data from low energy formation experiments indicate that the relative size of the second resonance, N(1520) — thought to be the first pole on the N_γ trajectory —

to the 1st resonance, N(1238), is larger by a factor of 2-5 in photo induced vs pion induced processes.

The turnover in $d\sigma/du$ at 180^{o}, is according to both references, Barger and Weiler and Beaupre and Paschos, a kinematic effect, coming from the fact that three of the four s-channel helicity amplitudes vanish at 180^{o} by angular momentum conservation.

Finally, we remark on a few additional points. First, there exists the possibility of right signature fixed poles contributing to the cross section in addition to the Regge exchanges. Dashen and Lee[6] have pointed out that the backward pion photoproduction cross section, $d\sigma/du$, can be written as the sum of two terms, the first arising from a right signature fixed pole and the second from the Regge exchanges. They argue this circumstance would provide a sensitive test for the existence of such poles as the term for the fixed nucleon pole at $J = 1/2$ would be proportional to s^{-1} and therefore, at high energies would dominate the cross section. The data from this experiment, Fig. 5.3, indicate an energy dependence of s^{-3} which should be clearly distinguishable from that of s^{-1}. Therefore, it is concluded that the present data lend no support for the existence of right signature fixed poles contributing in any major way to the processes measured here.

Next, we show the relationship between the low energy data from DESY[7] for reaction #4 $\left.\frac{d\sigma}{d\Omega}\right|_{cm}$ vs E and the data reported here, in Fig. 5.8. It should be noted that only every second point for the DESY data has been plotted. The normalization between the two experiments appears to be consistent.

Lastly, data for reaction #3, charge exchange scattering[8] (CEX) have recently become available in the range of 2 to 6 GeV/c incident pion momentum. This reaction is believed to be mediated by baryon exchange with allowed values for isospin of 1/2 and 3/2, and therefore it was natural to try and understand the

features of the data in terms of Regge exchange using the N_α and Δ trajectories. Barger and Cline[9] made two predictions as to the shape that data would have when measured. Their analysis used the N_α and Δ trajectories with parameters as determined from the high energy pion scattering data (reactions 1 and 2) and in addition used the two possible signs for the ratio of the Δ to nucleon residue functions; i.e., $\frac{\beta_\Delta}{\beta_\alpha} < 0$ or $\frac{\beta_\Delta}{\beta_\alpha} > 0$, with the solution using the negative value for this ratio being the preferred one.

Comparison of the preferred solution with the data[8b] is shown in Fig. 5.9. The non-preferred solution does not give a good representation of the data. The fit is tolerable, although not too good in the dip region. The sharp dip seen at $u = -0.15(GeV/c)^2$ in reaction #1 does not appear in the charge exchange data. Instead there appears to be a break in the distribution and perhaps a weak dip near u value of $-0.3\ (GeV/c)^2$.

η and ρ Cross Sections

Cross sections for the backward production of η and ρ mesons are plotted vs u in Figs. 5.10 and 5.11 and vs s in Fig. 5.12. Numerical values are given in Table 5.2. It is noted that the magnitude of each of these cross sections is comparable to that for π^o production — the η cross sections are about 1.5 to 2 times smaller than the π^o cross sections, and the ρ cross sections are about 1.5 to 2 times larger than the π^o. The quoted errors are large due to both the statistical quality of the data and the uncertainty in the subtraction of the background arising from multi-pion production (see Chapter IV).

The statistical quality of the data is less good than that in the π^o measurements. The data measurements were extended to the larger values in missing mass, in the region where the η and ρ steps are seen, in order both to measure indicative cross sections for those two reactions, and to provide data at high missing mass

values against which to match the multi-pion background; however, we took only limited data here, because we wished to maximize the running time devoted to the π^o measurements. However, the η and ρ results are included, since they represent the only known values for those cross sections in the 6-18 GeV energy range.

The reported cross section for the ρ is actually the sum of that for ρ^o and ω production, as indicated in Chapter IV. With the mass separation of some 20 MeV between those two mesons the instrumentation resolution ~75 MeV at the ω^o mass would not allow separation of the two processes.

Discussion of η Production

The η meson is an isosinglet and therefore requires T = 1/2 exchange in the cross channel. If N_α exchange dominates the reaction, then a dip in the cross section would be expected at u ~ -0.15 $(GeV/c)^2$. The measurements presented here, Table 5.2, were made at two values of u, -0.05 and -0.67 $(GeV/c)^2$, and thus do not sufficiently delineate the u dependence of that cross section to see if such a dip effect occurs.

Presently, it is thought, on theoretical grounds, that the ηNN coupling is small, less than 1/10th that for πNN.[10] Moreover, π^o emission can occur with Δ exchange as well as with T= 1/2 exchange. In view of these considerations and in view of the experimental fact that η production in the present data shows a $d\sigma/du$ which is 1/2 to 2/3 that for π^o production, the implication is that some T= 1/2 exchange other than N_α exchange might be contributing relatively strongly to η production. Moreover the s-dependence of η production at small u suggests $\alpha(0) \approx -0.7$, following the same argument given above in the discussion of π^o production.

These considerations all suggest that N_γ exchange, or some similar exchange, might be making a major contribution to η production. However, a fuller interpretation must await more detailed experimental data on η production. We remark,

finally, that the relative magnitude for such cross sections as backward η production and backward π^o production involves the unknown u-dependence of the respective residue functions.

Discussion of ρ Production

The cross sections for backward ρ photoproduction are approximately 1.5 to 2 times larger than those for backward π^o; see Tables 5.1 and 5.2. The energy dependence of the ρ data for, $d\sigma/du$, at $u \simeq -0.06$ $(GeV/c)^2$ was found to be $s^{-3.6\pm.4}$ as compared to that of $s^{-3.0\pm0.2}$ for π^o production. Since the π^o and the ρ^o are members of isospin triplets, production of both mesons may proceed via exchanges of the same trajectories, in which case differences in the structure of the meson-nucleon vertex might be inferred from the ratio of the cross sections for the two reactions.

If a sizable amount of ω is actually present in "ρ" step, we cannot extract information on the relative nucleon-meson vertex strength for π^o and ρ^o or ω.

We note that experimentally the ratio of cross sections for the backward pion-initiated reactions,[11] again at small u, $\frac{\sigma(\pi^- p \longrightarrow p\rho^-)}{\sigma(\pi^- p \longrightarrow p\pi^-)}$ is about 1.5, a number very similar to the experimental ratio for $\frac{\sigma(\gamma p \longrightarrow p''\rho'')}{\sigma(\gamma p \longrightarrow p\pi^o)}$. In the pion-initiated reactions mentioned, pure T = 3/2 exchange is involved. Thus the experimental ratio for the photo reactions would be explained if pure Δ exchange is involved and if the contribution from ω exchange is very small. We remark in this connection that Beaupre and Paschos[4] do in fact conclude that at small u the photoproduction may be dominated by Δ exchange.

REFERENCES FOR CHAPTER V

1. A. M. Boyarski, F. Bulos, W. Busza, R. Diebold, S. D. Ecklund, G. E. Fischer, J. R. Rees, and B. Richter, Phys. Rev. Letters 20, 300 (1968).
2. J. Orear, D. P. Owen, F.C. Peterson, A. L. Read, D. G. Ryan, D. H. White A. Ashmore, C. J. S. Damerell, W. R. Frisken, and R. Rubinstein, Phys. Rev. Letters 21, 389 (1968).
3. Emmanuel A. Paschos, Phys. Rev. Letters 21, 1855 (1968).
4. J. Beaupre and E. Paschos, "Regge analysis of π^0 and π^+ photoproduction at backward angles," Report No. SLAC-PUB-655, Stanford Linear Accelerator Center, Stanford University, Stanford, California (1969).
5. V. Barger and P. Weiler, Wisconsin Preprint (to be published in Phys. Letters) (1969).
6. Roger Dashen and S. Y. Lee, Phys. Rev. Letters 22, 366 (1969).
7. G. Buschhorn, P. Heide, U. Kötz, R. A. Lewis, P. Schmüser, and H. J. Skronn, Phys. Rev. Letters 20, 230 (1968).

8a. V. Kistiakowsky, R. K. Yamamoto, R. D. Klem, P. Marcato, I. A. Pless, I. Spirn, E. F. Anelli, C. N. De Marzo, A. Romano, D. G. Crabb, A. C. Meyers III, and J. R. O'Fallon, Phys. Rev. Letters 22, 618 (1969);

b. R. C. Chase, E. Coleman, H. W. J. Courant, E. Marquit, E. W. Petraske, H. Romer, and K. Ruddick, Phys. Rev. Letters 22, 1137 (1969).

9. V. Barger and D. Cline, Phenomenological Theories of High Energy Scattering (W. A. Benjamin, New York, to be published).
10. J. C. Botke, "Partial wave analysis of $\pi^- + p \rightarrow \eta + N$," University of California, Santa Barbara Preprint (1968);

S. R. Deans and J. W. Wooten, "Spin 2 exchange in the process $\pi^- + p \rightarrow \eta + N$ and the η nucleon coupling constant," University of Florida, Tampa, Florida Preprint (1968).

11. E. W. Anderson, E. J. Bleser, H. R. Blieden, G. B. Collins, D. Garelick, J. Menes, F. Turkot, D. Birnbaum, R. M. Edelstein, N. C. Hien, T. J. McMahon, J. Mucci, and J. Russ, Phys. Rev. Letters 22, 102 (1969).

12. V. Barger and D. Cline, Phys. Rev. 155, 1792 (1967).

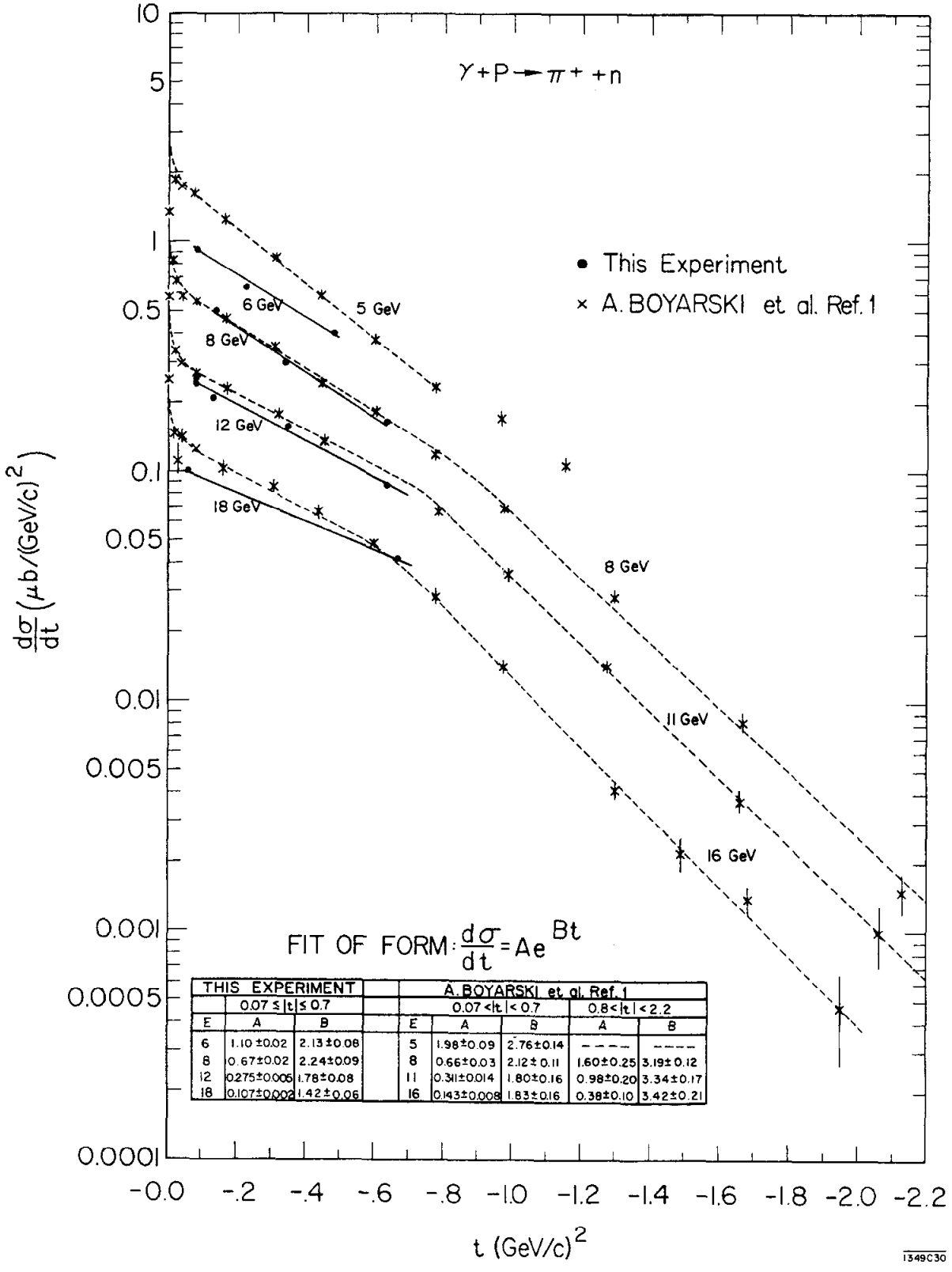

THIS EXPERIMENT			A. BOYARSKI et al. Ref. 1				
	0.07 ≤ |t| ≤ 0.7		0.07 < |t| < 0.7			0.8 < |t| < 2.2	
E	A	B	E	A	B	A	B
6	1.10 ±0.02	2.13 ±0.08	5	1.98±0.09	2.76±0.14	----	----
8	0.67±0.02	2.24±0.09	8	0.66±0.03	2.12± 0.11	1.60±0.25	3.19± 0.12
12	0.275±0.005	1.78±0.08	11	0.311±0.014	1.80±0.16	0.98±0.20	3.34±0.17
18	0.107±0.002	1.42±0.06	16	0.143±0.008	1.83±0.16	0.38±0.10	3.42±0.21

Fig. 5.1--Differential cross section $d\sigma/dt$, vs t, for the reaction $\gamma p \longrightarrow \pi^+ n$ as measured during this experiment ($+0.1 \geq -t \geq +0.8$) and by Boyarski et al.[1] ($0 > -t > 2.2$). Solid curves are fits to the data measured in this experiment while dashed curves are fits to data of Ref. 1. Fits were made in the form $d\sigma/dt = A \exp(Bt)$ with values for parameters A and B as shown.

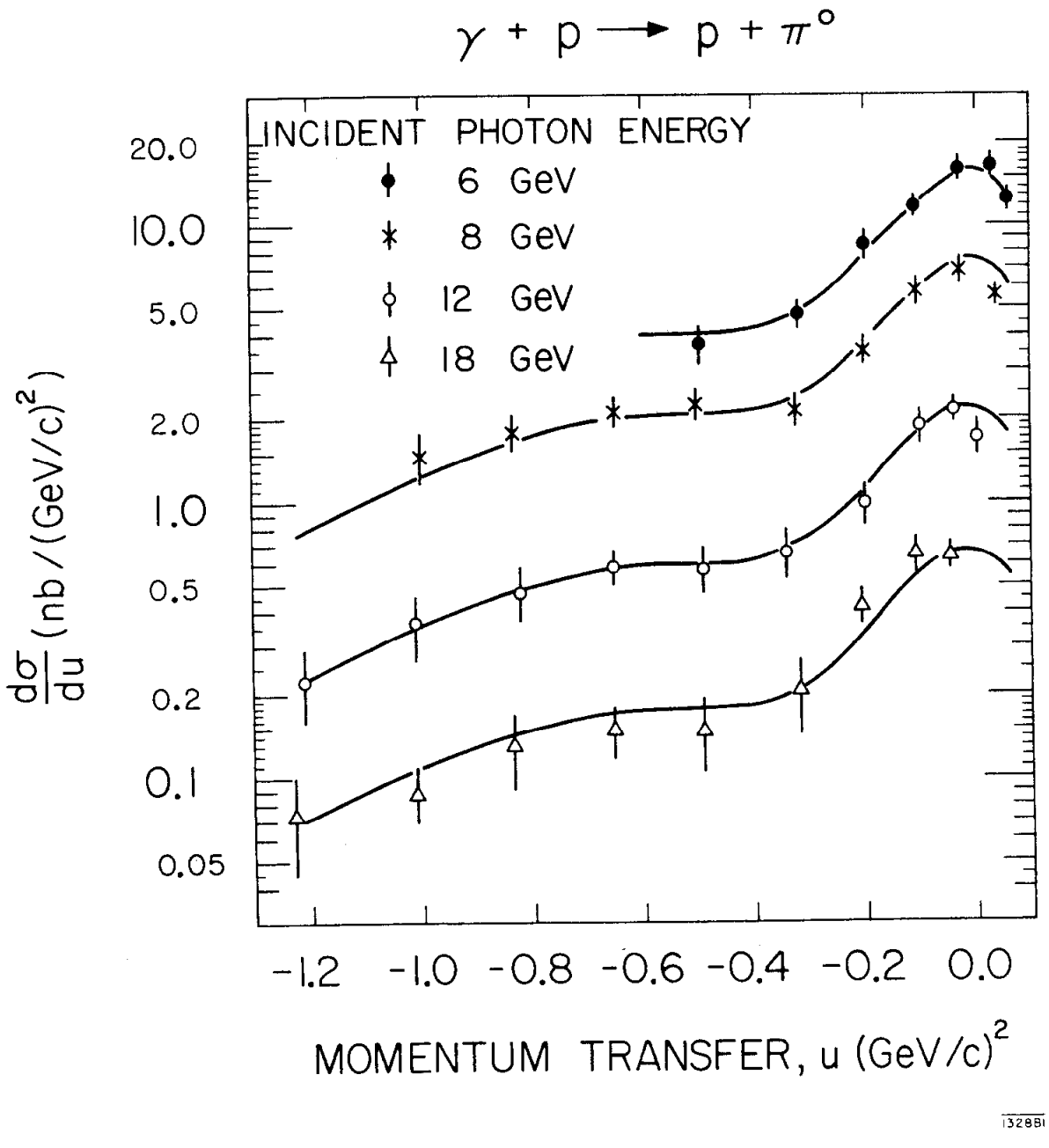

Fig. 5.2--Differential cross sections, $d\sigma/dt$, vs u for reaction $\gamma p \longrightarrow p\pi^{o}$. The solid curves represent a free-hand smooth curve through the data, with the same curve shape traced through the data points at each energy.

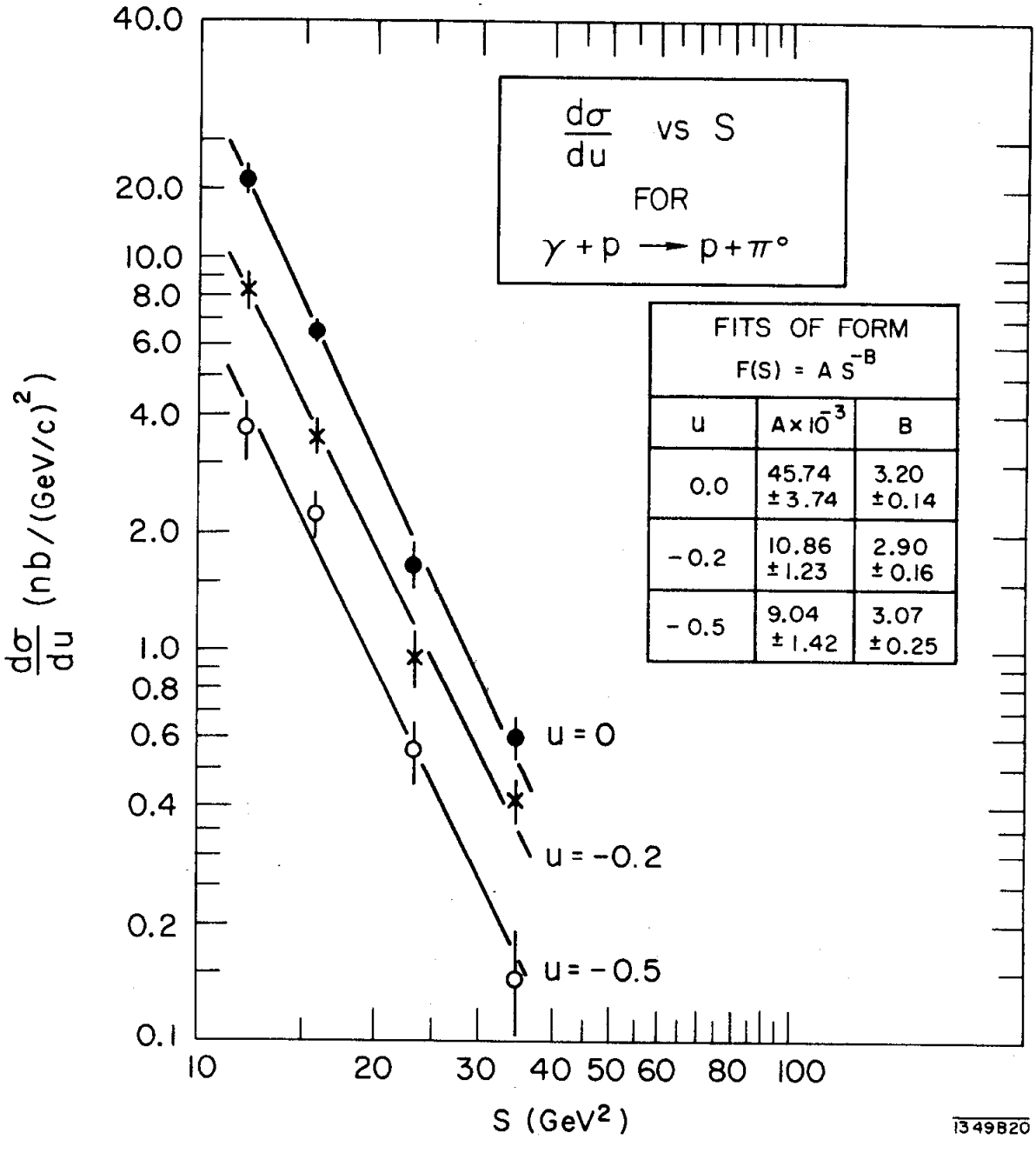

Fig. 5.3--Differential cross section, $d\sigma/du$ vs s at three u values for the reaction $\gamma p \longrightarrow p\pi^o$. Solid curves represent fits to the data of the form, $F(s) = A(s)^{-B}$, with the values for parameters A and B as shown.

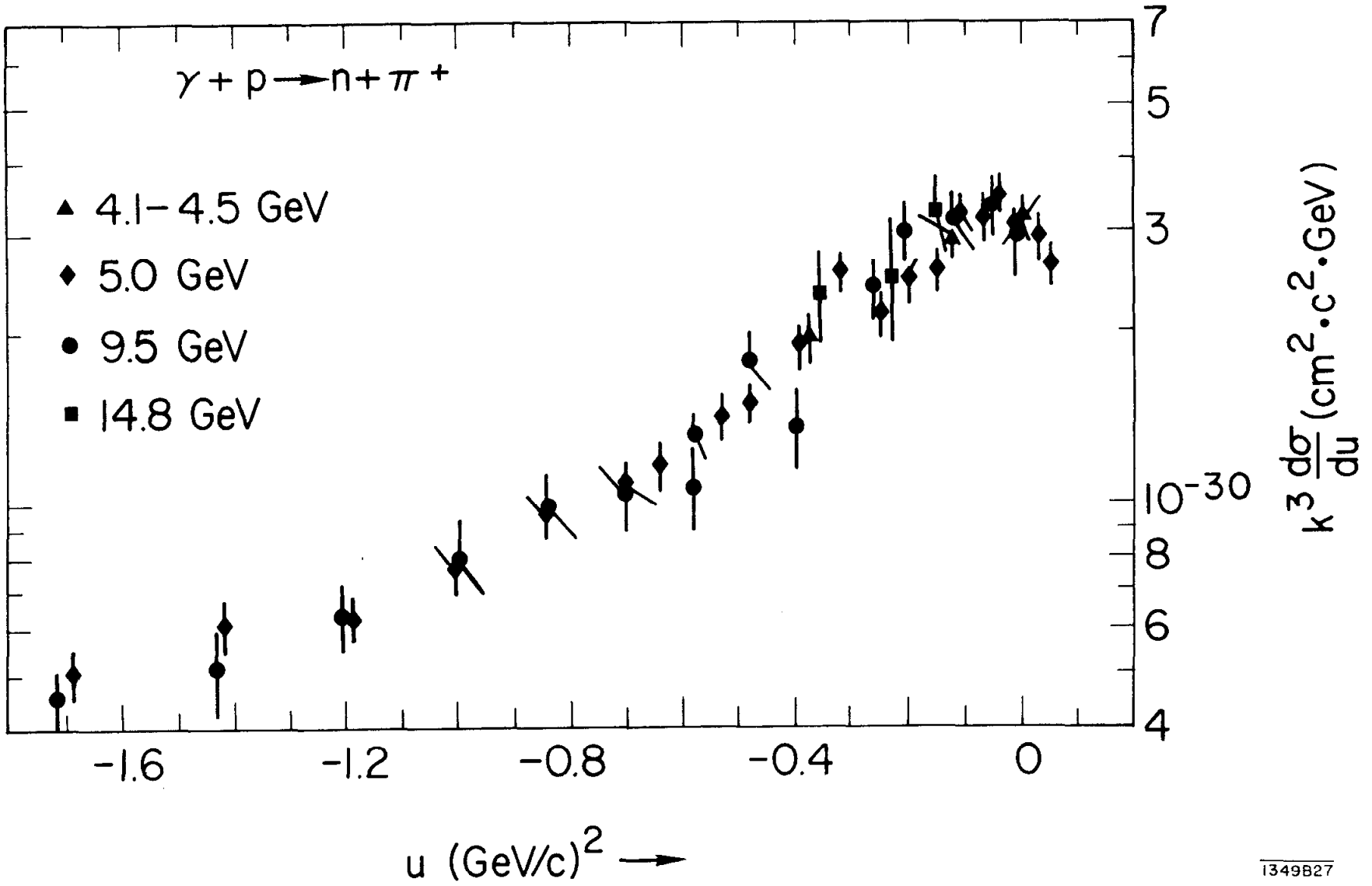

Fig. 5.4--Scaled differential cross section, $K^3(d\sigma/dt)$ vs u of Ref. 17, Chapter I for $\gamma p \rightarrow n\pi^+$. Scaled data have been plotted to remove the variation in K from one u value to the next.

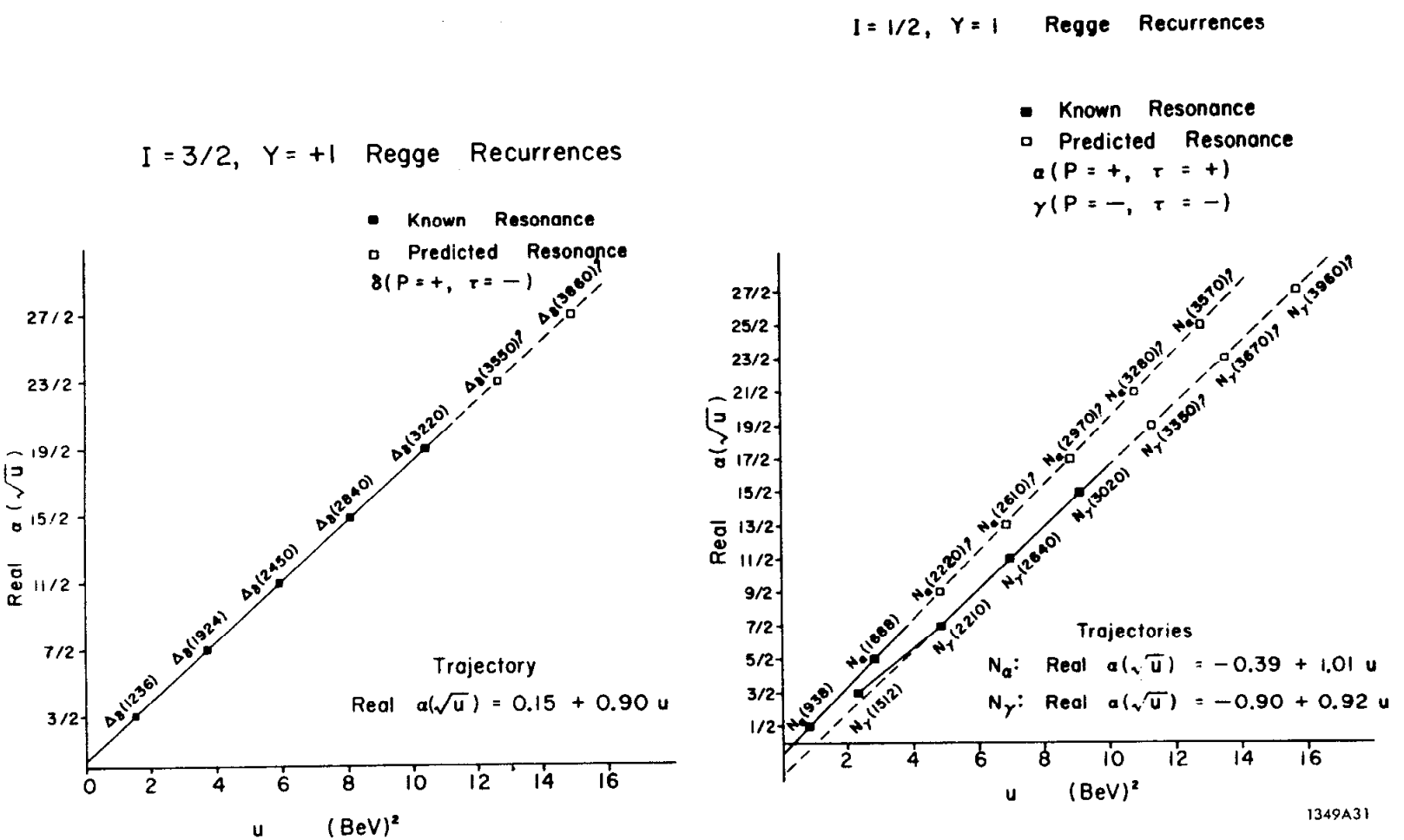

Fig. 5.5--N_α, N_γ, and Δ_δ Regge recurrences (Ref 12).

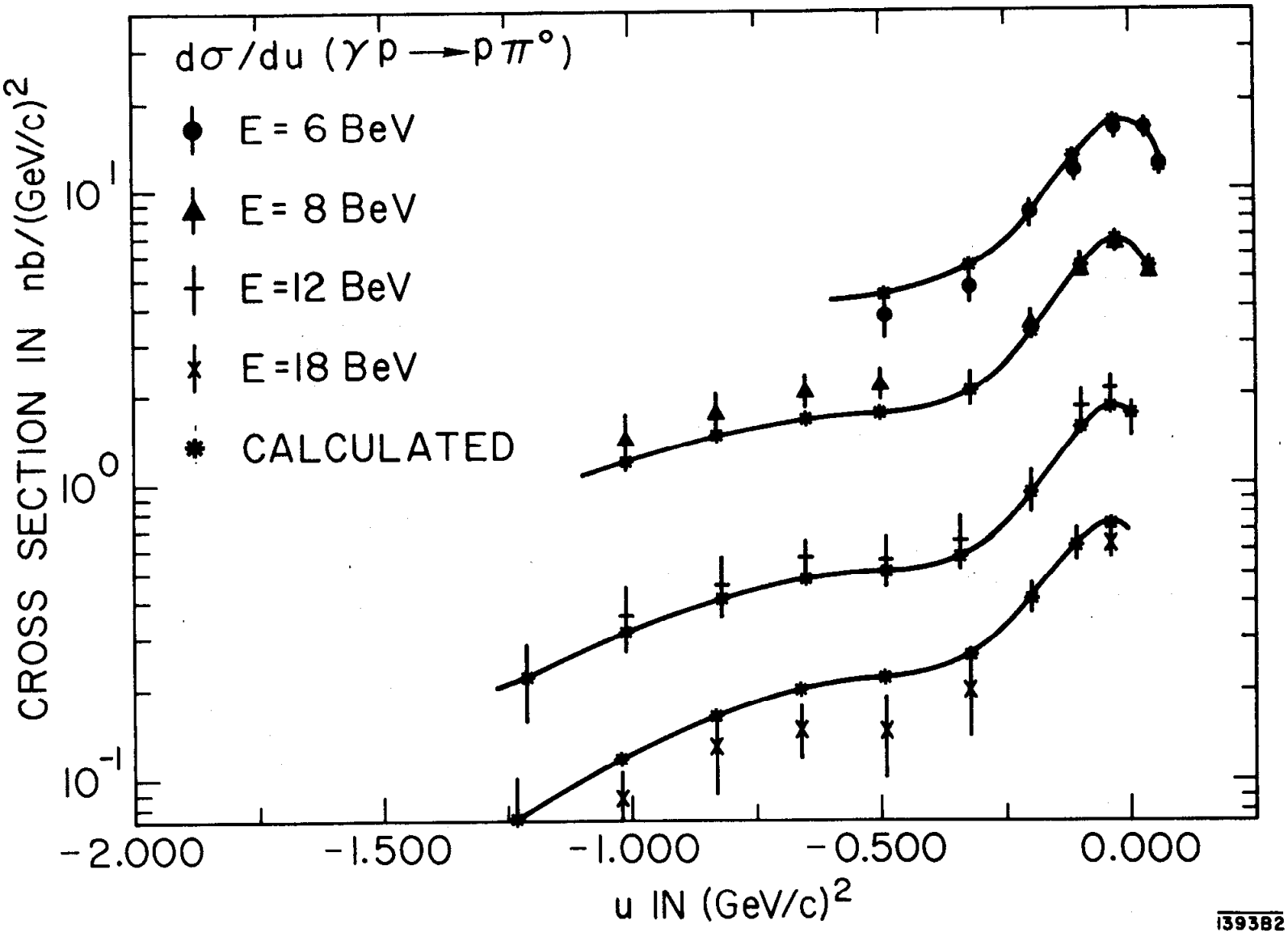

Fig. 5.6a--Fits of Beaupre and Paschos[4] using a Regge model to the differential cross section, $d\sigma/du$ for the reaction $\gamma p \longrightarrow p\pi^0$.

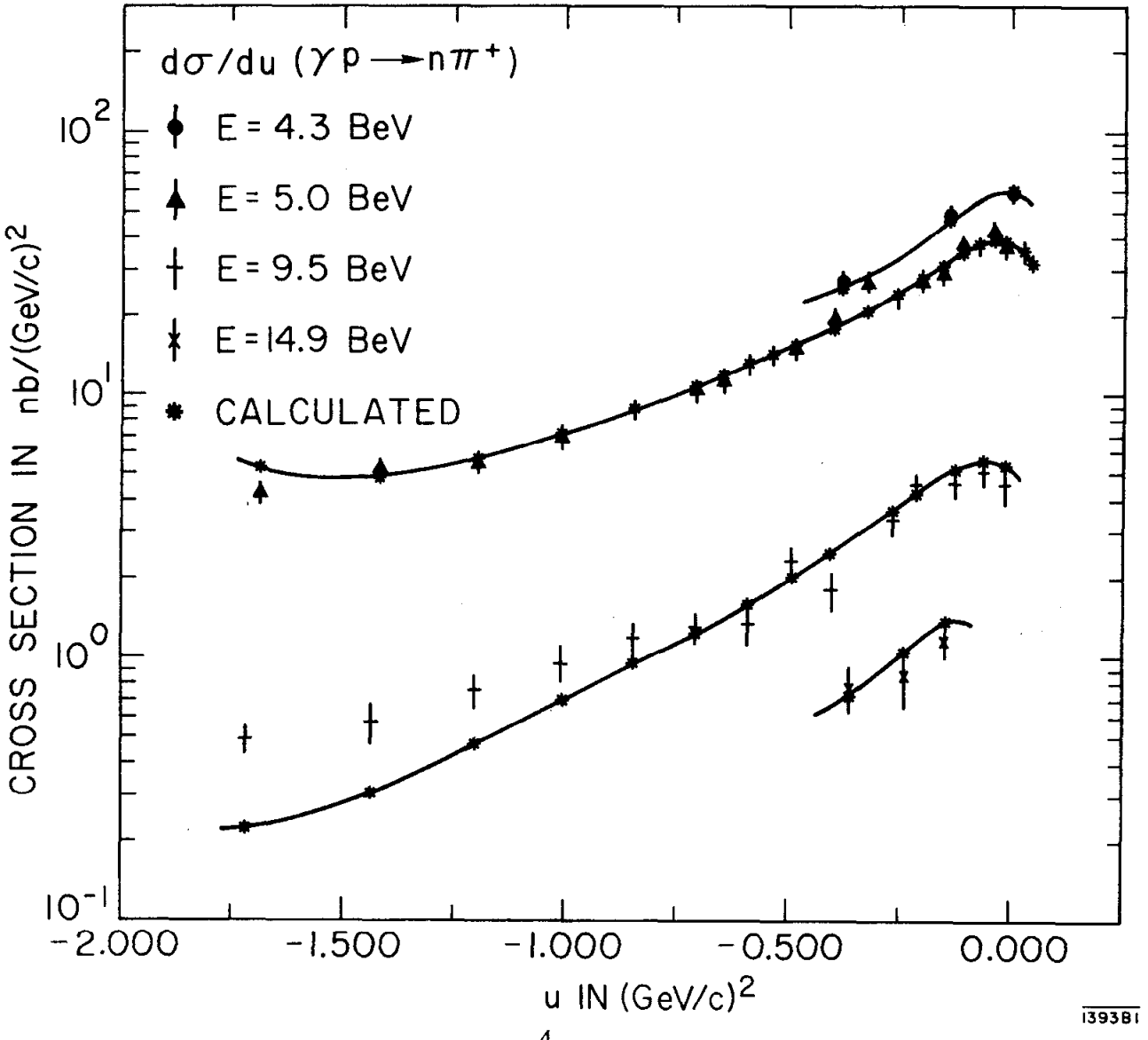

Fig. 5.6b--Fits of Beaupre and Paschos[4] using a Regge model to the differential cross section, dσ/du, for the reaction γp → nπ⁺.

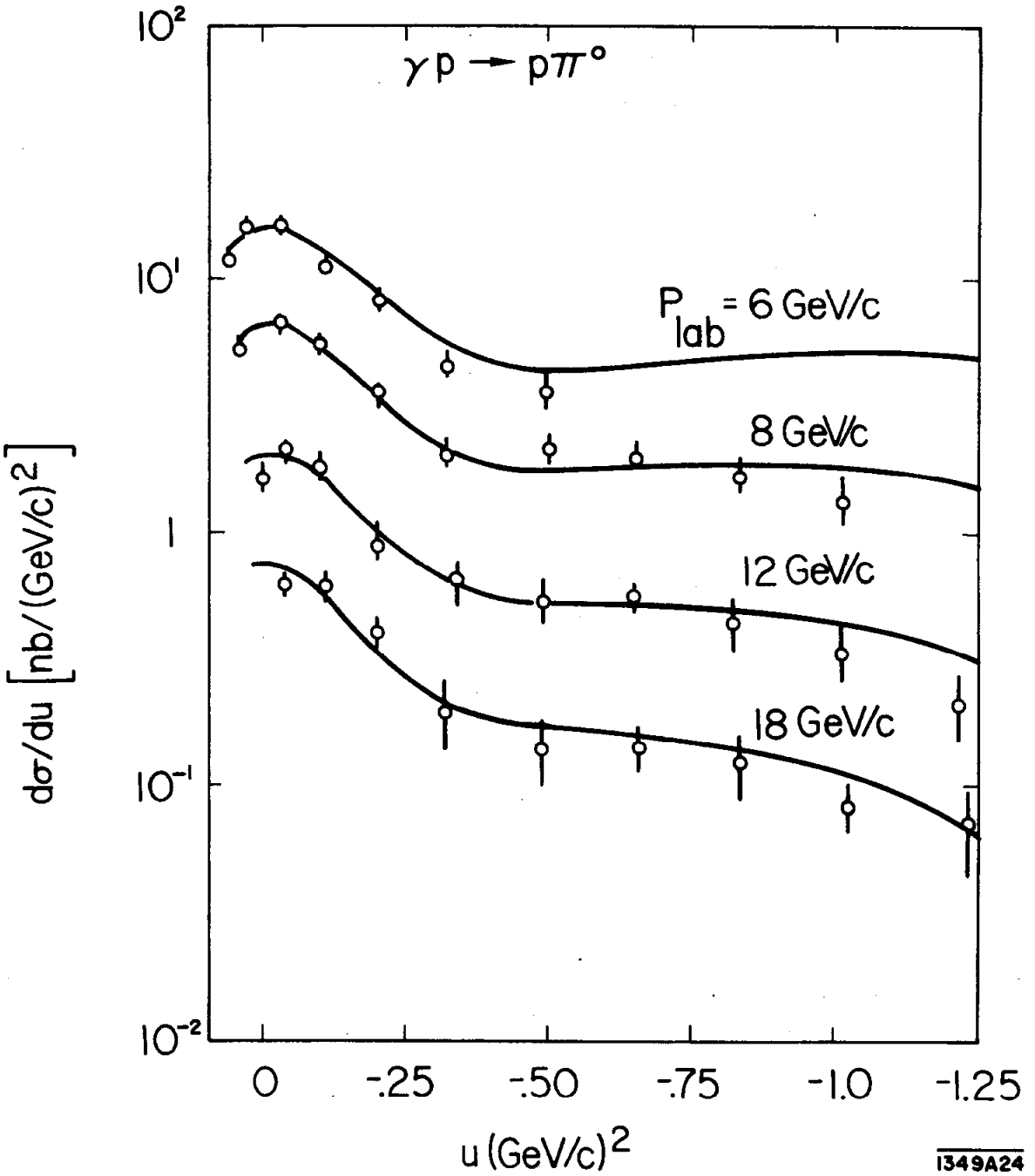

Fig. 7a--Fits of Barger and Weiler[5] using a Regge model to the differential cross section, $d\sigma/du$, for the reaction $\gamma p \rightarrow p\pi^0$.

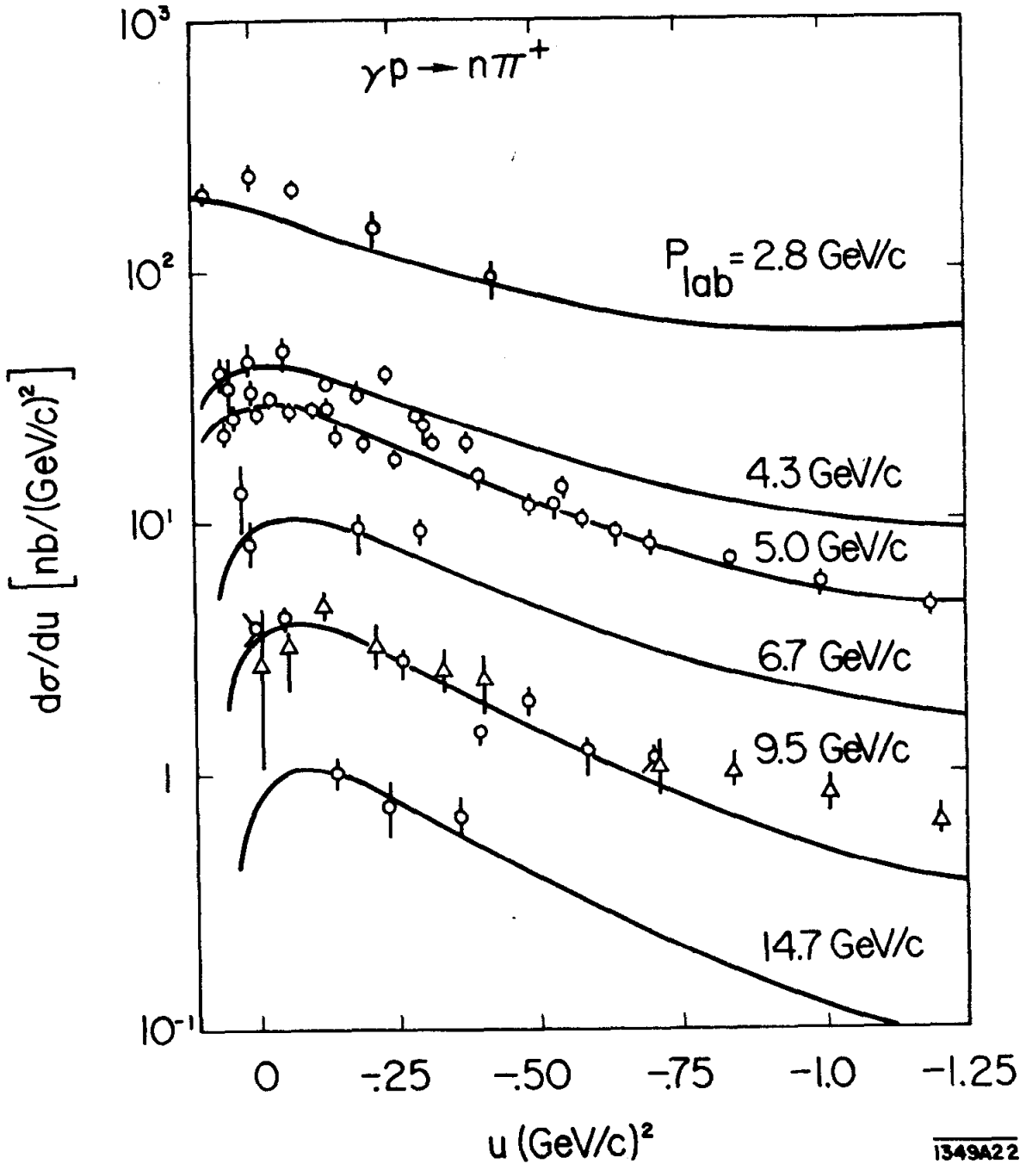

Fig. 7b--Fits of Barger and Weiler[5] using a Regge model to the differential cross section, $d\sigma/du$, for the reaction $\gamma p \rightarrow n\pi^+$.

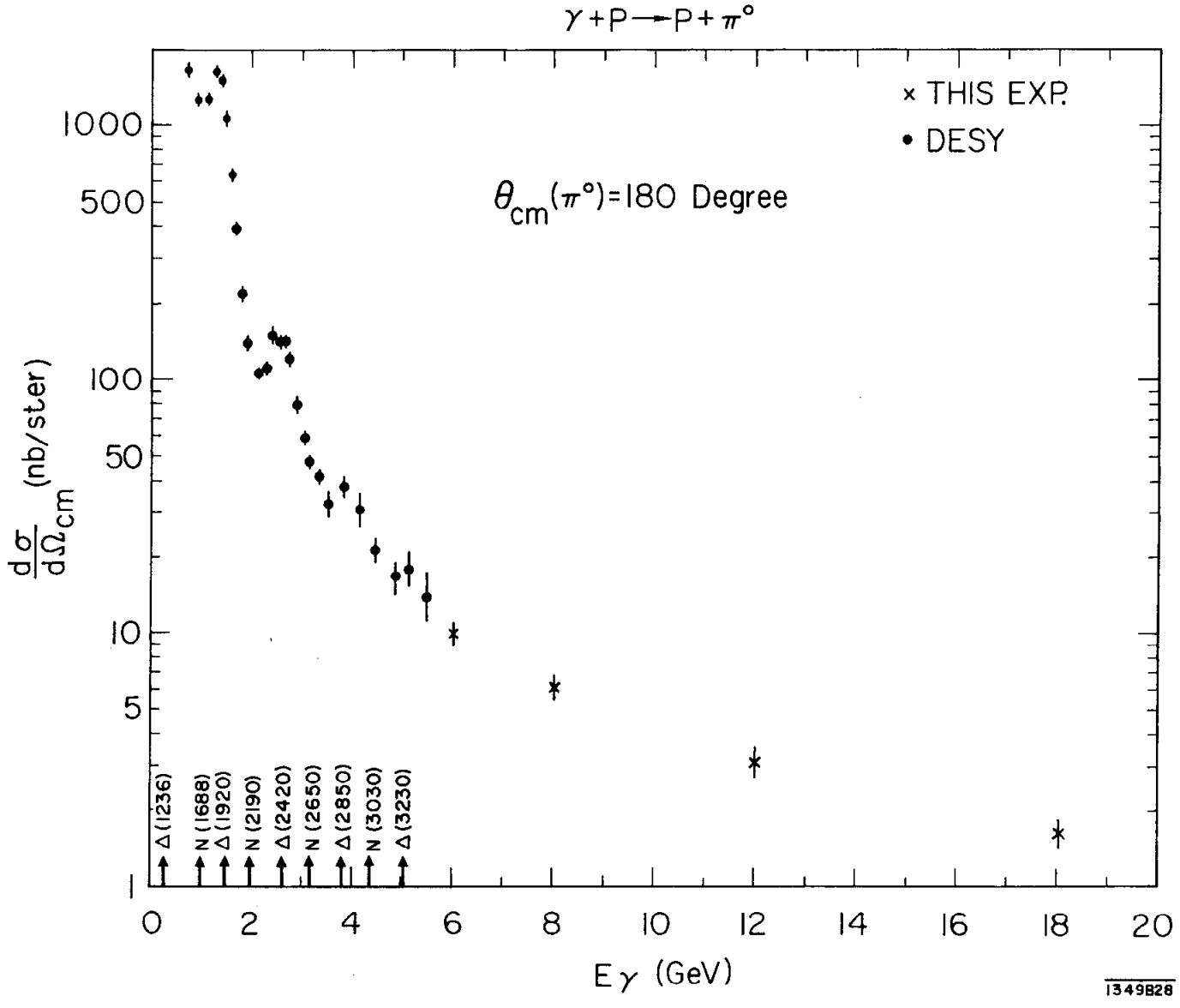

Fig. 5.8--Differential cross section $d\sigma/d\Omega|_{cm}$ vs s for the reaction $\gamma p \longrightarrow p\pi^0$ at 180^0 cm. The data points below 5.5 GeV are taken from the experiment of Buschhorn et al.[7] (DESY); every second point has been plotted. The points above 5.5 GeV result from this experiment.

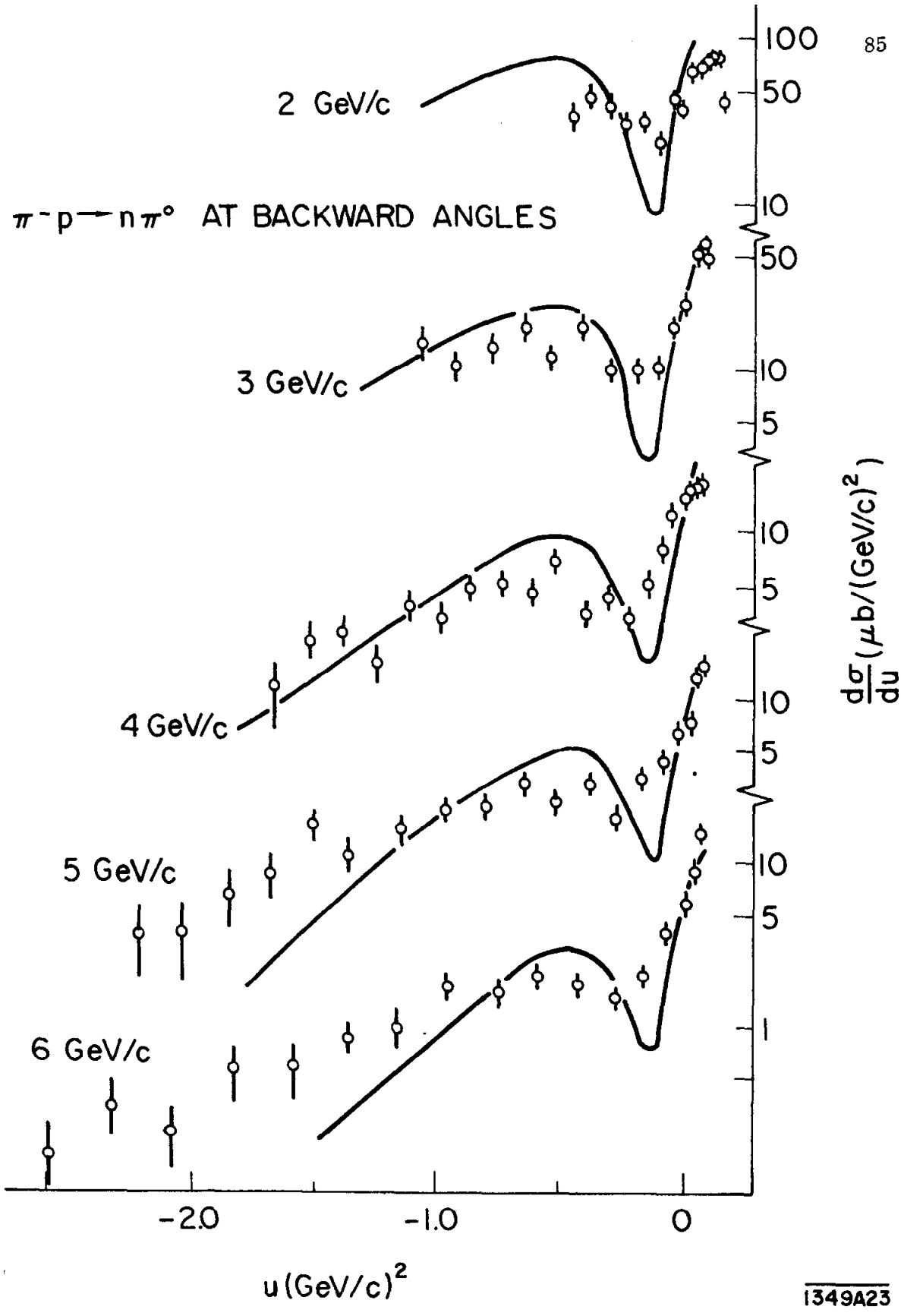

Fig. 5.9--Differential cross sections, $d\sigma/du$ vs u for the charge exchange reaction $\pi^- p \rightarrow n\pi^\circ$ (Ruddick et al., Ref. 8). The solid curves are the predictions of Barger and Cline[9] based on a Regge model with exchange of N_α and Δ_δ trajectories and the sign for the ratio of residue functions, $\beta_\Delta/\beta_\alpha$, taken as negative.

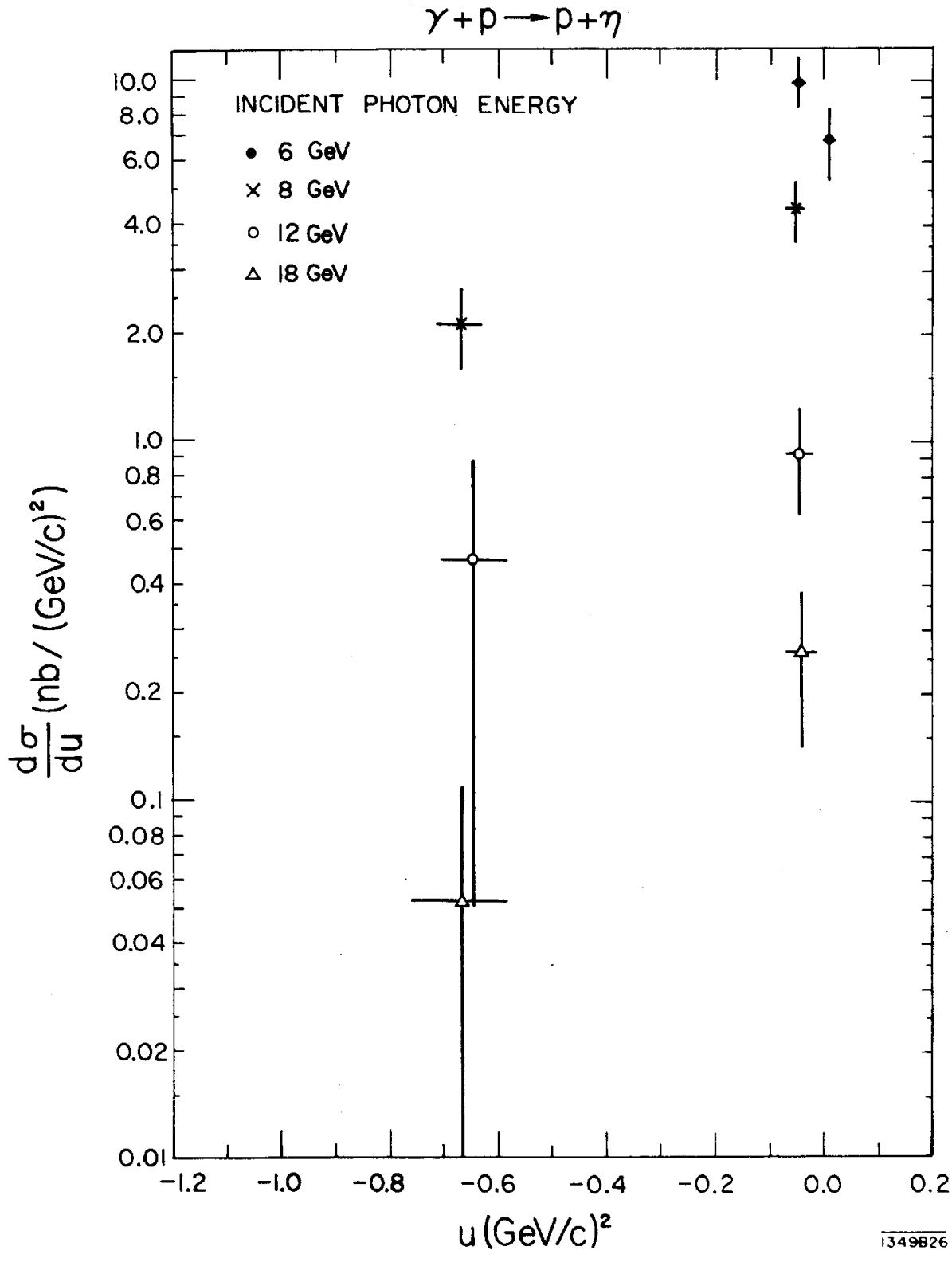

Fig. 5.10--Differential cross section $d\sigma/du$ vs u for the reaction $\gamma p \longrightarrow p\eta$.

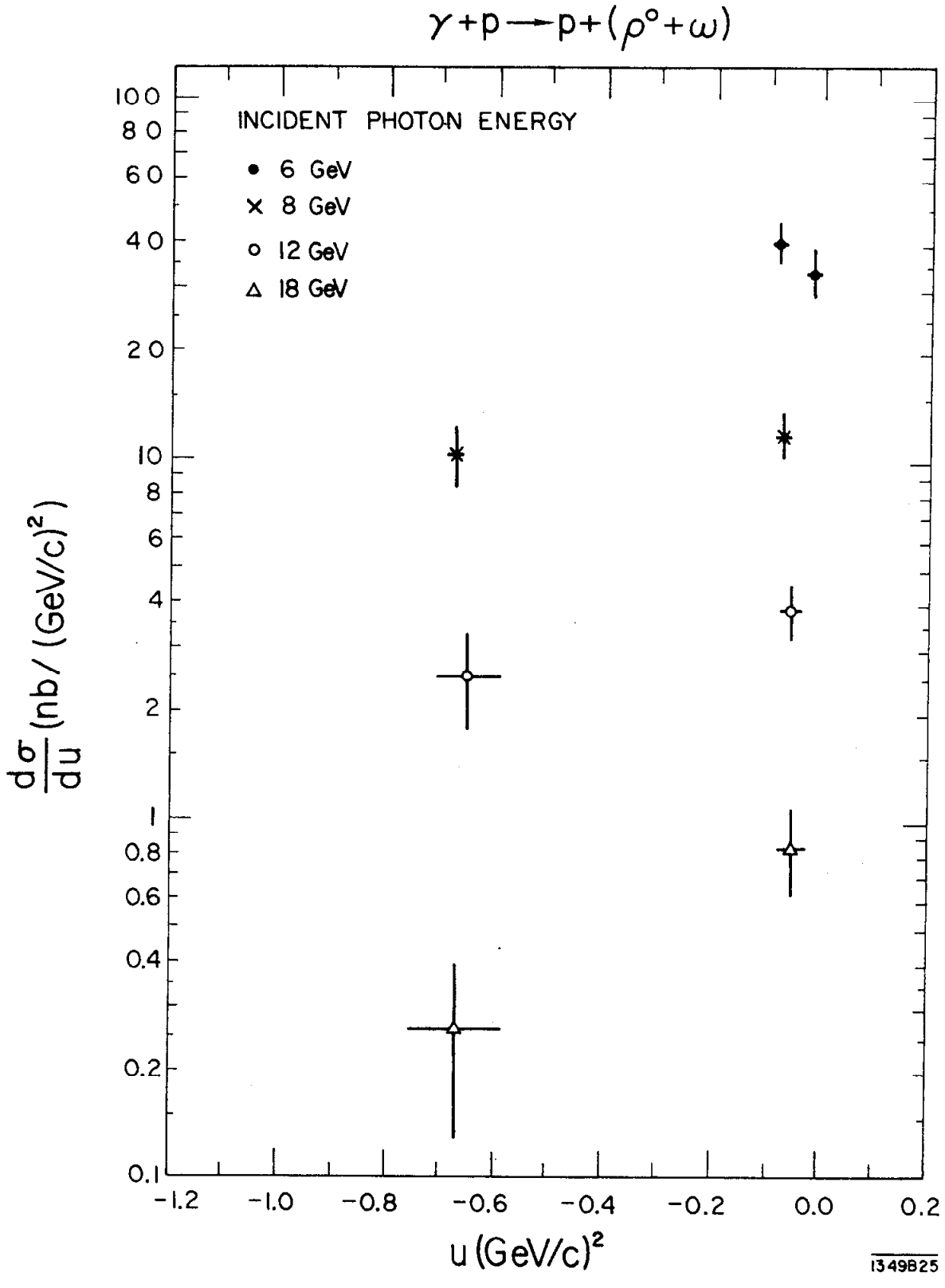

Fig. 5.11 --Differential cross section dσ/du vs u for the reaction $\gamma p \longrightarrow p(\rho^{o} + \omega)$.

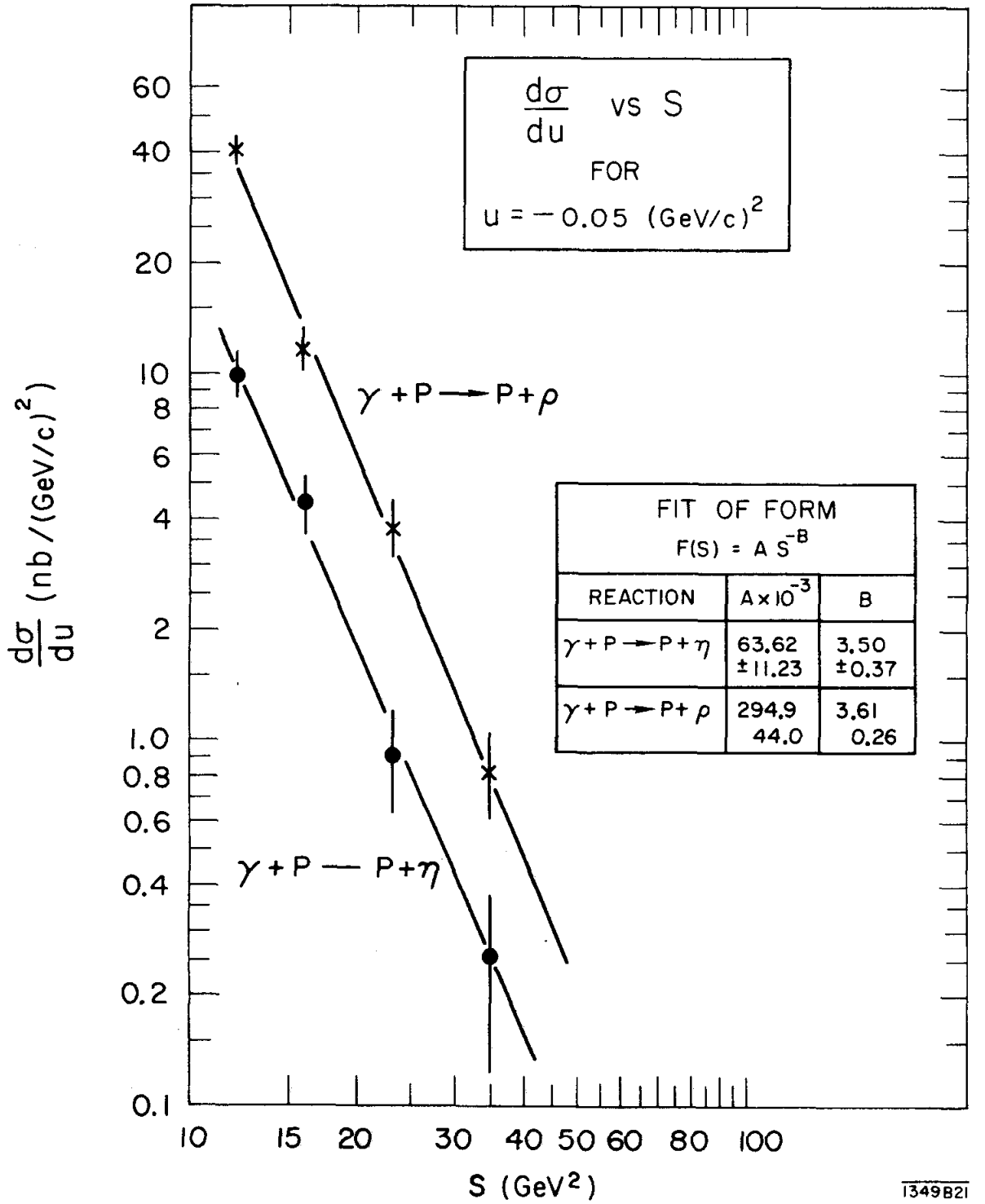

Fig. 5.12--Differential cross section $d\sigma/du$ vs s for the reactions $\gamma p \rightarrow p\begin{Bmatrix}\rho^0+\omega \\ \eta\end{Bmatrix}$ for fixed u. The solid curves represent fits to the data of the form $F(s) = A(s)^{-B}$ with the values for the parameters A and B as shown.

TABLE 5.1

DIFFERENTIAL CROSS SECTIONS FOR $\gamma + p \longrightarrow p + \pi^o$

Spectrometer Angle (degree)	u $(GeV/c)^2$	$-d\sigma/du$ $nb/(GeV/c)^2$	Spectrometer Angle (degree)	u $(GeV/c)^2$	$-d\sigma/du$ $nb/(GeV/c)^2$
6 GeV			12 GeV		
0.75	+ 0.06	12.10 ± 1.02	0.75	0.00	1.68 ± 0.22
1.60	+ 0.03	16.13 ± 1.23	1.20	- 0.04	2.11 ± 0.19
2.75	- 0.03	15.97 ± 1.21	1.70	- 0.10	1.85 ± 0.23
3.70	- 0.11	11.56 ± 1.00	2.24	- 0.20	0.96 ± 0.16
4.60	- 0.20	8.33 ± 0.89	2.83	- 0.34	0.65 ± 0.13
5.55	- 0.32	4.66 ± 0.52	3.35	- 0.49	0.56 ± 0.11
6.75	- 0.49	3.73 ± 0.61	3.85	- 0.65	0.57 ± 0.08
			4.32	- 0.82	0.46 ± 0.11
			4.78	- 1.01	0.36 ± 0.09
			5.25	- 1.21	0.22 ± 0.06
8 GeV			18 GeV		
0.75	+ 0.04	5.51 ± 0.43	0.75	- 0.04	0.638 ± 0.069
1.90	- 0.03	6.68 ± 0.54	1.15	- 0.11	0.630 ± 0.081
2.70	- 0.10	5.60 ± 0.50	1.48	- 0.20	0.415 ± 0.051
3.43	- 0.20	3.54 ± 0.36	1.82	- 0.32	0.202 ± 0.062
4.20	- 0.32	2.12 ± 0.28	2.25	- 0.49	0.146 ± 0.045
5.10	- 0.50	2.21 ± 0.28	2.59	- 0.66	0.148 ± 0.030
5.82	- 0.65	2.08 ± 0.27	2.90	- 0.83	0.129 ± 0.039
6.55	- 0.83	1.76 ± 0.28	3.21	- 1.02	0.087 ± 0.020
7.20	- 1.01	1.43 ± 0.31	3.52	- 1.23	0.073 ± 0.029

TABLE 5.2

Energy (GeV)	Spectrometer Angle (Degrees)	$\gamma + p \rightarrow p + \eta^0$		$\gamma + p \rightarrow p + (\rho^0 + \omega)$	
		U $(GeV/c)^2$	$-d\sigma/du$ $nb/(GeV/c)^2$	U $(GeV/c)^2$	$-d\sigma/du$ $nb/(GeV/c)^2$
6	1.60	+ 0.011	6.82 ± 1.56	- 0.010	33.2 ± 4.9
6	2.75	- 0.046	9.91 ± 1.39	- 0.075	40.2 ± 5.0
8	1.90	- 0.050	4.46 ± 0.86	- 0.063	11.7 ± 1.6
8	5.82	- 0.670	2.10 ± 0.57	- 0.670	10.3 ± 2.0
12	1.20	- 0.045	0.92 ± 0.30	- 0.055	3.83 ± 0.65
12	3.85	- 0.645	0.47 ± 0.42	- 0.645	2.53 ± 0.75
18	0.75	- 0.042	0.26 ± 0.12	- 0.051	0.83 ± 0.22
18	2.59	- 0.670	0.053 ± 0.058	- 0.670	0.26 ± 0.13

APPENDIX A

Missing Mass Technique

Assume for the moment that the energy of the photon initiating the reaction is known. The missing mass of the particle or particles associated with the final state proton can then be calculated according to the following expression and histogrammed.

$$MM^2 = (\tilde{K} + \tilde{M}_T - \tilde{P}_D)^2 \qquad (A.1)$$

$$= M_T^2 + M_D^2 - 2M_T E_D + 2K(M_T - E_D + P_D \cos\theta_{sc})$$

MM^2 = squared missing mass (GeV^2)

M_T = mass of target particle (proton)

"~" = indicates four-vector

M_D, E_D, P_D = mass, energy and momentum of detected particle

θ_{sc} = laboratory angle of detected particle

K = photon energy (GeV)

The missing mass histogram should reflect several features. First, a peak centered at a squared missing mass value equal to that of the π^o mass squared and of magnitude in proportion to the size of the cross section for that reaction. The width for the peak is determined by the overall resolution of the apparatus as the π^o has negligible inherent width itself. Furthermore, if it is possible to produce additional types of particles in the backward direction — in the case of this experiment, η and ρ^o — then peaks in the missing mass histogram may possibly be seen centered at values equal to the mass squared of those particles. However, the squared mass of the η and ρ^o are 0.30 and 0.58 GeV^2 respectively, while that for two pi mesons is 0.08 GeV^2. Consequently, the η and ρ^o peaks sit upon a nonresonant background contribution arising from reactions in which multiple pions are produced.

Therefore, whether or not these peaks are seen experimentally is determined by their magnitude relative to that for the background term around those squared mass values, and the available running time vs that which would be necessary to acquire sufficiently good statistical data to make the separation.

However, two complications arise in the above procedure owing to the photon beam not being monochromatic, as was temporarily assumed above, but instead having a bremsstrahlung energy distribution. First, it was not possible to know the precise energy K (in Eq. (A.1)) of the photon initiating the reaction. Thus, what K value to use when calculating MM^2? Second, it was not possible to count directly the number of photons in the incident beam. The need for determining both of these quantities is obvious from Eq. (III.1) which describes the rate of events into a specified bin of the missing mass histogram.

Calculation of MM^2

The first difficulty is surmounted as follows. For K in Eq. (A.1), insert the value K_0, the maximum photon energy, equal to the energy of the electrons producing the photon beam. The effect of this insertion is as follows, if for the moment it is assumed that all protons detected come from the state with the π^o moving backward in the cm system.

Protons associated with events initiated by photons of energy K_0 will have measured values of momenta and angles such that missing mass values calculated by Eq. (A.1) with $K = K_0$, will be distributed about the mass of the π^o; because of the imperfect resolution of the instrumentation the distribution will not be infinitely sharp. On the other hand, protons associated with events initiated by photons somewhat lower in energy than K_0, will have measured values of momenta and angles such that the missing mass values calculated from Eq. (A.1), again with $K = K_0$, will be appreciably higher than that of the π^o mass. If now the photon

number spectrum, dN/dK, times the differential cross section, $d\sigma/d\Omega$, is assumed to be independent of K, then the missing mass distribution so calculated for this one reaction will correspond to the flat "step" indicated in Fig. A.1a and labeled "a".

For example, if $K_0 = 6$ GeV, and the detected proton from the $p\pi^o$ final state, with the π^o at 180 degrees, has a momentum of 5.86 GeV/c, then the energy of the photon initiating the reaction was, in reality, 5.48 GeV. The squared missing mass, MM^2, calculated from Eq. (A.1) with $K = K_0 = 6$ would however, be 0.90 GeV^2 and not 0.018 GeV^2, the squared mass of the π^o. Such an event would therefore, be counted in the histogram bin which included the missing mass value of 0.90 GeV^2.

Actually, dN/dK and $d\sigma/d\Omega$ and their product, will not be exactly independent of K. But in practice, as explained further below, the step shape is needed only for a K range of a few percent, and over this range we can in fact neglect the variation in $(dN/dK) \cdot (d\sigma/d\Omega)$. In effect, we calculate $d\sigma/d\Omega$ for K values at the tip of the bremsstrahlung spectrum, from the magnitude of the height of the step at the rise point. The width of the rising edge of the step arises from (a) the overall resolution of the experimental setup and (b) the width of the leading edge of the bremsstrahlung spectrum.

If now it is possible to produce a second type of particle whose mass is greater than that for the π^o, then by arguments similar to those above, a corresponding step would be produced, indicated as step "b" in Fig. A.1a. If in addition, it is possible to produce 3, 4, 5, etc. body final states, which implies that the proton associated with such states would have a continuous momentum distribution, for example in multipion production, then correspondingly one would have from this effect the dashed curve in Fig. A.1a. We can see now why it

is not important whether the step for a given particle is exactly flat. The reason is that we must in any event deal with the problem of a nonflat "background" distribution, the shape of which is not precisely known a priori.

The missing mass distribution measured in the experiment should thus appear as the summation of a series of steps plus the nonresonant background term from the multipion final states. Figure A.1b is such an experimentally measure plot.

Determination of ΔN_γ

The second problem, determination of $\Delta N\gamma$, was handled as follows. Let $\phi(K, K_0)$ be a function that represents the shape of the bremsstrahlung spectrum according to the relation $\phi(K, K_0) = K(dN/dK)\, N_1$, where N_1 is a normalizing constant, and where dN is the number of photons in the band dK at energy K. K_0 is the tip energy. Figure A.2 shows the normalized shape of ϕ for two actual cases, normalized to $\int_0^{K_0} \phi(K, K_0)dK = K_0$. These curves were calculated by D. Yount.[1] Using a different and more convenient normalization, with $N_1 = 1$, $dN = \phi(K, K_0)\, dK/K$.* Note that $\phi(K, K_0) = K\, dN/dK$ is then equal to dE/dK, where dE is the beam energy in the band dK. The total energy contained in the beam is then given by $\int_0^{K_0} \phi(K, K_0)\, dK = E_{tot}$. Experimentally the total energy of the photon beam can be measured and in terms of it a quantity "number of equivalent quanta" is defined, by

$$NEQQ \equiv E_{tot}/K_0 \qquad (A.2)$$

If the bremsstrahlung spectrum had an exact "1/K" shape, the part of the total beam energy in an energy band of width ΔK would be given by $\Delta E = E_{tot}(\Delta K/K_0) = K_0\, NEQQ\, \Delta K/K_0 = NEQQ\, \Delta K$ and the number of photons within this energy band ΔK, would be given by $dN = NEQQ\, \Delta K/K$. However, the real spectrum is not

*A rough approximation to the shape of the bremsstrahlung spectrum is given by taking $\phi(K, K_0)$ equal to a constant. The spectrum dN/dK then has a "one over K" shape up to $K = K_0$.

simply "1/K" as mentioned, and thus it is necessary to insert into the preceding expression a multiplicative quantity, λ, which describes the shape of the spectrum at the value of K being considered.

Consequently we write,

$$\text{"number of photons in energy band" of width } \Delta K \text{ centered at energy K} = \Delta E/K = \Delta N(K) = \lambda \, NEQQ \, \Delta K/K \qquad (A.3)$$

This equation defines λ. An equivalent definition is given by

$$\lambda = \frac{\Delta E}{NEQQ\,\Delta K} = \frac{dE/dK}{\frac{1}{K_0}\left[\int_0^{K_0} dE/dK \, dK\right]} = \frac{dE/dK}{\left[dE/dK\right] \text{ average over K}} .$$

With the normalization used in Fig. A.2, $\lambda(K)$ is equal to the function plotted there. Thus for the 0.03 rl case, and for $K/K_0 = 0.85$ to 0.97, the value of λ is $\simeq 0.87$.

Now interpret ΔK as the width of the energy band from which photons could initiate reactions whose protons were detected by the spectrometer. Since the spectrometer accepts a momentum band, ΔP, the magnitude of ΔK can be determined from

$$\Delta K = \frac{\partial K}{\partial P} \Delta P \qquad (A.4)$$

where $\partial K/\partial P$ is the Jacobian of the transformation between "photon energy band" and associated "proton momentum band" as fixed by the spectrometer. The Jacobian is understood to be evaluated at the central momentum and angle values of the spectrometer acceptance. An explicit expression for it is given in Eq. (IV.4).

The value K_0 is inserted in Eq. (III.3) when one calculates $d\sigma/d\Omega$, as indicated in Eq. (IV.2). For the very tip of the spectrum this clearly makes no difference. It is really the height of the rise, in Fig. A.1, which gives the cross section. (In any event, in using Eq. (III.3) or Eq. (IV.2) to calculate $d\sigma/d\Omega$, we would not in general know what value of K to use except at the location of each rise.)

The value of λ to be used, in Eq. (IV.2), is thus the value appropriate to the flat part of the step following the rise. Following the discussion above, for the 0.03 rl radiator we use the value $\lambda = 87$.

Observe that the essentially flat region of the photon spectrum begins approximately 0.06 GeV below the tip energy, K_0.

REFERENCES FOR APPENDIX A

1. D. Yount (private communication).

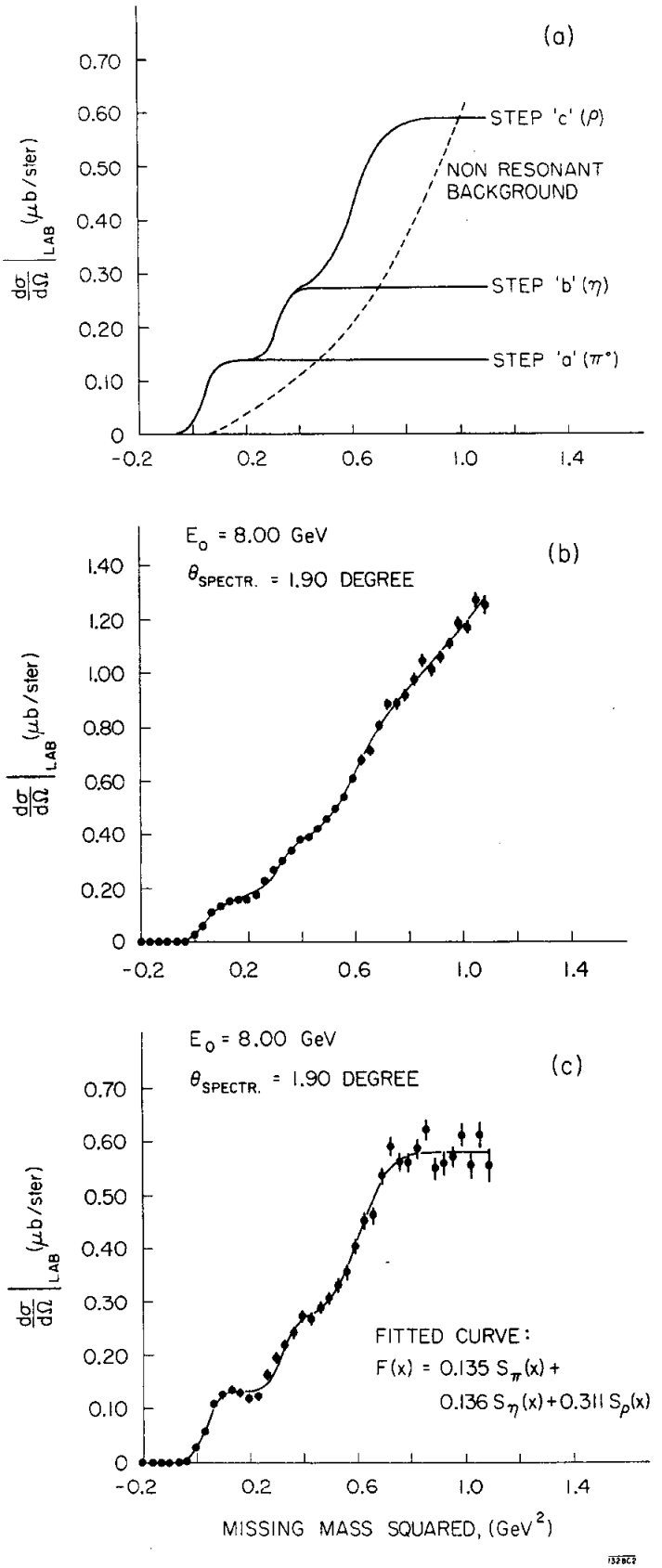

Fig. A.1--(a) Steps (solid curves) plus nonresonant multi-pion background (dashed curve) into which a proton missing mass spectrum can be decomposed. (b) Proton missing mass spectrum at 8 GeV, $\theta_{lab} = 1.9^{o}$. (c) The same data point plotted with the fitted background subtracted.

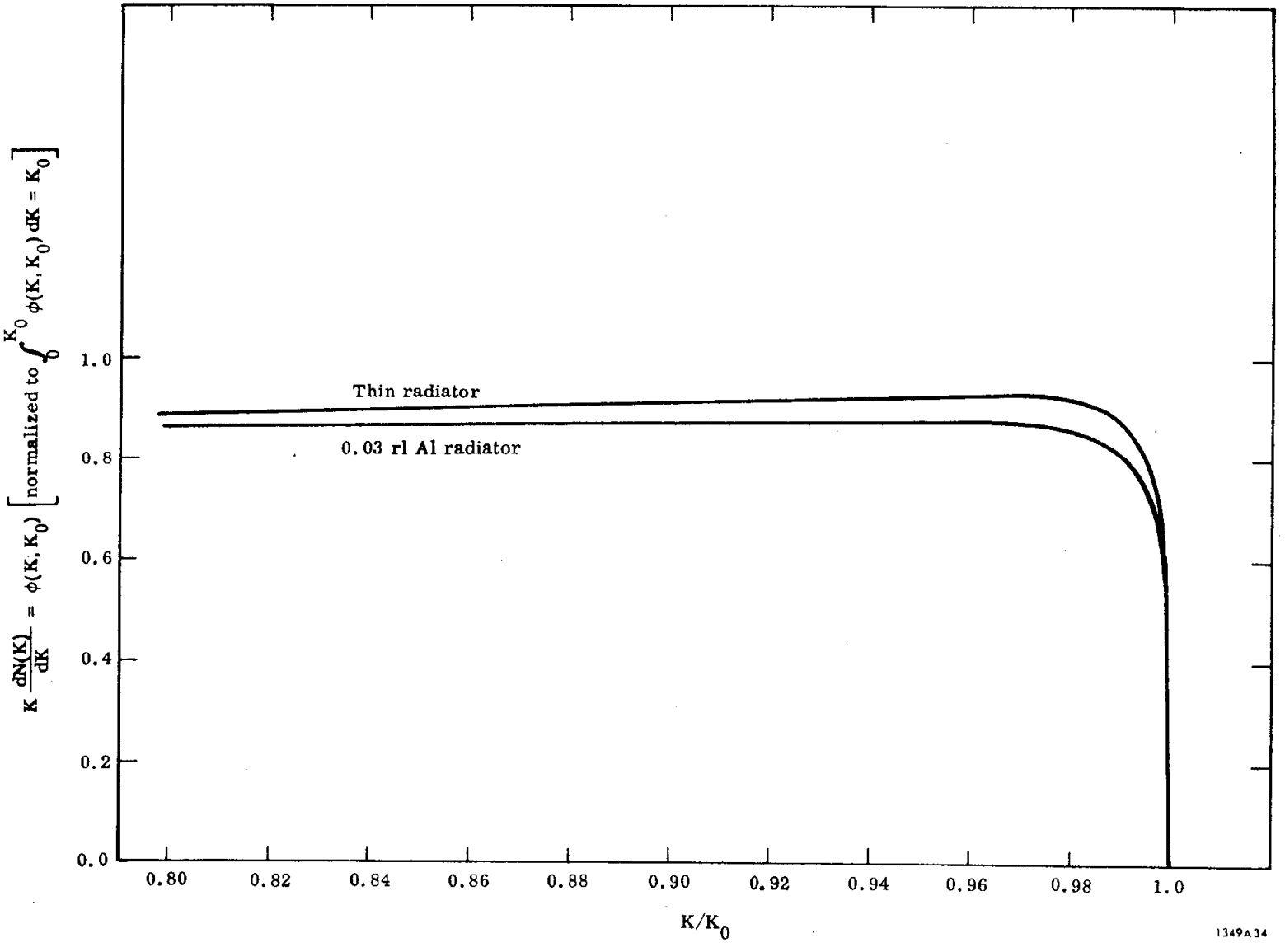

Fig. A.2--Normalized bremsstrahlung spectra produced by electrons of energy 6 GeV impinging upon (a) "thin" radiator and (b) 0.03 rl Al radiator.

APPENDIX B

Particle Detection System

The cement shielded "hut" at the downstream end of the 20 GeV/c spectrometer housed the detection system for those particles transported by the magnetic optics system of that instrument. Output signals from the various detectors, schematically depicted in Fig. 3.4, were transmitted to the electronics over some 350 feet of coaxial cable and eventually multiplexed into an on-line computer (see Ref. 5 of Chapter III). The detection system subdivided into three functional classes: class (1), trigger counters to alert the fast electronics, class (2), hodoscopes which supplied data that allowed the kinematics of the detected particle to be calculated, and class (3), particle type identification counters.

Class (1) — Trigger counters: A particle which interacted with the three scintillation type trigger counters Tr_1, Tr_2, Tr_3, was considered to be one of possible interest by the electronics, on-line computer, complex. A three-fold coincidence from these counters, initiated gating pulses for the remainder of the electronics in the detection system and alerted the computer.

Class (2) — Hodoscopes: Kinematics of the detected particle could be recovered from the information taken from the four hodoscopes. The technique was as follows.

Consider the space of the detection system in the "hut" where no magnetic elements of the optics system were present and thus particles traveled in straight-line trajectories. (Neglect scattering for the present as it was accounted for through a correction factor.) Measure, (a) the angle in the vertical plane, ψ_V, which a particle trajectory makes with the trajectory of the central ray of the optics system as it traverses the "hut," (b) the angle in the horizontal plane, ψ_H, made by the particle trajectory with the central ray, and (c) the vertical

displacement, y_d, and the horizontal displacement, x_d, of the trajectory with respect to the central ray at the focal plane of the optics.

Next, using the inverse matrix elements describing the spectrometer optics, transform these four quantities into four corresponding quantities at the target; i.e., the laboratory coordinate space; which quantities then turn out to be the projection of the true scattering angle in the vertical and horizontal planes, ϕ_0 and θ_0 respectively, the particle's momentum at the target, $\delta = \frac{\Delta P}{P} \times 100$, and the lateral displacement of the particle, x_0, in the horizontal plane, measure with respect to the central ray of the optics as it intersects the target proper. In making this transformation, it is assumed that the particles all leave the target with no vertical displacement above or below the central ray for the optical system. Experimentally it was not possible to meet this condition as it was necessary to use a beam spot with vertical extent on the order of 1 centimeter in order to provide a useable counting rate. The effect of the vertical beam spread was to reduce the ideally obtainable momentum resolution as discussed under "Resolution" in Chapter III.

The two quantities ψ_V and y_d, were determined by recording which "bins" the particle trajectory intercepted in the "Phi" and "Momentum" hodoscopes. Similarly, the two quantities ψ_H and x_d were determined by recording which "bins" the trajectory intercepted in the "X" and "Theta" hodoscopes. These hodoscopes were constructed of thin fingers of scintillator mounted on phototubes. The "X", "Phi" and "Momentum" hodoscopes were constructed with two overlapping rows of scintillation fingers while the "Theta" hodoscope consisted of three such overlapping rows. Overlapping scintillators to form "bins" reduced the granularity of space from that available with just the scintillation fingers themselves and furthermore increased the efficiency of the hodoscope system.

Class (3) — Particle-type identification counters: The detectors used to identify particles as to type were; a nitrogen gas filled threshold Cerenkov counter, a freon gass filled differential Cerenkov counter, a scintillator-lead plate sandwich shower counter, and a range telescope constructed of 9 scintillation paddles with lead plates in the gaps between paddles 1-2 and 2-3 and 10-inch thick steel blocks filling the gaps between the remaining scintillators.

A spherical mirror collected the light produced by particles traversing the differential Cerenkov counter. The focal plane for its optics was divided into three regions. Region 1, the central region, of angular extent from 0-40 mrads, was a black absorber. Region 2, the "inner" angular region extended from 40-60 mrads and was viewed by two phototubes whose combined output was fed to a pulse height analyzer (PHA). Region 3, the "outer" region, from 60 to 95 mrads, was viewed by four phototubes and their combined output fed to a second PHA. The channel number output from these two pulse-height analyzers was treated by the computer as the X-Y coordinates on a three-dimensional plot with number of events plotted along the Z axis. With this arrangement, it was possible to section the X-Y plane into three regions which, for normal operating conditions, placed signals from protons in Region 1, signals from pions and kaons in Region 2 and particles that produced little or no light in either angular region into Region 3. Pulses from the threshold Cerenkov and shower counters were also fed into separate pulse-height analyzers.

To insure knowing the position of the effective zero on each PHA scale, a small, constant magnitude pulse, was added to the signal pulse from the associated detector. This resulted in shifting the effective zero of the scale to channel 10 in the analyzer. Thus a particle traversing a detector but producing no effective signal in it, would still record in the effective zero channel of the corresponding analyzer, producing what was termed a "pedestal pulse."

With this arrangement, particle identification was accomplished by checking the "signature" that each event produced in the system. Characteristic "signatures"* were as follows:

Electrons: Nonpedestal pulses in both of the Cerenkov counters, a signal in the shower counter that fell within the range determined for electron signals in the corresponding pulse-height analyzer, no penetration into the range telescope.

Muons: Nonpedestal pulses in the two Cerenkov counters, and shower counter, complete traversal of the range telescope.

Protons: Pedestal pulse in the threshold Cerenkov counter, a pulse in one of the three regions of the differential Cerenkov counter, normally Region 1, a pulse in the shower counter falling within the range for hadrons in the corresponding pulse-height analyzer, and some penetration into the range telescope.

Pions: A nonpedestal pulse in the threshold Cerenkov counter, a pulse in the pion region of the differential Cerenkov counter, a pulse in the shower counter falling within the range for hadrons in the corresponding pulse-height analyzer, and some penetration into the range telescope.

Kaons: A pedestal pulse for a momentum of 6 and 8 GeV/c but a nonpedestal pulse at momenta of 12 and 18 GeV/c in the threshold Cerenkov counter, a pulse in Region 2 of the differential Cerenkov counter and shower-range pulses which fell within the region for hadrons.

---

*Signature given describes the manner in which the entire detection system responded to the particle. Nonunderlined portions thereof indicates those aspects used by the computer software to determine particle type.

It is of course true that all events did not cleanly separate into particular regions or ranges of various detectors. Distributions in pulse-height analyzers for one type of particle had tails which could spill over into the region designated as that for another particle type. For example, the tail of the hadron pulse distribution in the shower PHA had some overlap into the adjacent region for electron pulses and consequently correction factors were introduced into the analysis to account for such phenomena.

Figures 4.2a, b show two outputs of the shower counter — range telescope histogram; the first (a) with the spectrometer set at a large angle (1.5°) and therefore detects few electrons while for the second (b), the spectrometer is set at a small angle (5°) and detects many electrons. In Fig. B.1a, b, the counts in the first range telescope bin (the bin in which electrons are recorded) of Fig. 4.2a, b are plotted against channel number. Areas of the two histograms are not normalized to each other. From the shape of the tail for the hadrons spilling into the electron region (Fig. B.1a) a correction was deduced to account for those hadrons having large pulse heights, i.e., greater than the electron cut in the shower counter PHA.

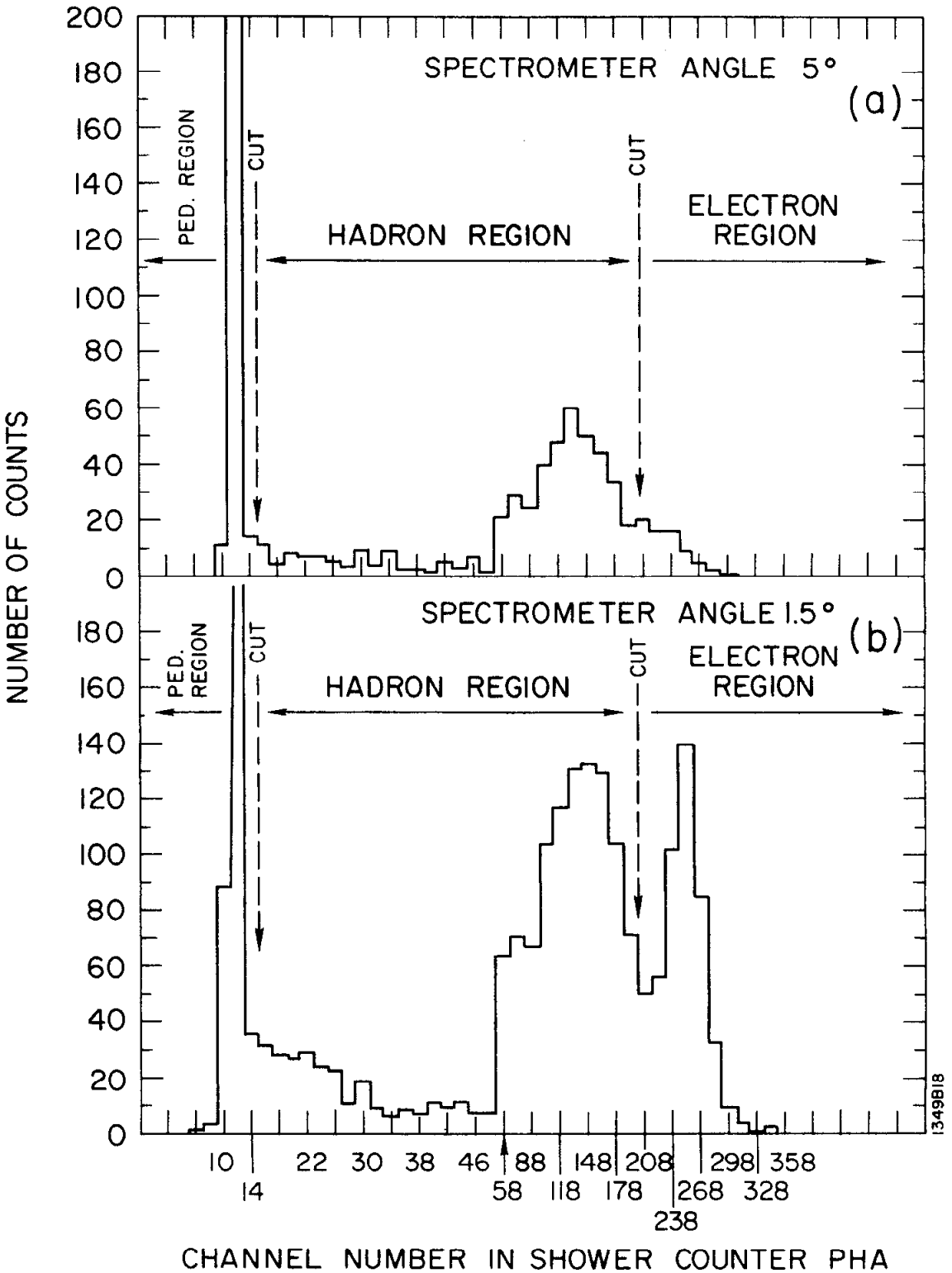

Fig. B.1--Counts vs channel number in shower counter pulse height analyzer (PHA). In (a), spectrometer was set at a large angle (5^{o}) and consequently measured few (~ 0) electrons as indicated by the combined information from shower counter and range telescope. In (b), spectrometer was set at a small angle (1.5^{o}) and measured an electron peak. Consequently the events recorded above channel 200 in (a) give a measure of the number of hadrons which produce sufficiently large pulse heights to be recorded in the electron region. Note: the apparent peak centered around channel 150 is caused by a change of horizontal scale which occurs at channel 50.